A SYSTEMATIC APPROACH TO QUANTIFYING THE NOISE-ENSO RELATIONSHIP AND ITS EFFECT ON EXTREME EL NIÑO EVENTS

A DISSERTATION SUBMITTED TO THE GRADUATE DIVISION OF
THE UNIVERSITY OF HAWAIʻI AT MĀNOA
IN PARTIAL FULFILLMENT OF THE REQUIREMENTS FOR THE
DEGREE OF

DOCTOR OF PHILOSOPHY

IN

METEOROLOGY

AUGUST 2014

By

AARON F. Z. LEVINE

Dissertation Committee:

Fei-Fei Jin, Chairperson
Jennifer Griswold
Jianping Li
Duane Stevens
Axel Timmermann

Acknowledgements

I would like to thank my advisor, Fei-Fei Jin, for his direction, my committee for their patience and guidance, and the members of my research group, particularly Christina Karamperidou and Malte Stuecker, for their helpful discussions. I acknowledge the World Climate Research Programme's Working Group on Coupled Modelling, which is responsible for CMIP, and I thank the climate modeling groups (listed in Table 5.1 of this paper) for producing and making available their model output. For CMIP the U.S. Department of Energy's Program for Climate Model Diagnosis and Intercomparison provides coordinating support and led development of software infrastructure in partnership with the Global Organization for Earth System Science Portals.

Abstract

State-dependent noise forcing, where properties such as amplitude are dependent on the background conditions, has been shown as a potential cause for the El Niño - La Niña amplitude asymmetry. Complex characterization of the state dependency of El Niño noise forcing as documented in most existing research has not been readily applicable to the outputs from the current generation of coupled climate models (GCMs). Here a simple method for determining the overall strength of the state-dependence factor of the El Niño noise forcing is proposed and tested. This method is shown to be independent of the data sampling from monthly mean to daily data, which make it readily applicable to monthly climate data archives. Using a reanalysis product and two coupled GCMs, the method is then applied to the equatorial zonal windstress, which is a known noise source for the El Niño-Southern Oscillation (ENSO) phenomenon. The windstress in all three cases is shown to have strong state-dependent noise forcing.

The state-dependent component of the noise forcing is further isolated and shown to be enhanced by the Pacific Warm Pool and Westerly Wind Burst interaction. The coupled process acts to increase the low-frequency component of state-dependent windstress noise forcing, a part of noise forcing that is most essential in the excitation and strengthening of ENSO.

The methodology is then further applied to the outputs from a suite of Coupled Model Intercomparison Project (CMIP)5 model simulations under various scenarios. It is found that most of the CMIP5 models underestimate the state-dependence factor of the equatorial windstress on sea-surface temperature (SST). There is a consistent relationship with the zonal equatorial SST gradient and the state-dependence factor. However, the models fail to agree on changes of the state-dependence factor due to global warming.

Finally, using the conceptual model, the state dependence factor is shown to control the ENSO skewness and is a predictor of the frequency of occurrence of extreme El Niño events. To a large extent, the CMIP5 simulations are in support of these theoretical relationships.

Contents

List of Figures

Chapter 1

Introduction

1.1 The Significance of El Niño

Over the past few decades, El Niño-Southern Oscillation (ENSO) has been a major area of climate research. Even though it is a tropical coupled ocean-atmosphere phenomenon in the Pacific Ocean basin, ENSO has global implications. Through global teleconnections, it has been linked to changes in precipitation and temperature throughout North America, to the Indian and Austral summer monsoons and to changes in tropical cyclone distribution among many other effects. These global effects vary from event to event with central Pacific El Niño projecting on to different teleconnection patterns than eastern Pacific El Niño (Kug et al., 2009). However, in both cases, the stronger the ENSO event, the more marked these anomalies have a tendency to become. The so-called El Niño of the Century in 1997-98 resulted in an estimated 34 billion USD (unadjusted) in damages globally, despite the early forecast of an event nine months prior to the peak (Nicholls, 2001).

Despite substantial study and significant potential societal impacts, the changes to ENSO from anthropogenic climate change are not well constrained (IPCC AR5). A recent study, (Power et al., 2013), has found that if the last century's ENSO record is superimposed on next century's projected SST change, the major impacts of ENSO will be increased. However, the authors noted that the potential changes to ENSO

characteristics could alter this. Cai et al. (2014) found an increase in the number of extreme El Niño events, as classified by eastern Pacific precipitation, in response to global warming. These potential changes can include changes in amplitude, frequency, and location of maximum SST anomaly. As shown by Stevenson et al. (2012) and Wittenberg (2009), the length of our current climate record is not sufficient to determine with statistical significance the scope of these changes. However, based on tropical Pacific coral records, adjusting for data sparsity, and comparing with the ENSO variability of a highly variable coupled model, Cobb et al. (2013) claim that ENSO over the last century is significantly larger than ENSO at any point over the last millenia. This is in agreement with the findings of McGregor et al. (2010) for the period of the last 350 years.

There has also been much discussion over the last decade on ENSO flavors. These flavors of El Niño delineate different types of El Niño based on the location of the maximum warming. This maximum warming can occur in the eastern Pacific (also known as a canonical El Niño) or in the central Pacific (also known as El Niño Modoki or warm pool El Niño) (Ashok et al., 2007; Kug et al., 2009; Ren and Jin, 2011). Yeh et al. (2009) found that in response to global warming, there would be an increase in the fraction of El Niño events that could be classified as central Pacific El Niños. However, other research has disputed the simple classification of two distinct modes of El Niño variability, showing that the location of maximum SST anomaly during an El Niño event exists as a continuum (Ray and Giese, 2012). At the core of these different results lies the question, how well do we understand the natural variability of ENSO.

1.2 ENSO Linear Theory

In improving our understanding of ENSO's natural variability, a major tool is simple ENSO models. Simple linear coupled models of ENSO have been designed and used to study ENSO growth, frequency, spatial pattern, and mean-state sensitivity. This approach has proven fruitful in developing a basic understanding of these properties. What follows here is a brief discussion of the linear dynamics of ENSO as viewed through different conceptual models of ENSO.

El Niño initially grows, peaks and then quickly becomes an opposite sign anomaly, La Niña (Rasmussen and Carpenter, 1982; Kessler, 2002). The initial growth is related to a positive feedback and the flip to the opposite signed anomaly comes from a delayed negative feedback. An early conceptual model to capture this is the delayed action oscillator (Suarez and Schopf, 1988; Battisiti and Hirst, 1989). The delayed action oscillator model focuses on ocean wave dynamics in relation to ENSO. An initial downwelling Kelvin wave, kicked off by a westerly wind burst, travels east along the equator, lowering the thermocline and shutting off the mixing from the shallow thermocline in the eastern Pacific. This generates a positive SST anomaly in the east which will further induce a westerly wind anomaly. This positive feedback is known as the Bjerknes feedback. Meanwhile, the westerly wind anomaly also generates upwelling Rossby waves that travel westward off the equator. Upon reaching the western boundary, the Rossby waves reflect and become an eastward propagating Kelvin wave. Like the Rossby waves, this Kelvin wave is upwelling, raising the thermocline in the eastern Pacific and enhancing cold water upwelling, which opposes the warm SST anomaly generated earlier. This delayed negative feedback is responsible for terminating the El Niño event and intiating the La Niña event. Observations with the TAO (Tropical Atmosphere Ocean) array in the equatorial Pacific have been able to observe these equatorial Kelvin waves (McPhaden et al., 1988).

Another conceptual model for ENSO is the recharge oscillator model (Jin, 1997a). The recharge oscillator also contains an initial positive feedback, followed by a delayed negative feedback. In the recharge oscillator, a positive SST anomaly induces a westerly wind anomaly which reinforces the positive SST anomaly by flattening the equatorial thermocline. This process is a positive feedback for ENSO growth. While the winds deepen the thermocline in the eastern Pacific, their curl also causes a slow discharge of oceanic heat content from the equatorial regions poleward. This discharge of heat content is the delayed negative feedback that ends the El Niño event and begins the subsequent La Niña. The total warm water volume in the equatorial Pacific has been observationally shown to lead the ENSO signal by 6-9 months (Meinen and McPhaden, 2000), confirming the recharge mechanism. It can also be shown that the delayed and

recharge oscillator conceptual models are not mutually exclusive, but rather two different descriptions for the same processes involved in ENSO (Sarachick and Cane, 2010).

A model of intermediate complexity, the Zebiak-Cane model, which uses a 1.5 layer ocean model with explicit SST mixed layer calculations was the first dynamical model to predict ENSO and has been used to examine many aspects of ENSO. One feature of this model which has proven particularly useful in elucidating key aspects of ENSO is that it specifies the mean state and annual cycle. By altering the mean climate state and adjusting different model parameters, the sensitivity of ENSO to different parameters has been explored (Jin and Neelin, 1993b,a; Neelin and Jin, 1993; Fedorov and Philander, 2000, 2001; Bejarano and Jin, 2008).

Using a simplified version of the Zebiek-Cane model, the relative importance of thermocline processes and zonal SST-advection to El Niño growth has been examined in many studies. In a series of papers, Jin and Neelin (1993b), Jin and Neelin (1993a), and Neelin and Jin (1993) examined the effect of the strength of the SST-atmosphere coupling and wave propagation speed and found that there were two dominate modes of El Niño growth which they dubbed the SST-mode and the thermocline mode. Additionally, they found that over a wide range of realistic parameters, both of these modes coexisted with the SST-mode having a higher frequency. Fedorov and Philander (2000, 2001) found that changes in the mean state of the tropical Pacific could account for the observed shifts in ENSO frequency and amplitude across the 1970s Pacific climate shift. Similar mapping can be done for the changes in El Niño in the early 2000s. Bejarano and Jin (2008) further examined changes to ENSO growth rate and frequency. They found that both of these modes coexist over a wide domain of parameters characterizing changes in the background state. Exploration of the different ENSO flavors has shown that the central Pacific El Niño events are dominated by zonal SST-advection processes compared to the eastern Pacific El Niño events, which are dominated by thermocline processes (Ren and Jin, 2013).

The differences between the relative contributions of the advective and thermocline feedbacks are examined by analyzing the anomalous heat budget (Jin and An, 1999a; Jin et al., 2006; Kim and Jin, 2011a). The change in growth rate determined by the Bjerknes

Instability Index has been shown to be related to the change in ENSO amplitude in different coupled models (Kim and Jin, 2011b). The different models disagree on which feedback is the dominant positive feedback, between the zonal advective, thermocline and Ekman and the final growth rate ends up being the difference of the two or three dominant feedbacks (Kim and Jin, 2011b).

1.3 ENSO Non-Linearity

An oscillator will continue to alternate regularly between positive and negative, increasing in magnitude if the growth rate is positive or reducing before eventually coming to rest at equilibrium if the growth rate is negative. Most of the intial versions of the conceptual models consider a positive growth rate to create an El Niño event. To prevent runaway growth, an ad-hoc and symbolic non-linear damping term has frequently been invoked to represent some of the systemic non-linearities in the more complex real world.

1.3.1 Amplitude Asymmetry

The linear models of ENSO have allowed for in depth study of many of the physical processes involved in the periodic behavior of ENSO. However, ENSO displays many properties that are not fully captured by linear processes. For example, there is a warm/cold asymmetry in ENSO. Figure 1.1 shows a timeseries of ENSO from the last 65 years. ENSO's amplitude asymmetry is immediately apparent. The postive (El Niño) SST anomalies are on the whole larger than the negative (La Niña) amomalies. The positive and negative feedbacks that contribute to the growth of the positive and negative phases of ENSO have been explored (Jin et al., 2006; Bejarano and Jin, 2008). There are five major sources for amplitude asymmetry, non-linear dynamic heating, the atmospheric non-linearity involved in convection, biological feedbacks on ENSO, tropical instability waves, and the Madden-Julien Oscillation (MJO) or Westerly Wind Burst (WWB) feedback. Beyond the tropical Pacific, Indian Ocean dynamics have also been explored as a possible source of the amplitude asymmetry (Okumura and Deser, 2010; Okumura et al., 2011).

The results of Jin and An (1999b) and Jin et al. (2003) first suggested a role for non-linear dynamic heating in creating the amplitude asymmetry. The non-linear dynamic heating is predominantly attributable to the anomalous zonal advection of the anomalous temperature gradient. It is a positive feedback on the positive events while being a negative feedback on the negative events. Another cause of ENSO asymmetry is the asymmetric response of convection to ENSO temperature anomalies. Convection forms over SSTs in excess of $27°C$. Due to the zonal asymmetries of SST in the equatorial Pacific, the region of SSTs in excess of $27°C$ expands greatly during an El Niño event, while it is mostly unchanged during a La Niña event (Hoerling et al., 1997; Kang and Kug, 2002).

Unlike the first two feedbacks discussed, the next two feedbacks act as negative feedbacks and are more efficient for La Niña than for El Niño. In the equatorial eastern Pacific, climatological upwelling creates a shallow nutricline leading to significant primary biological productivity from solar radiation, which acts to absorb incoming solar radiation. During an El Niño event, reduced upwelling deepens the nutricline and lessens the biologic productivity. During a La Niña event, there is a significant increase in primary productivity and a resultant increase in solar absorption (Timmermann and Jin, 2002; Marzeion et al., 2005). Tropical instability waves are monthly scale waves that provide meridional heat mixing. They can therefore act as a negative feedback on ENSO. During La Niña events, tropical instability waves are much more active than during El Nño events. This leads to ENSO asymmetry by greater damping of La Niña anomalies than of El Niño ones (Vialard et al., 2001; An and Jin, 2004; An, 2008). The interaction of ENSO with the MJO or WWBs can also create an amplitude asymmetry. This is also referred to as multiplicative or state-dependent noise forcing of ENSO. This will be detailed in a later section of this dissertation.

Another readily apparent feature of the ENSO timeseries in Figure 1.1 is that El Niño events tend to be short, beginning and ending in under a year, while La Niña events can be multiple years long. ENSO has been observed to follow a regular progression from the beginning of an El Niño event through to a La Niña event. However, the tropical Pacific can linger in a La Niña state for multiple years in a row or remain in

an ENSO neutral state for many years after a La Niña event before the following El Niño event occurs (Kessler, 2002). The role of a simple deterministic non-linearity in the windstress response to SST has been found and offered as an explanation, particularly as it relates to the extended La Niña conditions (Choi et al., 2013). This has also been found using other forms of deterministic non-linearities within the ENSO feedbacks (DiNezio, personal communication).

1.3.2 ENSO Combination Tones and Phase Locking

Another aspect of non-linearity is ENSO phase locking, namely, that El Niño peaks in the boreal winter. The annual cycle interaction has been examined in the conceptual models as well. Simple models involving low-order chaos have been used to explain the syncronizing of ENSO to the annual cycle (Tziperman et al., 1995; Jin et al., 1994). This has also been shown to be the result of an annually varying linear growth rate (Stein et al., 2010) and the effect of phase locking between the annual cycle and ENSO (Stein et al., 2011). The annual cycle influences ENSO in other ways as well. The non-linear interactions between the two different frequencies of the annual cycle and ENSO create the combination tones, or spectral peaks tat exist at the sum or difference of the two interacting frequencies (Stuecker et al., 2013). The combination tones have been shown to play a vital role in the transition from El Niño to La Niña (McGregor et al., 2012). This asymmetry is important for ENSO impacts and not well captured by simple linear dynamics, but when accounted for as a deterministic non-linearity within the previously linear system, can be replicated with conceptual models.

1.3.3 ENSO Propagation Non-Linearities

It is also apparent that the SST anomalies sometimes appear to propagate eastward across the Pacific and sometimes westward, although this seems to be a change in appearance due to change in the annual cycle rather than an actual change in ENSO (Boucharel et al., 2013). The propagation asymmetry between El Niño and La Niña can also be explained by examaining the role of the total current as opposed to just

the anomalies. The total current reverses during extreme El Niño events causing the temperature anomalies to appear to propagate in the opposite direction of the moderate El Niños and La Niña events (Santoso et al., 2013; Wang and McPhaden, 2000). This too is not captured by linear ENSO theory predictions.

1.3.4 Stochastic Forcing of ENSO

ENSO as a slow oscillator interacts with many large scale, but much shorter period phenomena, such as the MJO, WWBs, tropical instability waves, etc. This interaction is fundementally non-linear but can be approximately treated by the approach first proposed by Frankignoul and Hasselmann (1977) for the interaction of weather with climate in other oceanic regions. Specifically, one can treat this kind of slow-fast interaction with a stochastic model. It has been observed that WWBs can produce a Kelvin wave that travels along the equatorial Pacific modifying the depth of the thermocline (McPhaden et al., 1988), which can trigger an El Niño event. WWBs tend to occur over timescales of 2-40 days (Yu et al., 2003; Eisenman et al., 2005; Tziperman and Yu, 2007). In comparison, ENSO has a timescale of 2-7 years. Thus, the WWBs can be considered noise in a mathematical sense because the time scale of these WWBs are much shorter than the timescale of ENSO. The mathematical noise can be white noise (constant energy at low frequencies) or red noise (more energy at lower frequencies than at higher ones). However, blue noise (more energy at higher frequencies than lower ones) has been shown to be deficient at forcing ENSO (Roulston and Neelin, 2000; Levine and Jin, 2010). The noise can also be additive (where the random forcing is completely independent of the state of the system) or multiplicative (where the random forcing has a dependence on the state of the system). This can be used to explain the irregularity of ENSO given the deterministic physics of the oscillator (Penland, 1996; Penland and Sardeshmukh, 1995; Kleeman and Moore, 1997; Moore and Kleeman, 1999; Zavala-Garay et al., 2003, 2004, 2005, 2008).

Keen (1982) created a climatology of these WWBs and found that there is a diversity of structures associated with them. For ENSO, the important pattern is the strong

westerly wind anomaly in the equatorial wave guide in western and central Pacific that projects onto the stochastic optimal (Moore and Kleeman, 1999, 2001; Zavala-Garay et al., 2005). These types of WWBs were shown to occur before the 1997-8 El Niño (Yu et al., 2003). Harrison and Chiodi (2009) created an updated climatology of WWBs and found that there were spatial differences in the typical WWBs between the last decade and the decade and a half prior. They speculated that this was important for differences in ENSO between the two periods. The WWBs that they found showed an easterly component which converged with the westerlies of the WWBs in the central Pacific in the post-1998 period. This easterly component was not present in their analysis in the pre-1998 period. They also reported changes in the amount of WWBs in the central and eastern Pacific over that time. These changes in WWBs could result in changes to ENSO between these periods.

Coupled model experiments have shown that the frequency of occurrence of large and moderate El Niño events significantly increases after a WWB has been inserted into the model compared with the control runs without the inserted WWB (Lengaigne et al., 2004; Lopez and Kirtman, 2013). Lengaigne et al. (2004) found that there are additional WWBs that occurred after the inserted WWB in the ensemble simulations that formed El Niño events which did not occur in the cases that did not form El Niño events. This suggests that multiple WWBs are needed to trigger an El Niño event. The prevalence of them in the simulations that formed large El Niños make the role of many WWBs particularly important for the largest El Niño events (Vecchi et al., 2006; Gebbie et al., 2007).

Examination of the 1997-8 El Niño showed that multiple WWBs occurred one after another in its growth phase (McPhaden, 1999). These pulses are discrete, increasing in magnitude, and propagating eastward as the El Niño develops. Satellite wind observations have shown the importance of these WWBs and their eastward propagation in initiating El Niño events (Tziperman and Yu, 2007) as well as simplified model experiments showing how this type of forcing can lead to more and larger El Niño events (Eisenman et al., 2005; Lengaigne et al., 2004; Gebbie et al., 2007). However, theoretical studies show that high frequency noise forcing cannot create an El Niño event

(Roulston and Neelin, 2000; Levine and Jin, 2010). These studies suggest that it is the low frequency component of the noise forcing that is responsible for forcing an El Niño event. To more thoroughly examine the creation and enhancement of the low frequency component from the high frequency variability, we need a better understanding of the noise forcing of ENSO.

Normally, noise forcing is considered to be additive (Zavala-Garay et al., 2008; Penland, 1996). Additive noise is generally independent of the background ENSO state, meaning the properties of the noise, when taken as a whole over long time periods, do not change depending on whether or not an El Niño event is occuring. However, linear additive stochastic noise alone does not create changes in ENSO asymmetry or other higher-order moments unless there is another source of non-linearity within the system, instead multiplicative noise is required (Müller, 1987; Sardeshmukh and Sura, 2009; Levine and Jin, 2010). Multiplicative noise differs from additive noise in that there is a state-dependent component to the total noise. In this case, the state of ENSO changes the total noise properties. One of the advantages of using multiplicative noise is that it can effect the higher moments of the system like skewness (3rd moment) or kurtosis (4th moment) whereas additive noise cannot in the presence of linear deterministic feedbacks. As opposed to considering non-linear feedbacks that have also been shown to increase the higher-order moments of systems and have been explored as source of the non-linearities of ENSO, this dissertation will consider multiplicative noise.

Gebbie and Tziperman (2009b,a) have shown that increases in the number of WWBs and their eastward propagation can be associated with the larger El Niño amplitudes. They have also shown that this eastward propagation of the WWBs is associated with the eastward migration of the warm pool edge. Therefore, it has been suggested that these westerly wind bursts are not just a forcing mechanism for ENSO but are also affected by the underlying state of ENSO, and potentially a multiplicative noise process (Kessler and Kleeman, 2000; Vecchi and Harrison, 2000; Yu et al., 2003; Eisenman et al., 2005; Perez et al., 2005; Gebbie et al., 2007; Tziperman and Yu, 2007; Gebbie and Tziperman, 2009b; Kapur and Zhang, 2012). Many of these studies have focused on the interaction and coexistence of WWBs and changing SSTs in the central Pacific and how they relate

to large El Niño events.

Conceptual ENSO models incorporating multiplicative noise forcing have shown increases in ENSO asymmetry and the number of extreme El Niños, and decreases in ENSO predicatability (Jin et al., 2007; Levine and Jin, 2010). Unlike multiplicative noise forcing, semi-stochastic noise forcing has a stochastic (random) component and a deterministic component that is triggered during the initiation of El Niño event. In more complicated models, experiments have shown that adding semi-stochastic forcing to the models adds skewness to ENSO and increases the amplitude and irregularity of ENSO (Gebbie et al., 2007). In this experiment, the deterministic component of the forcing is the state-dependent part of the forcing and acted similarly to multiplicative noise forcing. The deterministic component that was added to the model in this scenario was also simplified to be Gaussian in space and time. This approach of defining the multiplicative component as Gaussian in space and time (although not necessarily determinisitic) has been previously repeated for many additional experiments. With semi-stochastic forcing, the WWBs are no longer randomly distributed but group after an initial WWB. It is more common to have a second and third WWB in this scenario than under additive noise forcing. This is attributed to the multiplicative noise forcing and is consistent with what was observed in 1997-8 El Niño event.

Using the semi-stochastic framework for windstress noise forcing of ENSO, coupled model experiments have shown that additional westerly wind stress events that occur, occur further to east. Eastward progression of the wind bursts much like that observed during the growth phase of the 1997-8 El Niño event are generally evident (Gebbie et al., 2007; Gebbie and Tziperman, 2009b,a; Lopez et al., 2013; Lopez and Kirtman, 2013). Gebbie and Tziperman (2009b) showed that including this semi-stochastic forcing into a predictive model improved the model's ability to predict El Niño. Further, their simuations suggest that it is the general characteristics of the deterministic component of the forcing and not the characteristics of the individual WWBs that are important in modifying ENSO. Similarly, Lopez et al. (2013) found that it is the low-frequency component of the state-dependent noise that played an important role in modifying ENSO characteristics as opposed to the high-frequency stochastic forcing. This is in

agreement with previous studies in conceptual and simplified physics models which have shown that the high-frequency component of the stochastic forcing alone is not an efficien ENSO driver (Roulston and Neelin, 2000; Levine and Jin, 2010).

A previous study, (Kug et al., 2008) attempted to measure the strength of the state dependence of the multiplicative noise. They found that the important region for the windstress forcing of ENSO was between 160øE-160 øW. However, their approach has not proved practical for additional applications and further study of the multiplicative noise forcing of ENSO. An issue with the practical implementation of this methodology is that it relies on daily data, which is not available in the same quantity as monthly mean data in the current archives from climate model experiments (CMIP3 and CMIP5) as well as requiring significantly more hard disk space. Another problem with this methodology is that spectral filtering is used to determine the noise forcing. The filtering limits the the noise spectrum to the energy between 20-90 days, which as has been previously discussed not efficient in forcing ENSO (Roulston and Neelin, 2000; Levine and Jin, 2010; Lopez et al., 2013).

Further, Kug et al. (2008) make use of simple linear regression to estimate the value of the state-dependence factor. Recent work on noise forcing of ENSO has shown that there is an increased response of windstress to the SST anomalies when the SST anomalies are positive (Choi et al., 2013). The additional response of the westerly windstress to the positive SST anomaly suggests a role for convection being involved in the response of the windstress to SST anomalies. Convection is suggested as a physical process due to its non-linear interaction with SST over the tropical oceans. Convection has a minimum threshold of SST below which it does not not form. By using a simple linear regression, Kug et al. (2008) did not account for the possibility of a convective threshold in their work on multiplicative noise. The importance of the convective threshold will be examined in greater detail throughout this dissertation.

1.3.5 Extreme El Niño Events

The previously outlined work on multiplicative noise forcing suggested that multiplicative noise forcing plays a role in creating extreme El Niño events. Extreme El Niño events are important due to their strong societal impact. During these extreme events, many of the climate anomalies associated with El Niño are significantly enhanced leading to severe droughts in some regions and severe flooding in other regions. Events of this magnitude tend to remain in the public consciousness long after they have occurred and better understanding the forcings associated with them is important to understanding and predicting extreme El Niño events, allowing for improved mitigation of the climate anomalies and increased community resiliency to extreme El Niño events.

Including multiplicative noise into CGCMs has been shown to effect eastern Pacific El Niño preferentially over central Pacific El Niño events (Lopez et al., 2013; Lopez and Kirtman, 2013). Eastern Pacfic El Niño events tend to be longer and stronger than their central Pacific counterparts. Lopez and Kirtman (2013) showed that this is related to the response of the thermocline to WWBs and was magnified by adding a state-dependence. Multiplicative noise has already been shown to increase the skewness of ENSO in conceptual and more complicated models (Levine and Jin, 2010; Gebbie et al., 2007). This increase in skewness can be seen as an increase in extreme El Niño events (Levine and Jin, 2010).

During an extreme El Niño event, SSTs in the entire equatorial Pacific are above the convective threshold. This causes a significant increase in precipitation in the cold tongue region. This enhancement is greater than just linearly accounting for El Niño amplitude (Cai et al., 2014). The non-linear enhancement of the precipitation in response to SST could have profound impacts when superimposed on anticipated global warming spatial patterns, which makes understanding the causes behind these extreme El Niño events of even greater societal significance (Power et al., 2013).

Observationally, during the 1997-8 El Niño event, there were multiple WWBs that triggered the event (McPhaden, 1999; Yu and McPhaden, 1999; McPhaden and Yu, 1999). Gebbie et al. (2007) suggested that the individual timing of the wind bursts

were unimportant in the creation of the El Niño events, but that the overall increase in WWBs was important. Similarly, Vecchi et al. (2006) found that while an unlikely large number of WWBs happened in the growth phase of the El Niño, the additional WWBs always occurred and they were involved in the creation of the extreme magnitude of the El Niño event. Taken with the findings that it is the low-frequency component of the noise forcing and not its high-frequency variability that is important for the forcing of ENSO (Roulston and Neelin, 2000; Levine and Jin, 2010), it is hypothesized that the low-frequency component of the noise is the main driver of these extreme El Niño events.

1.4 Coupled Model Simulations of ENSO

In general, most climate models simulate ENSO to a degree. However, across most of the GCMs that have participated in the Coupled Model Intercomparison Project (CMIP)3 and CMIP5, there are still aspects of ENSO that are poorly simulated in the current generation of climate models (Bellenger et al., 2014). Many models still poorly simulate ENSO amplitude (Bellenger et al., 2014). Those that do simulate ENSO amplitude correctly are frequently getting the amplitude right for the wrong reasons, with large cancelling errors in the different feedback terms (Kim and Jin, 2011b). Because ENSO growth can be described as the difference between two or three competing feedback terms, there is a large amount of uncertainty associated within the models on the relative importance of different processes (Kim and Jin, 2011b; DiNezio et al., 2012). Therefore, while unfortunate, it is somewhat expected that the models do not agree in the changes in ENSO amplitude or even the sign of the changes in ENSO amplitude due to anthropogenic climate change (Collins et al., 2010). Another aspect of the simulation of ENSO that the climate models struggle to correctly simulate is the ENSO spectrum. Although as shown by Wittenberg (2009) and Stevenson et al. (2012), observations do not exist for the requisite length of time to fully constrain the ENSO spectrum, observations show a broad spectral band of enhanced activity between 2 and 7 years. In contrast with the available data from observations, most models have long enough control simulations to fully constrain their ENSO peaks. In these control simulations, many models fail to

fully simulate the breadth of the ENSO peak simulated within observations, instead have strong discernable peaks at one or two different frequencies (Bellenger et al., 2014).

Climate models still struggle with the seasonal phase locking of ENSO to boreal winter (Stein et al., 2014). As has been previously discussed in observations, El Niño events peak during the boreal winter months. However, while many of the current-generation climate models have improved this aspect of the simulation compared to the CMIP3 models, there are still erroneous El Niño peaks during the rest of the year. ADD CITATION. The failure of models to correctly simulate the annual cycle-ENSO phase locking has been associated with a poor simulation of the annual cycle in SSTs in the eastern Pacific (Ham and Kug, 2014). Also of interest in correctly simulating ENSO, the current generation of climate models now is more likely to simulate the location of maximum ENSO variability further to the east than the previous versions (Bellenger et al., 2014). This is joined by an improvement in simulating a diversity of ENSOs (CP and EP), although it is still a topic of discussion as to whether the diversity of El Niño maximum amplitude locations is a continuum (Ray and Giese, 2012; Johnson, 2013; Fedorov et al., 2014) or two distinct flavors (Ashok et al., 2007; Ren and Jin, 2011; Takahashi et al., 2011). That debate and overall amplitude issues aside, the climate models tend to simulate the correct amplitude longitude of maximum anomaly relationship–namely, that the further east the maximum SST anomaly is, the larger the SST anomaly.

1.5 Objectives and Approaches

Great progress has been made in understanding and simulating ENSO. However, many issues remain unresolved in terms of understanding ENSO, for example ENSO asymmetry, pattern, and temporal diversity both in the observational record and in GCMs. The overarching objective of this dissertation is to better understand the role of ENSO state-dependent noise in contributing to this diversity. To achieve this objective, I will use a systematic approach to quantify the state-dependence of the noise-ENSO interaction. It includes testing a method that estimates the state-dependence factor of ENSO noise

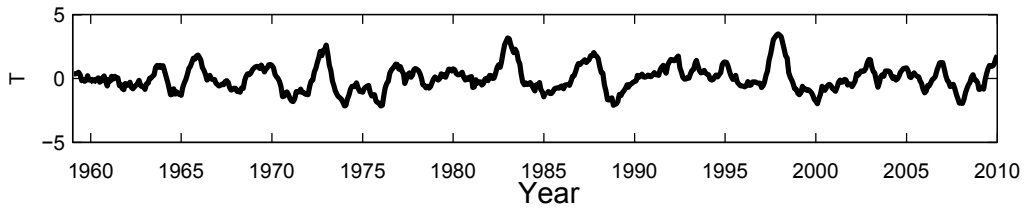

Figure 1.1: A time series of the Niño3.4 Index over the last 60+ years. To first order, ENSO has an oscillatory nature, but the observed record shows significant assymmetries in magnitude and duration.

in a conceptual model. Secondly, the methodology for estimating the state-dependence factor will be applied to reanalysis and two CGCMs. Thirdly, utilizing the results from this analysis, I will explore the physical processes involved in creating and amplifying multiplicative noise within the system and compare the results to previous studies of WWBs and multiplicative noise. Fourthly, I will examine the state-dependence factor of multiplicative noise in 21 different CMIP5 models. The Pre-Industrial Control simulation and two different emissions pathways will be examined in order to study the effects of global warming on the state-dependence factor and potential changes to ENSO. Finally, I will examine how the interaction between ENSO and the multiplicative component of noise generates extreme El Niño events.

Chapter 2

A Simple Method for Estimating the State-Dependency of ENSO Noise

2.1 Introduction

Examining a phenomenon with a conceptual model can be useful for determining the role of different components in creating the phenomenon. The conceptual model makes predictions that can then be tested in the observed phenomenon. As previously discussed, there are two different major conceptual models for ENSO. These models, the delayed action and recharge oscillators, have focused on different physical processes that have been observed as integral parts of ENSO. These conceptual models have been shown to be equivalent means of describing ENSO. This dissertation will use the recharge oscillator as the conceptual model. Equation 2.1 shows a simple recharge oscillator system of ENSO where T represents ENSO state, h the thermocline depth anomaly, λ represents

the Bjerknes positive feedback and ω represents the frequency.

$$\begin{aligned} \frac{dT}{dt} &= -\lambda T + \omega h + \Sigma F_i \\ \frac{dh}{dt} &= -\omega T \end{aligned} \tag{2.1}$$

This form of the recharge oscilator is derived from a two box model (Jin, 1997a; Burgers et al., 2005). As such it is unable to capture the diversity of ENSO flavors that have been observed. However, its simplicity has allowed it to be solved analytically (Jin, 1997b; Jin et al., 2007; Levine and Jin, 2010). The third term in the temperature tendency equation, ΣF_i, is where any or all forcing terms can be added to the equation. If $\Sigma F_i = 0$, the model produces a symmetric ENSO. By adjusting ΣF_i, different non-linearities can be examined for their effect on ENSO independently and in combination. The shape and type of this forcing term will be the subject of this dissertation. In this chapter, I will consider the conceptual recharge oscillator model with different strengths of multiplicative noise and develop a model to estimate the magnitude of the multiplicative noise from observations.

2.2 Multiplicative Noise in the Recharge Oscillator

Multiplicative noise forcing of ENSO was explored in this simple conceptual recharge oscillator model in Jin et al. (2007) and Levine and Jin (2010). In their studies, they used a simple parameterization of multiplicative noise to force the recharge oscillator equations (Equation 2.2).

$$\begin{aligned} \frac{dT}{dt} &= -\lambda T + \omega h + \sigma_N \xi(t) G \\ \frac{dh}{dt} &= -\omega T \\ \frac{d\xi}{dt} &= -r\xi + w(t) \end{aligned} \tag{2.2}$$

Where G is the multiplicative term and xi is the noise. This version of the model differs from the version used in Levine and Jin (2010) in the values of the constants. Here we use $\lambda = 2$ year^{-1}, $r = 8$ year^{-1}, $\sigma_N = 1.75\sqrt{6}$ year^{-1}, and $\omega = \frac{\pi}{2}$ year^{-1}. Since $r = 8$

year^{-1}, the conceptual model is forced with red noise, which has increased power at low frequencies compared with higher frequencies. If r were instead set to 360 year^{-1}, the noise forcing would be white. White noise has a constant amount of energy at all frequencies. The values of the constants were chosen so that in the additive noise case, $G = 1$, the standard deviation of T is 0.81, similar to that of the Niño3.4 region in reanalysis. Jin et al. (2007) and Levine and Jin (2010) used a multiplicative noise term $G = 1 + BT$, where B is the SST-dependent factor of multiplicative noise. Here, I also consider a different shape of the multiplicative noise term, $G = 1 + BTH(T)$, where $H(T)$ is a Heaviside function.

The inclusion of this threshold non-linearity in the noise forcing term, $\sigma_N \xi(t) G$, can be physically interpreted as changes in the magnitude of the windstress anomaly depending on the anomalous temperature only during the El Niño phase. The multiplicative nature of the threshold non-linearity comes as a consequence of the convective process associated with the generation of transient windstress in the western and central Pacific. Transient windstress, in the form of WWBs, is generated by convective events. Convection has a minimum threshold around the average temperature in this region and thus positive temperature anomalies are able to trigger convection and the westerly wind anomalies to the west of the convection. Negative temperature anomalies cause little change in the windstress forcing because convection is already absent from this region. Further, these anomalies are multiplicative, meaning that when one convective event occurs, it changes the underlying ENSO state such that a following convective event is more likely to occur and be stronger than it would be in the absence of the first event. The observed increased variability in the windstress during strong El Niño events is something that can be represented as the multiplicative noise forcing of ENSO.

A consequence of multiplicative noise, particularly in the form that has been used to modify the forcing of El Niño in the conceptual model, is that after the initial noise forcing event a second strong forcing event becomes more likely. This can be demonstrated by comparing the difference between the additive noise case ($B = 0$) and the multiplicative case ($B = 0.5$) in the conceptual model. The standardized histograms of the noise forcing one, two, and three months after a large noise event ($\xi > \sigma(\xi)$) are examined

and compared with the standardized histogram of the full ξ distribution (Figure 2.1). The standardized histogram of the total red noise time series is Gaussian. However, selecting the times immediately following a large noise event modifies the distribution. In the additive case, the width of the distribution does not change much. The mean of the distribution is shifted positively and the frequency of occurrence of events around the shifted mean is significantly increased. From this, we can see that red noise plays a role in increasing the likelihood of long-lasting anomalous westerly wind forcing. The results of the multiplicative, $B = 0.5$, case show an even more significant change in the distribution of noise forcing. In the months following a large noise forcing event, not only is the mean of the distribution shifted like we see for the additive case, but the width and skewness of the distributions are significantly altered creating a large impact in the extreme positive tails of the noise forcing distribution. Thus, multiplicative noise significantly increases the likelihood that the future noise will be even larger, playing a role in enhancing the low-frequency component of the noise.

2.3 A Method for Calculating the State-Dependent Factor, B

Using the conceptual model, three typical solutions under different multiplicative noise forcing are considered. For each case, a 50-year segment from a longer 10,000 year simulation is shown. The result for the case with only additive noise, $B = 0$, is shown in Figure 2.2 (a). From the temperature (upper left panel) and noise forcing (lower left), there are a few El Niño events that occur and the noise forcing has a lot of variability. Using the time series of temperature and noise forcing, $G\xi$, we have a pair of points $(T(t_i), G(t_i)\xi(t_i))$ for each sample time i. These points are then binned based upon $T(t_i)$. The bin widths are chosen to give an approximately equal number of points per bin assuming that the temperature has a Gaussian distribution. While T is not Gaussian, this approximation gives enough points per bin at the larger values and enough bins at the smaller values of T. The standard deviation of the associated values of $G(t_i)\xi(t_i)$

are then calculated for each bin. Any bin with fewer than 15 points is discarded from the analysis. Using this method for binning, the standard deviation of $G\xi$ for each bin is then plotted against the center value of the T bin. The standard deviations of $G\xi$ as a function of T for the same 50-year sample period are estimated as the dots on the right in Figure 2.2(a). The exact distribution of the standard deviations of $G\xi$ is shown as the solid black line. In the additive noise case, the standard deviation of $G\xi$ does not depend on temperature. A second method of calculating the standard deviation of $G\xi(T)$ was also used. This method held the number of points per bin constant at 15 and $\bar{T}$ and the standard deviation of $G\xi$ for each bin was calculated. The results are similar (Figure 2.3). The fixed bin width method was chosen for the ease of comparing between different cases since the constant points per bin method would have changing values on both the x and y-axes while the the constant bins method has changing values only along the y-axis. For increased, applicability I have averaged the output of the conceptual model to produce monthly mean data from daily forcing to use in the calculation of B. This change does not affect the results.

The solution and the same analysis for the case where $G = 1 + 0.5\ T$ are shown in Figure 2.2(b). Focusing on the standard deviations of $G\xi$ as a function of T (right column), it is shown that in this case the standard deviation of $G\xi$ is no longer constant. It reaches its minimum at a value of $BT = -1$ and increases in value when T is either greater than or less than that value. The slopes of the lines defined by those points on either side of the minimum are theoretically equal. This is approximately true in the 50-year sample period depicted here. Similarly, in Figure 2.2(c), I show the same information but for the case where $G = 1 + .5\ TH(T)$. Comparing the standard deviations of $G\xi$ (right column) between cases (b) and (c), the effect of the threshold non-linearity can be detected. Instead of having a minimum value of the standard deviation of $G\xi$ at $BT = -1$, at $T = 0$ the standard deviation of $G\xi$ flattens out and is nearly constant for all of the bins with $T < 0$.

To estimate the value of B, the standard deviation of the noise as function of the El Niño state is used. The standard deviations of $G\xi$ with respect to the Niño index are first calculated, these are represented by the circles. They are then piecewise linearly

regressed (all of the bins with negative values of T are grouped into one regression and all of the bins with a positive value of T are grouped into a second one) onto the same Niño index. The y-intercepts of these two regressions are averaged and represent an estimate of the noise standard deviation. The positive side linear regression is then repeated but with the y-intercept forced to equal the y-intercept of the of the negative regression. B is equal to the slope of the latter regression divided by the noise standard deviation (Figure 2.4).

To test the robustness of this estimation method, I have performed a number of 10,000-year simulations in the conceptual model at different values of B with $G = 1 + BTH(T)$. Each 10,000-year simulation has been subdivided into 200 separate, non-overlapping 50-year intervals. The estimated value of B is calculated for each of these intervals and then compared with the actual value used in the conceptual model. The estimated value from the full 10,000-year simulation and the standard deviation of the sub-intervals are shown in Figure 2.5 where the actual value is shown as the straight line. It shows that the value of B can be estimated with a 50-year data length with reasonable accuracy. The accuracy over 50 years data length is important because it allows for the utilization of this method to estimate the value of B in short data sets such as the reanalysis products.

2.4 The Effect of Daily vs. Monthly Mean Sampling

While phenomena associated with noise forcing of ENSO (MJOs, WWBs, etc.) are typically thought of as short-timescale processes, in order to actually force ENSO, they must have energy in the lower ENSO frequencies (Roulston and Neelin, 2000; Levine and Jin, 2010). Therefore, the loss of high-frequency information by using the monthly mean as opposed to daily or pentad data should be unimportant. To test this hypothesis, the conceptual model is used and the daily noise forcing is compared to the monthly mean values. In estimating the value of B, the uncertainty in the estimation is slightly reduced but the mean of the estimate from 200 50-year samples remains nearly constant (Figure 2.6). Over longer time periods for estimation, the daily data reduce the uncertainty even

less.

2.4.1 Sampling Versus Natural Noise Characteristic Time Scale

The use of the monthly mean is further tested by examining the effect of the noise decorrelation time scale on the estimation of B in both monthly and daily noise estimations. The decorrelation timescale of the noise, r in equation 2.2, sets the self-organization properties of the noise and is the difference between white and red noise. The default time scale used throughout this chapter is 45 days. Sensitivity tests are run with it set to 30, 15, and 10 days. The noise amplitude is normalized such that

$$\sigma = \sigma_0 \sqrt{\frac{r}{r_0}} \tag{2.3}$$

where σ_0 and r_0 are the values of σ and r for 45 days. This normalization is used because the ENSO growth rate with multiplicative noise is $Gr = \frac{\frac{\sigma^2 B^2}{r} - \lambda}{2}$ (Jin et al., 2007; Levine and Jin, 2010). Both daily and monthly mean data are stored from the sensitivity tests. The value of B estimated using the monthly mean noise forcing is not sensitive to the noise decorrelation time scale. With the daily data, the value of B is not very sensitive to the noise decorrelation time scale for $r > 10$ days (Figure 2.7).

2.5 Isolating the Windstress Noise Forcing

From Frankignoul and Hasselmann (1977), it is known that variability existing on timescales much shorter than ENSO can be treated as stochastic forcing. There are many potential sources from both the atmosphere and the ocean for this stochastic noise forcing of ENSO. This dissertation will focus on only one of these sources, the transient (not directly related to ENSO) equatorial windstress. During ENSO, there is a strong zonal wind response in the central and western Pacific. This response is directly proportional to ENSO SSTs and not stochastic. Therefore, the windstress is split into two components.

$$\tau = \tau_D + \tau_R \tag{2.4}$$

τ_D denotes the deterministic response of the central Pacific windstress to ENSO SSTs and τ_R is the remaining component of the windstress or the windstress noise. Choi et al. (2013) showed that there is both a linear and threshold non-linear response of the windstress to ENSO SST anomalies. This is one component of the deterministic response.

$$\tau_1 = \mu_1 T + \mu_2 H(T) T \tag{2.5}$$

Additionally, Stuecker et al. (2013) showed the existence of annual cycle-ENSO combination tones in the tropical Pacific SST-spectra. They showed that the combination tones play a large role in the El Niño-La Niña transition. As such, they have strong weighting when El Niño is near its peak and a much smaller weighting during La Niña and thus could be a source of the windstress variance asymmetry instead of the multiplicative noise forcing. These combination tones are from the linear combination of the ENSO and annual cycle frequencies and show up in the per annum spectrum at the values of $1 \pm Cf$, where C is any integer and f is the ENSO frequency. The strongest of these occur when $C = 1$. This will be considered and removed.

$$\tau_{AC} = \mu_{AC} T cos(\omega_{AC} t) \tag{2.6}$$

Because the noise forcing generation region of ENSO is in the western and central Pacific, there is also the potential for a forcing from the semi-annual cycle. Combining these different deterministic responses of the windstress to ENSO SST anomalies, it is proposed that

$$\tau_D = \mu_1 T + \mu_2 H(T) T + \mu_{AC} T cos[\omega_{AC}(t - t_{AC})] + \mu_{SAC} T cos[2\omega_{AC}(t - t_{SAC})] \tag{2.7}$$

where ω_{AC} is the annual cycle frequency and t_{AC} and t_{SAC} are the number of months that the annual cycle and the semi-annual cycle are offset from the ENSO peak.

The conceptual model affords the opportunity to test a method for determining the coefficients μ_1, μ_2, and μ_{AC}. A windstress timeseries, τ, is created in the form of equation

2.5, with

$$\begin{aligned} \tau_D &= A_0 T + A_N H(T) T + A_{AC} T cos(\omega_{AC} t) \\ \tau_R &= A_R \xi (1 + B H(T) T) \end{aligned} \tag{2.8}$$

A_0 is set to 1 and the rest of the coefficients are chosen such that they are correctly proportional to A_0, with $A_N = \frac{1}{5}$, (Choi et al., 2013), $A_{AC} = \frac{1}{3}$ Stein (2008), $A_R = 1$, and $B = 0.5$. According to Stuecker et al. (2013), the combination tone and the direct ENSO response are orthogonal to each other. Because of this, the combination tone, $A_{AC} T cos(\omega_{AC} t)$ can be treated separately from the rest of Equation 2.8 as part of a multiple linear regression. However, since $A_0 T$ and $A_N H(T) T$ are not orthogonal to each other, a simple multi-linear regression does not work. Instead the covariance matrix is set up and A_0 and A_N are solved for.

$$\begin{pmatrix} A_0 a_{11} & A_N a_{12} \\ A_0 a_{21} & A_N a_{22} \end{pmatrix} = \begin{pmatrix} F_1 \\ F_2 \end{pmatrix} \tag{2.9}$$

where

$$\begin{aligned} a_{11} &= \overline{T T(t - t_0)} \\ a_{12} &= \overline{H(T) T T(t - t_0)} \\ a_{21} &= \overline{T H(T(t - t_0)) T(t - t_0)} \\ a_{22} &= \overline{H(T(t - t0)) T(t - t_0) H(T) T} \\ F_1 &= \overline{\tau T(t - t_0)} \\ F_2 &= \overline{\tau H(T(t - t_0)) T(t - t_0)} \end{aligned} \tag{2.10}$$

and t_0 is a lag based on the principle that the future noise is uncorrelated with the

present state. Solving the system of two equations and two unknowns yields

$$\begin{aligned} A_0 &= (\frac{a_{22}}{a_{12}}F_1 - F_2)\frac{1}{\frac{a_{11}a_{22}}{a_1 2} - a_{21}} \\ A_N &= (\frac{a_{21}}{a_{11}}F_1 - F_2)\frac{1}{\frac{a_{12}a_{21}}{a_1 1} - a_{22}} \end{aligned} \tag{2.11}$$

When equation 2.11 is solved for with $t_0 = 2$, $\mu_1 = A_0$. Equation 2.11 is then solved for again with $t_0 = 0$ and $A_N = \hat{\mu_2}$. An estimate of the linear and threshold non-linear terms are then removed from the windstress, τ.

$$\hat{R_1} = \tau - \mu_1 T - \hat{\mu_2} H(T)T \tag{2.12}$$

After removing the linear and threshold non-linear terms from the windstress, the combination tone is then removed using a simple linear regression.

$$\hat{R_\tau} = \hat{R_1} - \hat{\mu_{AC}} T cos(\omega_{AC} t) \tag{2.13}$$

However, as it is currently calculated, the estimate $\hat{\mu_2}$ has a dependence on B, as shown in the simplified system,

$$\begin{aligned} Y &= A_N H(T)T + A_R[1 + BH(T)T]\xi \\ &= (A_N + A_R B\xi)H(T)T + A_R\xi \end{aligned} \tag{2.14}$$

To account for this,

$$\mu_2 = \hat{\mu_2} - A_R \hat{B} \tag{2.15}$$

where $\hat{B}$ is an estimate for the state-dependence factor caculated from the timeseries, $\hat{R_\tau}$, using the method outlined in section 2.3 and $A_R = \frac{\sigma(\hat{R_\tau})}{.66}$. Then R_1, μ_{AC}, and R_τ are calculated by repeating equations 2.12 and 2.13 with the updated value of μ_2 from equation 2.15. The new value of R_τ is then used to calculate the state-dependence factor, B.

Figure 2.8 shows the spectra of τ, R_τ, and $[1 + BH(T)T]\xi$. The τ spectrum shows

the additional energy added to the noise spectrum, $[1 + BH(T)T]\xi$, by τ_D. This extra power is most visible around the low frequencies where there is large scale temperature variability. The combination tones are also very evident in the spectrum of τ. The spectrum of R_τ shows that the energy in the combination tones and the ENSO driven deterministic windstress forcing can be removed by the method outlined above. To examine the ability of the method to correctly estimate the deterministic component of the noise forcing correctly, the relationship between τ_D and $\hat{\tau_D}$ is shown(Figure 2.9). This relationship is linear and is very close to the line of $\hat{\tau_D} = \tau_D$ with a slight overestimation of $\hat{\tau_D}$. Additionally, the relationship between the $[1 + BH(T)T]\xi$ and R_τ is examined (Figure 2.10). Like the estimate of τ_D, the estimate of the noise forcing, R_τ, is also fairly accurate. In this case, consistent with the overestimation of τ_D, there is a corresponding slight underestimation of R_τ. Since the goal of the study is to examine the noise forcing of ENSO, the actual and estimated noise forcing are composited over the extreme El Niño events in the conceptual model. Like the results in Figure 2.10, the recovered noise, R_τ, slightly underestimates the actual noise (Figure 2.11). Another method of examining the bias in the estimation of the noise is to compare the actual and estimated noise forcing over a time period. The 50-year time sample from the conceptual model also agrees with the rest of the results (Figure 2.12). There is an underestimation of the noise forcing related to the overestimation of the deterministic component. This underestimation is most pronounced when the temperature is larger. This bias of a slight underestimation of the noise amplitude during the growth phase will effect some of the results presented in later chapters. However, being an underestimation, it suggests that the results in the following chapter for the noise forcing should be even stronger than presented. Further, the bias in the deterministic component does not create a bias in the estimation of the state-dependence factor, B (Table 2.1).

2.5.1 The Impact of a Different Form of Non-Linearity

The conceptual model can also be used to test how well the linear approximation captures a more complicated non-linear deterministic term. The forcing term in the temperature

equation in 2.1 is set to include a non-linear deterministic component and linear deterministic component.

$$\tau_D = \mu_{NL} tanh(T) + \mu T \tag{2.16}$$

These two components are removed using the linear and threshold non-linear regression method that is applied to the timeseries. The non-linear deterministic component of the forcing cannot reproduce the changes in the standard deviation of the noise as a function of the ENSO state as seen with the multiplicative noise (Figure 2.13). However, the non-linear deterministic component can amplify the multiplicative noise signal if it is already present. If the shape of the non-linear deterministic dependence of the forcing on ENSO were already known, the non-linear component could be removed. Based on the work of Choi et al. (2013), this non-linear deterministic component is chosen to be a threshold non-linearity. However, this uncertainity is a limitation of the noise isolation method being used.

2.6 Summary

This chapter has introduced the conceptual recharge oscillator model with and without multiplicative noise. The changes in the standard deviation of the noise forcing as a function of ENSO state has been used to develop a method to use the monthly mean noise forcing to estimate the state dependence factor of the multiplicative noise, B. This method has been shown to be accurate over subsamples of 50 years. The conceptual model has been used to show that monthly mean data are acceptable to describe multiplicative noise even when daily data are available. An additional method has been developed to isolate the noise forcing from a deterministic component containing a linear, a threshold non-linear, and a combination tone. The method has been shown to estimate the coefficients of the different parts of the deterministic timeseries reasonably accurately and slightly underestimate the total noise forcing. These methodological biases do not bias the estimate of the state-dependence factor.

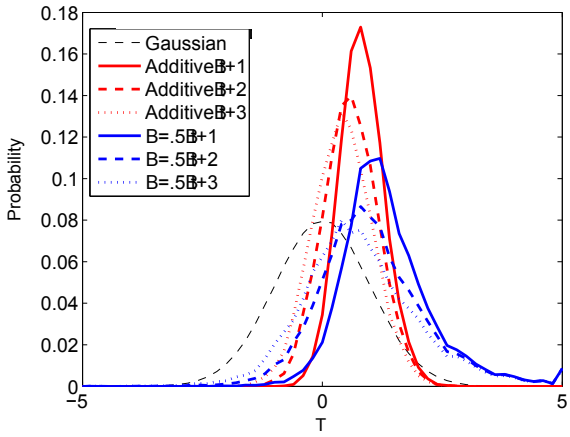

Figure 2.1: The standardized histogram of noise for 1 (solid), 2 (dashed), and 3 (dotted) months following a large noise event for additive, $B = 0$ (red), and multiplicative, $B = 0.5$ (blue), noise. The additive noise and the multiplicative noise both are different from the total noise PDF, which is Gaussian. Further, in the multiplicative noise case, the positive tail is greatly enhanced at all lags.

Table 2.1: Median value of the coefficients of deterministic noise as a function of length of observation period.

	Actual	50	100	200	400
A_0	1	1.16	1.13	1.13	1.11
A_n	0.20	0.11	0.15	0.19	0.19
A_{AC}	0.33	0.33	0.33	0.33	0.33
$\sigma(R)$	1	1.08	1.11	1.12	1.12
B	0.5	0.45	0.43	0.45	0.46

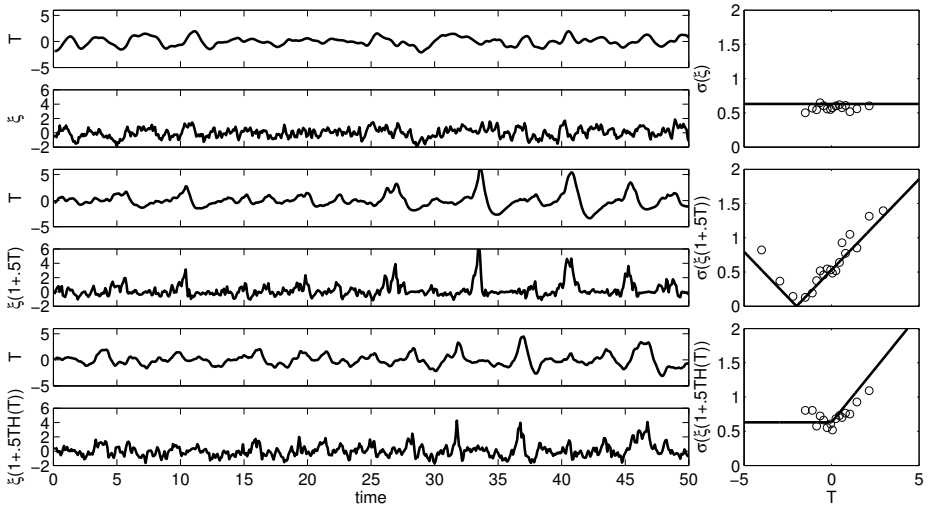

Figure 2.2: (a) Simulated time series of temperature (upper left) and the noise forcing (lower left) from a sample 50-year period in the 10,000-year simulation with $B = 0$. On the right, the conditional standard deviation of $G\xi$ for the same 50-year period (circles). The solid line represents the theoretical distribution of the standard deviation of $G\xi$ as a function of T. (b) the same as (a) but for $G = 1 + 0.5T$. (c) the same as (a) but for $G = 1 + 0.5TH(T)$.

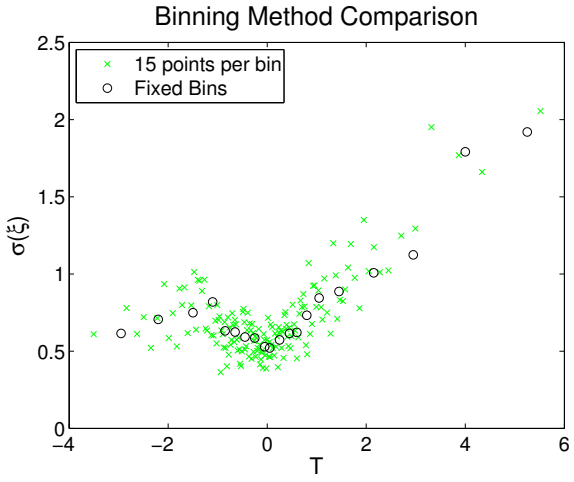

Figure 2.3: Comparison of the conditional standard deviation as a function of ENSO state when the bins are set at a fixed number of points per bin and when the bins are given a set bin width. The overall shape in both cases is the same.

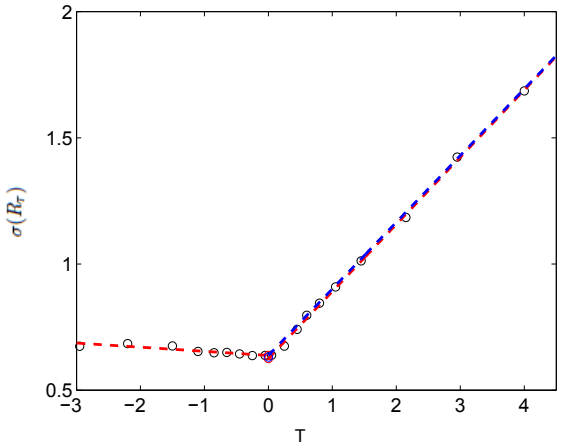

Figure 2.4: Schematic diagram of the methodology for estimating B. The red o are the different intercepts that get averaged for the normalization, red dashed lines are the initial linear regressions, and the blue dashed line is final linear regression.

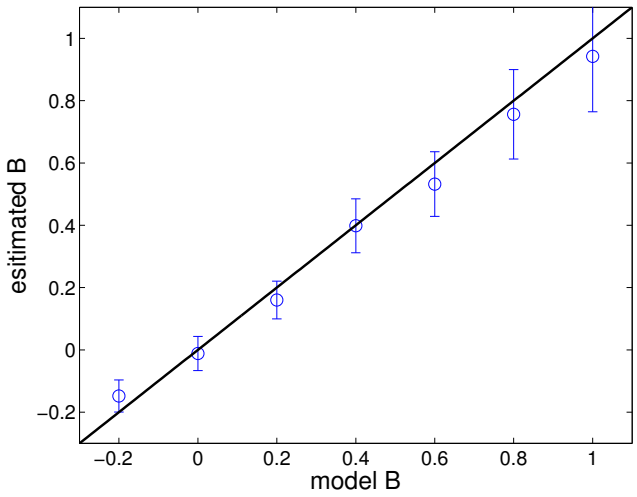

Figure 2.5: Using 200 segments of 50 years of monthly mean data from a 10,000-year simulation, the estimated B, including its ensemble mean (circles) and standard deviation (error bars) are shown. The actual value is shown as the straight line.

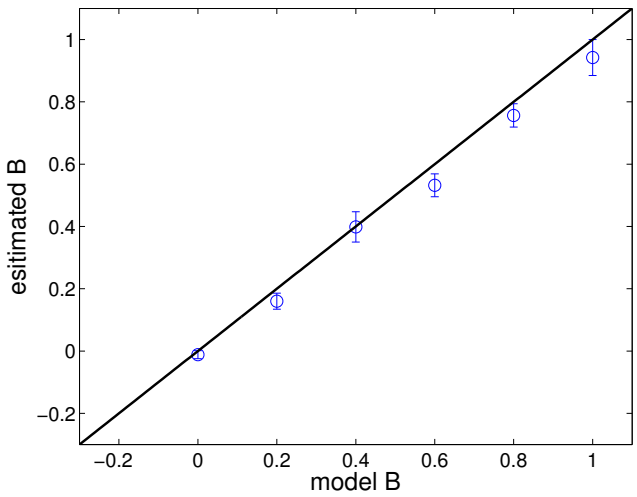

Figure 2.6: Using 200 segments of 50 years of daily data from a 10,000-year simulation, the estimated B, including its ensemble mean (circles) and standard deviation (error bars) are shown. The actual value is shown as the straight line. The error of the estimate is only slightly reduced by using daily data as opposed to monthly data.

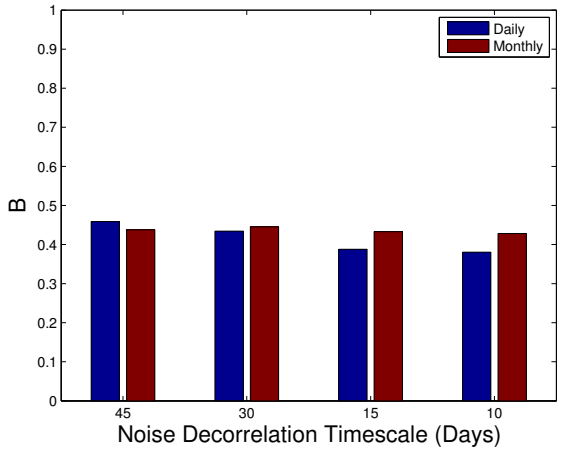

Figure 2.7: A comparison of the estimated B from daily and monthly data dependent for different noise decorrelation timescales. Neither the distinction between daily or monthly data nor the noise decorrelation timescale effects the estimate of B significantly.

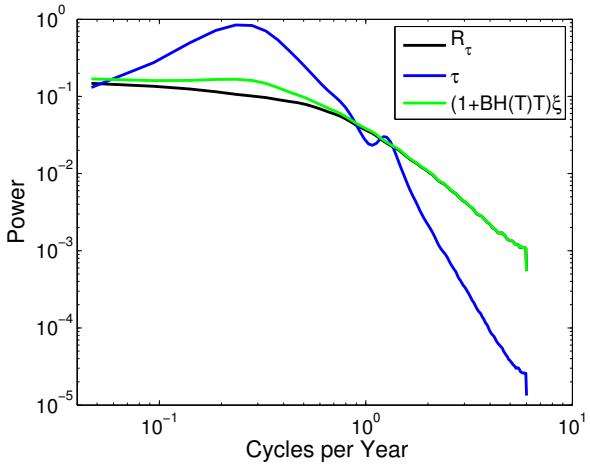

Figure 2.8: The spectra of τ, R_τ, and $[1 + BH(T)T]\xi$ from the created windstress $\tau = A_0T + A_NH(T)T + A_{AC}Tcos(\omega_{AC}t) + A_R[1 + BH(T)T]\xi$. The results show that the methodology outlined here can be used to estimate the windstress noise in the presence of a deterministic windstress.

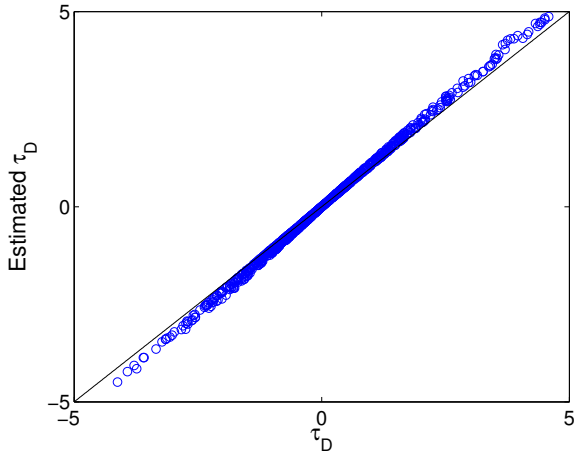

Figure 2.9: Scatter plot τ_D versus the estimated τ_D from the created windstress $\tau = A_0T + A_NH(T)T + A_{AC}Tcos(\omega_{AC}t) + A_R[1 + BH(T)T]\xi$ where τ_D is the deterministic component of τ. The results show that the methodology outlined here can be used to estimate the windstress noise in the presence of a deterministic windstress.

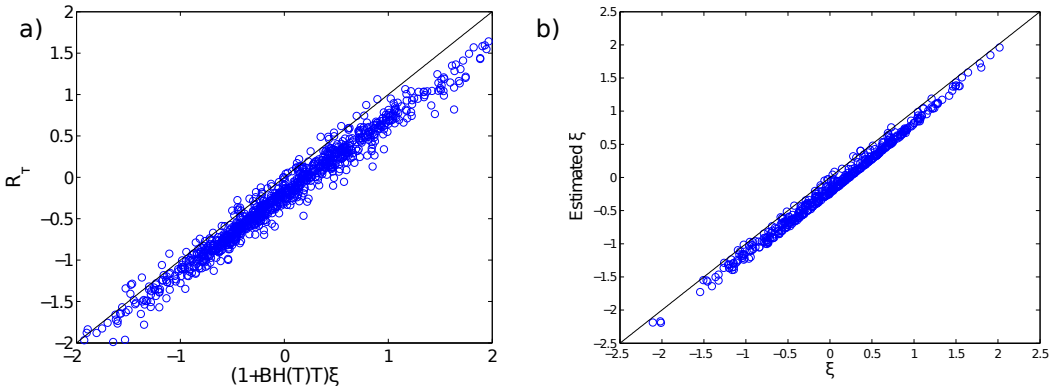

Figure 2.10: a) Scatter plot $(1 + BH)T)\xi$ versus R_τ from the created windstress $\tau = A_0T + A_NH(T)T + A_{AC}Tcos(\omega_{AC}t) + A_R[1 + BH(T)T]\xi$. b) Scatter plot of ξ versus estimated ξ. ξ is estimated using as $\xi = \frac{R_\tau}{1+BH(T)T}$. The results show that the methodology outlined here can be used to estimate the windstress noise in the presence of a deterministic windstress. Additionally, the noise can be split into additive and multiplicative components.

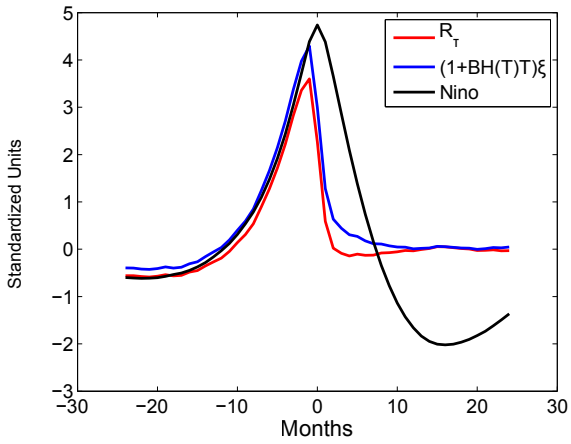

Figure 2.11: The composite noise forcing of extreme El Niño events comparing $(1 + BH)T)\xi$ and R_τ from the created windstress $\tau = A_0T + A_NH(T)T + A_{AC}Tcos(\omega_{AC}t) + A_R[1 + BH(T)T]\xi$. The results show that the methodology outlined here can be used to estimate the windstress noise in the presence of a deterministic windstress.

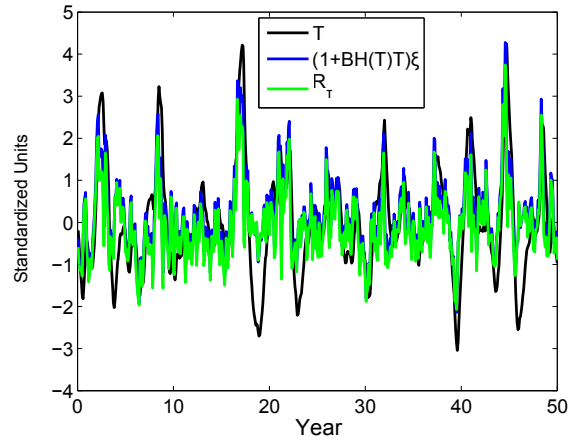

Figure 2.12: A 50-year timeseries from the conceptual model of T, $(1 + BH)T)\xi$, and R_τ from the created windstress $\tau = A_0T + A_NH(T)T + A_{AC}Tcos(\omega_{AC}t) + A_R[1 + BH(T)T]\xi$. The results show that the methodology outlined here can be used to estimate the windstress noise in the presence of a deterministic windstress.

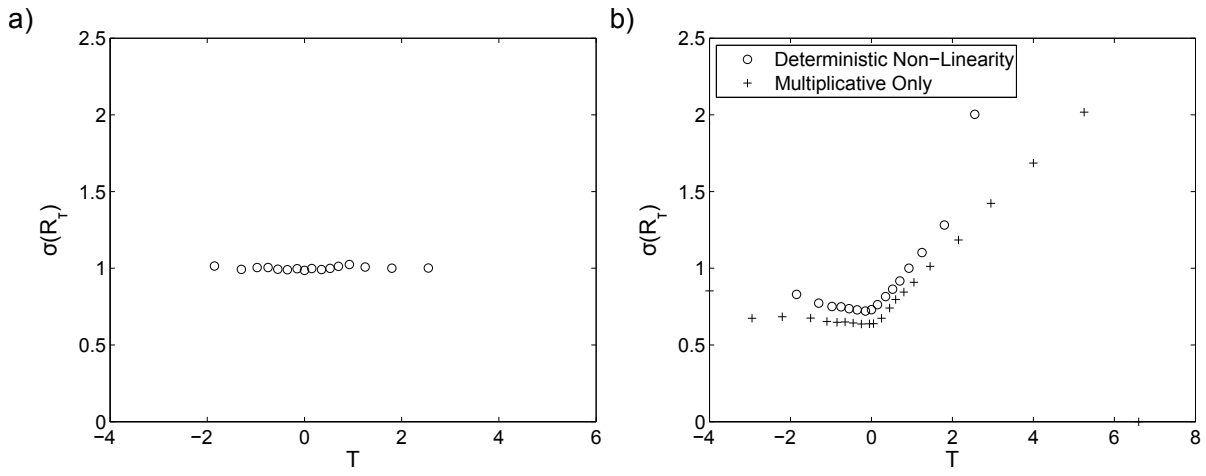

Figure 2.13: Standard deviation of the noise as a function of temperature at a) $B = 0$ and b) $B = 0.5$ for a deterministic non-linear forcing term. At $B = 0$, the deterministic non-linear forcing term has no effect on the conditional standard deviation.

Chapter 3

The Diagnosis of State-Dependency of ENSO Wind Stress Noise in Reanalysis and Two GCMs

3.1 Introduction

In the previous chapter, a method was developed to diagnose the state-dependency of the wind stress noise. In this chapter, the method will be utilized to estimate the state-dependency of the ENSO wind stress noise. In order to accomplish this, the ENSO wind stress noise will be isolated from the total wind stress using the method outlined in Chapter 2. The resultant wind stress noise is tested and found to have a state-dependent component.

3.2 Data

The windstress data used in this study are the European Centre Reanalysis 40-year reconstruction (ERA-40), which is available at a horizontal resolution of 2.5 degree x 2.5 degree (Uppala et al., 2005). The current and temperature data used to calculate the zonal advection of temperature come from the ECMWF Ocean Reanalysis System 3 (ORA-S3) and are on a 1 degree x 1 degree horizontal grid with the upper 5 levels representing the upper 50 m of the ocean (Balmaseda et al., 2008). The SST time series comes from the HadISST sea surface temperature reconstruction on a 1 degree x 1 degree grid (Rayner et al., 2003). The first principal component of the empirical orthogonal function analysis of the SST anomalies from 120E-80W and 10S-10N is used as the Niño index. This time series is representative of ENSO events and correlates highly with the Niño 3.4 time series (r=0.97).

In addition to Reanalysis data, two GCMs, Community Climate System Model 4 (CCSM4) and Geophysical Fluid Dynamics Laboratory (GFDL) CM2.1, are used. 400 years from the pre-industrial control integration of CCSM4 and 300 years from the CM2.1 1990-control integration are used. The atmospheric component of CCSM4 is run at 2 degree resolution and the ocean component is run at a nominal 1 degree resolution, with higher resolution in the tropics and 15 vertical levels in the upper 150m of the ocean (Gent et al., 2011). The atmospheric component of CM2.1 has 1 degree resolution and the oceanic component has variable resolution in the ocean reducing to less than half a degree at the equator (Delworth and coauthors, 2006). Both models have large and active ENSO representations.

3.3 Windstress Noise Forcing in Reanalysis and Two GCMs

Here the methodology from Chapter 2 is extended to these datasets and the windstress is assumed to take the form of Equation 2.7. In the conceptual model, the assumption of red noise forcing was made. Examining the spectra of R_τ, it can be seen that the windstress noise forcing that was isolated does indeed have a noise component with a red

noise type spectrum reducing to a white noise spectrum at frequencies higher than a few months for both the Reanalysis and the models (Figure 3.1). All of the different noise spectra show variability at high frequencies, but this difference is inconsequential since high frequency energy alone is unable to excite ENSO (Levine and Jin, 2010; Roulston and Neelin, 2000). The noise spectra are in stark contrast to the ENSO spectra which peaks at ENSO frequencies and reduces much more at higher frequencies than the noise forcing.

Additionally, the standardized histogram of R_τ was examined (Figure 3.2). R_τ is approximately Gaussian, although slightly peaked with a greater percentage of events closer to zero and less weighting in the tails of the distribution. Levine and Jin (2010) tested noise distributions with similar properties, only more extreme, and found that at values of $B < 1$ it had little effect on ENSO stability or ENSO extreme events. Therefore, these small deviations from gaussianity can be ignored.

Further examination of the standardized histogram of the noise forcing after a large noise forcing event ($R_\tau > \sigma(R_\tau)$) in the Reanalysis and coupled models, show changes that are similar to the conceptual model with multiplicative noise changes (Figure 3.3). Following a large noise forcing event, the median value of the noise has a positive shift and the positive tail is significantly enhanced. This is similar to what has been observed in the windstress noise forcing after multiplicative events and during the growth phase of strongest El Niño on record McPhaden (1999). This will be explored in greater detail in the next chapter. These differences are consistent with the multiplicative noise used in the conceptual model and suggest that it is possible to deduce the strength of the SST state dependent constant of multiplicative noise forcing from the time series using the method previously outlined.

3.4 Spatial Distribution of Noise

The spatial pattern of μ_1 shows the expected weakening of the Walker circulation with a strong increase in anomalous westerlies over the central Pacific dependent on ENSO phase (Figure 3.4). μ_2 shows a strong east-west dipole in its application of the ENSO

state to the windstress field (Figure 3.5). This is due to the changes in mean SST between the eastern and western Pacific. In the eastern Pacific, changes in convection are asymmetrically triggered by only positive SST anomalies. These results are consistent with Choi et al. (2013). The annual cycle combination tone has a hemispherically asymmetric pattern in the windstress (Figure 3.6). Both the pattern and the magnitude are similar across the different offsets in the Reanalysis data sets, due to the overall uncertainty within the combination tone over the short record of the Reanalysis data product. The pattern and offset for the Reanalysis and CM2.1 are in good agreement with the results from Stuecker et al. (2013), but in CCSM4 the combination tone is has a different spatial pattern and offset from Reanalysis and CM2.1. The semi-annual cycle combination tone has a similar sign reaction to El Niño in the South Pacific Convergence Zone and ITCZ and an opposite sign reaction in the central Pacific around the equator (Figure 3.7). The patterns of these different signals are consistent across the Reanalysis and the models.

Levine and Jin (2010) showed that the noise amplitude plays a role in the overall impact of multiplicative noise on ENSO. The standard deviation of R_τ of the tropical Pacific is examined (Figure 3.8). The windstress noise variability increases from east to west across the Pacific peaking in the central Pacific along the warm pool edge. Attention is focused on the equatorial region as the generation region of the Kelvin wave forcing of ENSO and the windstress noise forcing is averaged over the region of 160° E-160° W and 3° S-3° N. This area contains the most active region of windstress noise forcing. This region is along the warm pool edge where small changes in SST can have large impacts on the location of convection in the equatorial Pacific Ocean. This region is also consistent with the findings of Kug et al. (2008).

3.5 Calculating B for the Reanalysis and the Two Models

Having isolated a noise time series, it is compared with the Niño time series (Figure 3.9a). The residual time series has significant variability on short time scales and large peaks associated with the major El Niño events in 1982-3 and 1997-8, which is indicative of a relationship between the noise forcing and El Niño. There are peaks in the noise forcing

that are not associated with the peaks of the strong El Niño events in the record, the noise forcing is not solely dependent on ENSO state. Figure 3.9b and 3.9c show similar 50 year segments of CM2.1 and CCSM4, respectively. In both cases, comparing the windstress noise forcing time series and the temperature time series, the largest values of the noise forcing term are found to be contemporaneous with the onset of strong El Niño events as was seen in the Reanalysis with the 1982 and 1997 El Niño events. Again, these time series show peaks prior to the peak of the strong El Niño events, but there are additional peaks that are unassociated with El Niño events. Similar to the Reanalysis, the peak in the noise forcing occurs before the maximum of the El Niño event and flips sign at approximately the same time as the maximum El Niño anomaly. While this has been shown to be an important part of the combination tone signal (Stuecker et al., 2013), it is also an important part of the stochastic noise forcing of ENSO (Levine and Jin, 2010). These properties suggest that, like the conceptual model, the noise forcing is important to the creation of an El Niño event, but not the only determining factor. The relationship between these two time series is reminiscent of the features captured in Figure 2.2 (c).

The previously defined method from the conceptual model can be applied to the noise estimated from the Reanalysis (Figure 3.9a). In examining the standard deviation of the noise time series as a function of T, it can be seen that it has a positive slope for the positive T anomalies and a fairly flat slope for negative T anomalies, although the relationship is noisy because the 50-year data length is still short. Additionally, the value of the standard deviation does not approach zero at $BT = -1$. Both of these features are similar to the threshold non-linearity case as shown in Figure 2.2 (c). It is determined that the SST-dependent factor of multiplicative noise, $B = 0.29 \pm .14$. The measured value is significantly different from $B = 0$, which has an uncertainty range of ± 0.11 for a 50 year estimate.

There is some concern that the decadal scale changes that have been observed over the period of the Reanalysis are large enough that they impact the noise forcing and the calculation of the B. Over time periods shorter than the 50 years, utilized for the estimation of B in Reanalysis, the estimate has large values of uncertainty and is

not shown. However, an examination of the standard deviation of the noise forcing as a function of the ENSO state for different twenty year periods within the 50 years of Reanalysis data, clearly shows that the increase in standard deviation of the noise forcing as a function of the ENSO state is not due to the changes in the mean state caused by decadal variability (Figure 3.10).

In both models, over the analyzed section of the simulation, the standard deviation as a function of temperature is unchanging for $T < 0$ and increases linearly with temperature for $T > 0$ (Figure 3.9 b and c). This is clear evidence of multiplicative noise forcing with a threshold non-linearity. In both models, the slope of the increase of standard deviation is greater than in Reanalysis. This is confirmed by the estimated value for the SST-dependent factor of multiplicative noise in CCSM4, $B = 0.89$, and in GFDL CM2.1, $B = 0.54$. The B value has a much smaller uncertainty because the data length is 400 years and 300 years respectively. This is consistent with the small scatter around the line in these figures. According to the theoretical results of Jin et al. (2007) and Levine and Jin (2010), the overestimation of the value of B should result in both models having overly active ENSOs. Indeed, both models have overly strong ENSOs, with standard deviations in the Niño indices used for these calculations of $\sigma = 1°C$ and $\sigma = 0.95°C$, respectively. This is compared with the Reanalysis which is $\sigma = 0.81°C$. This suggests that the correct simulation of the SST state dependent factor of multiplicative noise may play a role in correctly simulating ENSO amplitude.

Further utilization of the conceptual model results can be achieved by assuming that $R_\tau = \xi(1 + BH(T)T)$. The additive noise component, ξ, and the multiplicative noise component, $\xi BH(T)T$, can be isolated.

$$\xi = R_\tau/(1 + BH(T)T) \tag{3.1}$$

This isolation works because $1 + BH(T)T$ is positive definite. These two compoents can be mapped out to see where they have strong variability, like the total windstress was examined in Figure 3.8. In Figure 3.11, the additive component is examined. The pattern of the additive noise resembles the total noise forcing. This is because the additive noise

is responsible for the majority of the total noise forcing. The multiplicative noise forcing shows much larger variability in the tropics, just off the equator and minimal variability in the extra-tropics (Figure 3.12). The significantly smaller values of the reanalysis are related to the much smaller value of B in the reanalysis compared with the two coupled models. The large variability just north or south of the equator is probably related to the location of the ITCZ during the ENSO growth phase. Dispite the off equatorial maximums, the equatorial box for calculating R_τ is retained because the windstress forcing should be within the equatorial wave guide so as to force the Kelvin waves that are a large part of ENSO growth.

Examining the autocorrelations of these two components of the noise forcing, it can be seen that ξ behaves like red-noise with a fast decorrelation time scale and $\xi BH(T)T$ adds a low frequency component to the noise forcing, which Levine and Jin (2010) showed was necessary for the triggering of El Niño events (Figure 3.13). From this, it is observed that multiplicative noise adds memory to the system. Previoius examinations of the lengthened atmospheric memory have been attributed to the ocean (e.g Frankignoul and Hasselmann (1977)). While multiplicative noise is a different process than simple red noise, it could be useful to explore the ocean as a source of increased memory.

3.6 Summary

The first challenge in applying the methodology developed in the conceptual model for calculating B is to define a noise time series. Unlike the conceptual model where the noise is externally generated and stored, in the Reanalysis and GCMs the total windstress is measured and the noise must be isolated. The linear ENSO, the threshold non-linear ENSO, the annual cycle combination tone, and the semi-annual combination tone signals are all removed from the anomalous windstress to extract the windstress noise time series. Using the conceptual model, it is shown that this method can successfully remove these signals linearly. This noise is shown to have properties consistent with multiplicative noise forcing. As extracted, the windstress noise is shown to have properties associated with white or red noise. Further, the state dependence factor can be measured over

these time series. In all cases, B is significantly different from zero. The estimate from Reanalysis is $B = 0.29$, from CM2.1 is $B = 0.54$, and from CCSM4 is $B = 0.89$. Both of the climate models investigated here have overly strong representations of multiplicative noise when compared with the Reanalysis, which corresponds with the models having the amplitude of ENSO be too large. However, having too strong of a representation of the multiplicative noise makes these models a good choice for a continuing study of the physical processes associated with multiplicative noise because the processes involved will most likely be more evident.

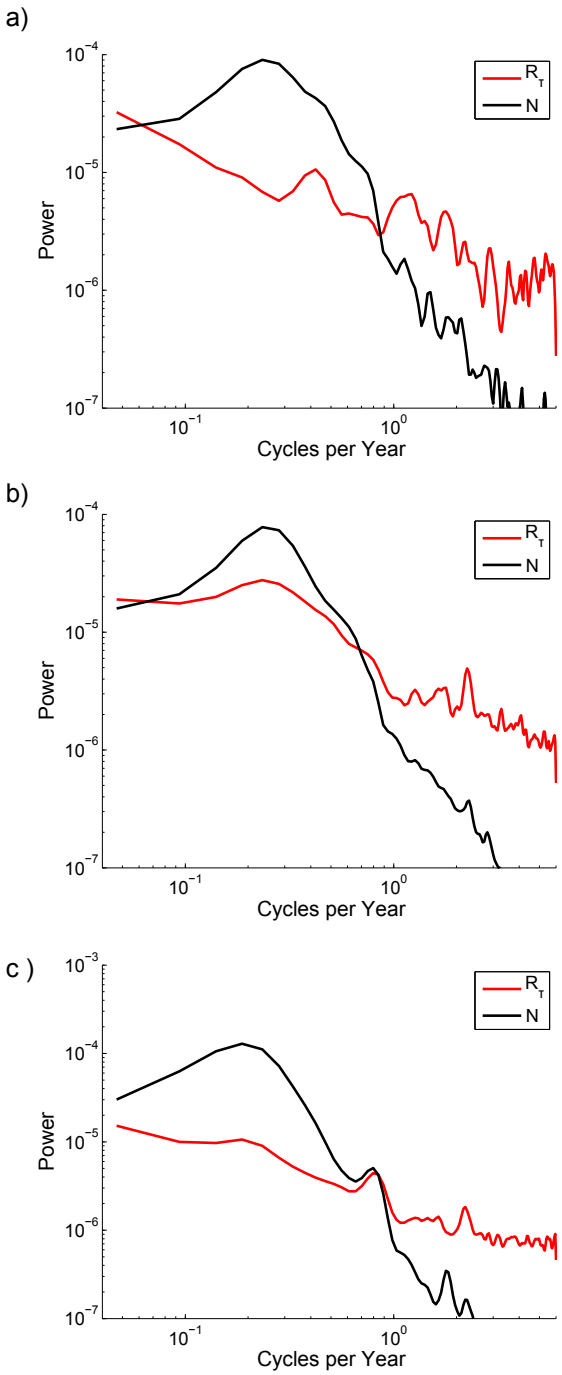

Figure 3.1: Spectra showing the ENSO and windstress noise forcing from a) Reanalysis b) CM2.1 c) CCSM4.

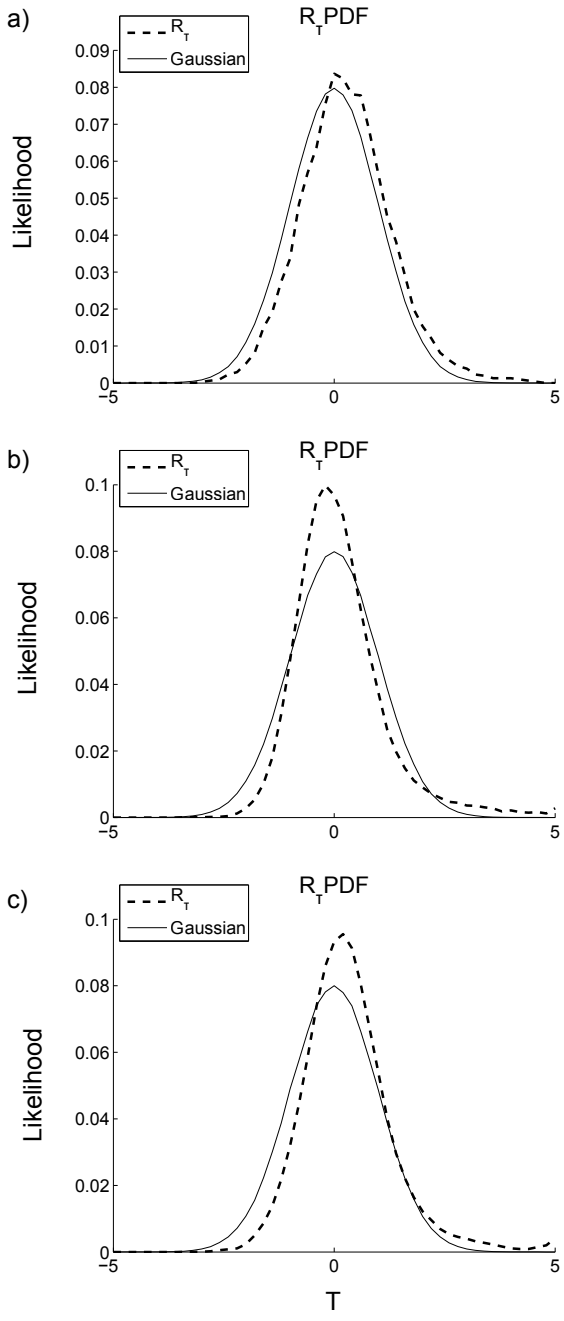

Figure 3.2: The normalized histogram of R_τ for a) Reanalysis b) CM2.1 c) CCSM4. It is nearly Gaussian in distribution. The normalized histograms are created by binning in bins of width 0.1 and then are smoothed over 5 points.

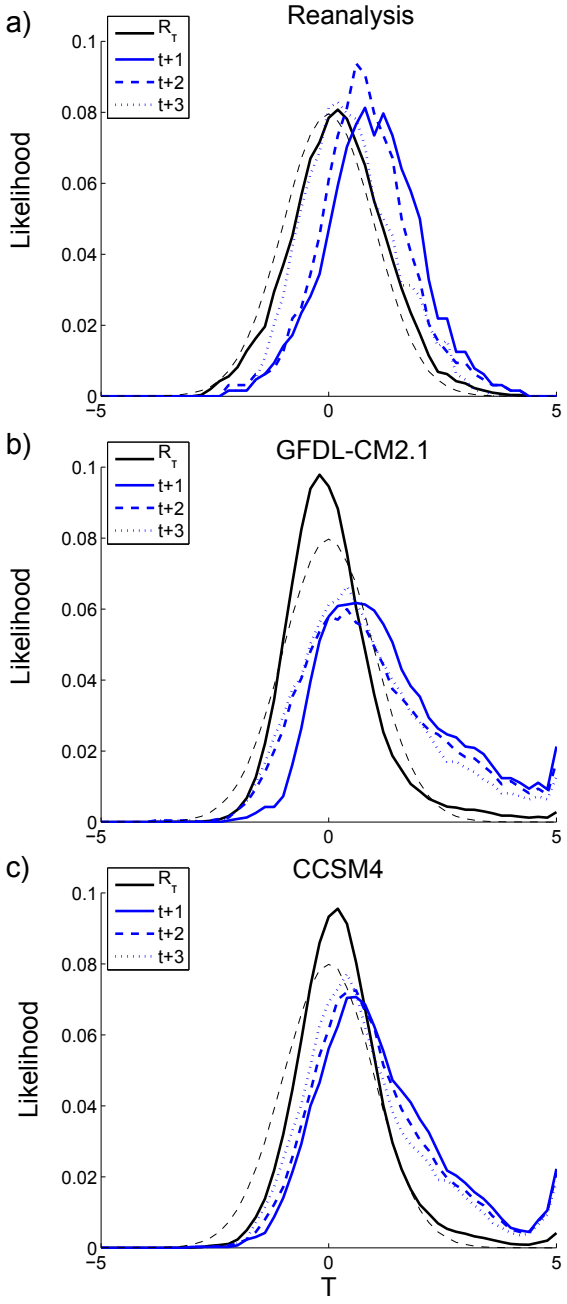

Figure 3.3: Normalized histograms of R_τ for one, two, and three months after a large ($R_\tau > \sigma(R_\tau)$) noise event for a) Reanalysis b) CM2.1 c) CCSM4. In all cases the positive tail is enhanced like the multiplicative noise case from the conceptual model. The normalized histograms are created by binning in bins of width 0.1 and then are smoothed over 5 points.

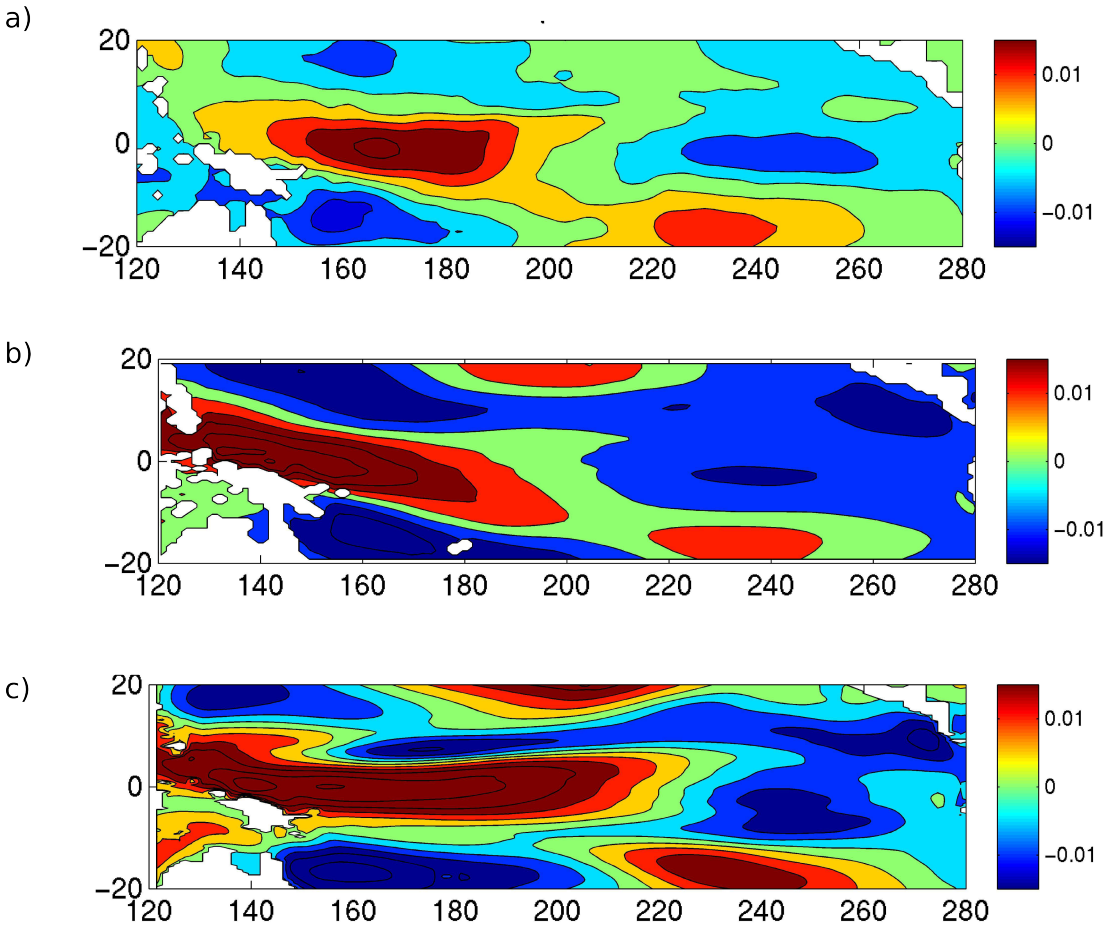

Figure 3.4: Spatial patterns of μ, the linear regression coefficient for the linear response of the windstress to ENSO for a) ERA40, b) GFDL CM2.1 and c) CCSM4. The strong westerly response in the western Pacific to El Niño events shifts the convection from the western Pacific to the central Pacific, which is evidence of the anomalous Walker circulation.

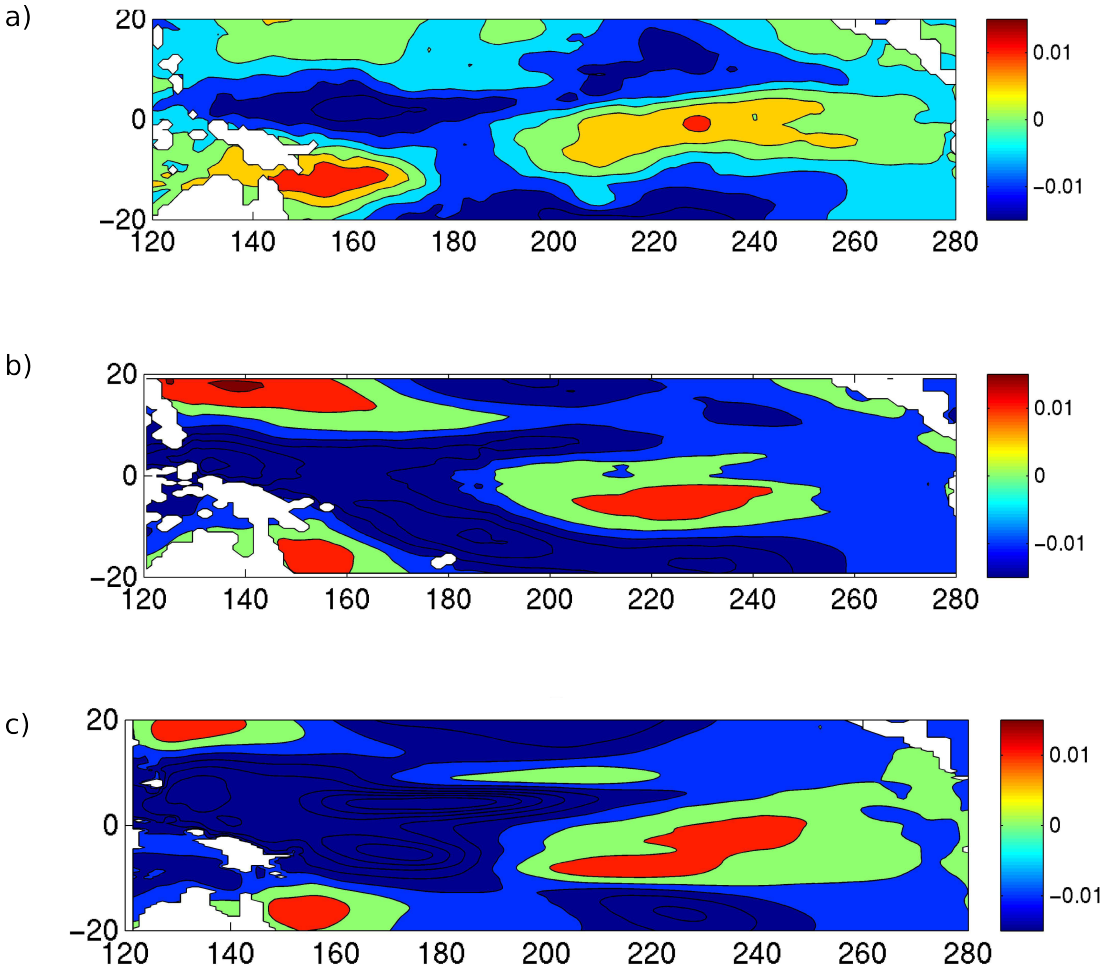

Figure 3.5: Spatial patterns of μ_2, the linear regression coefficient for the non-linear response of the windstress to ENSO for a) ERA40, b) GFDL CM2.1 and c) CCSM4. The non-linear response is an east-west dipole similar to the findings of Choi et al. (2013).

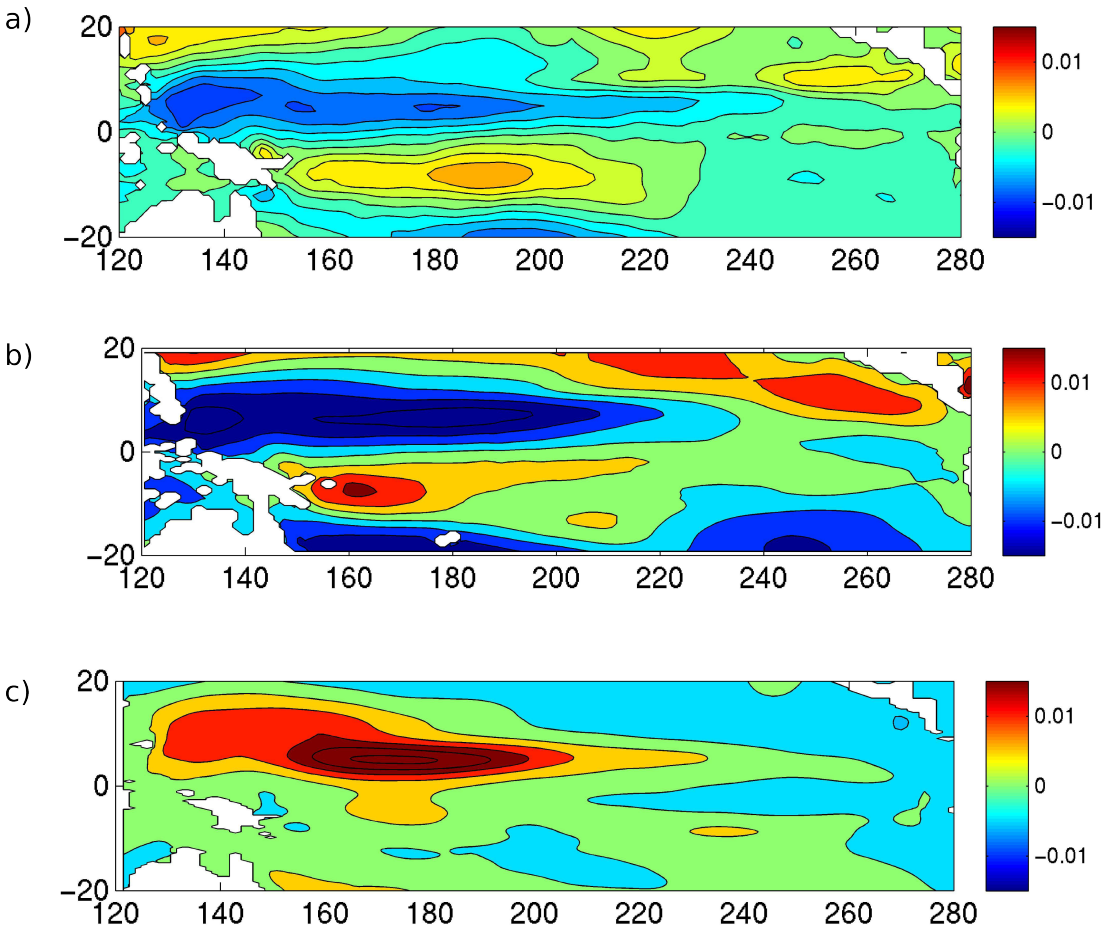

Figure 3.6: Spatial patterns of the linear regression for $\tau = \mu TH(T)cos(\omega_{AC}t - t_0)$ for a)ERA40, b) GFDL CM2.1 and c) CCSM4. The annual cycle combination tones for ERA-40 and GFDL CM2.1 are asymmetric and similar to the combination tones found by Stuecker et al. (2013). CCSM4 has a strong northern component of the combination tone, but lacks the asymmetric match in the southern hemisphere.

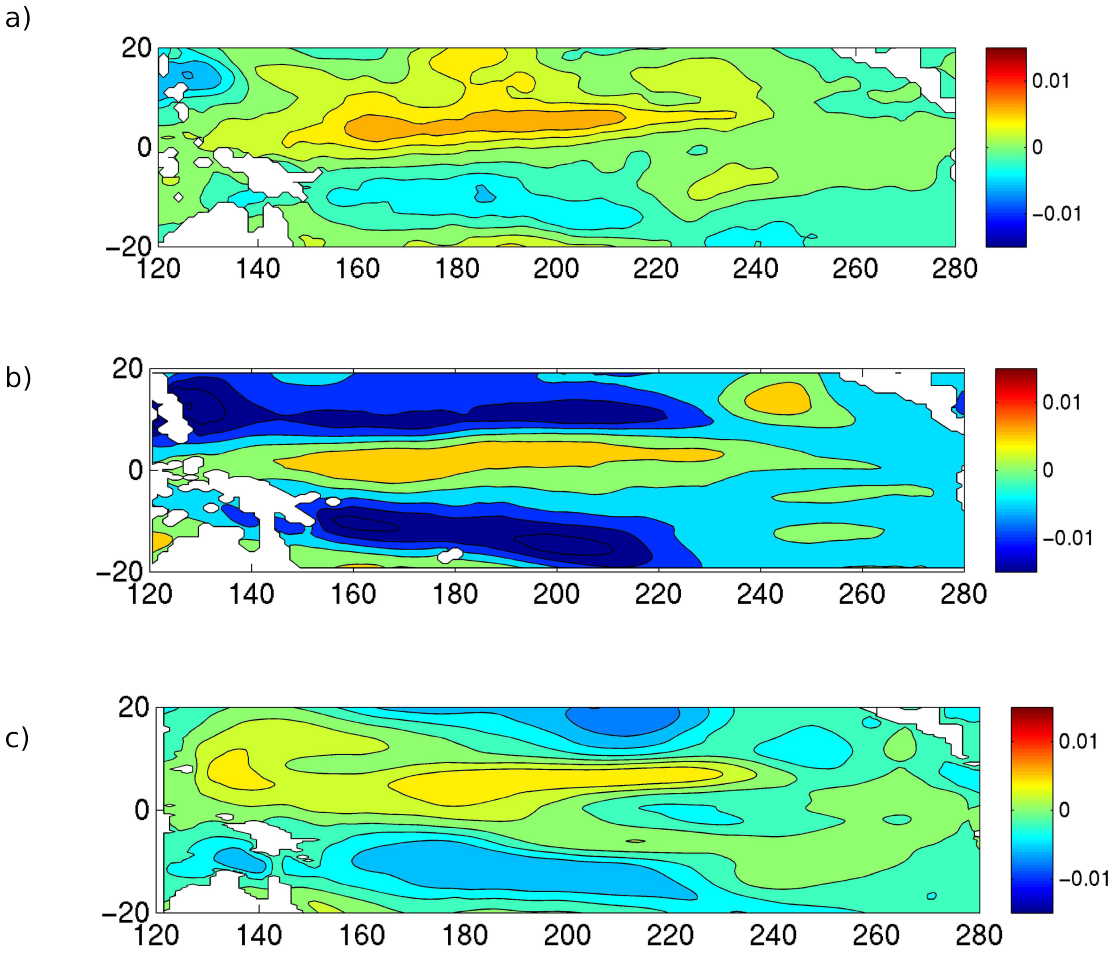

Figure 3.7: Spatial patterns of the linear regression for $\tau = \mu TH(T)cos(2\omega_{AC}t - t_0)$ for a) ERA40, b) GFDL CM2.1 and c) CCSM4. The semi-annual cycle combination tones are symmetric about the equator.

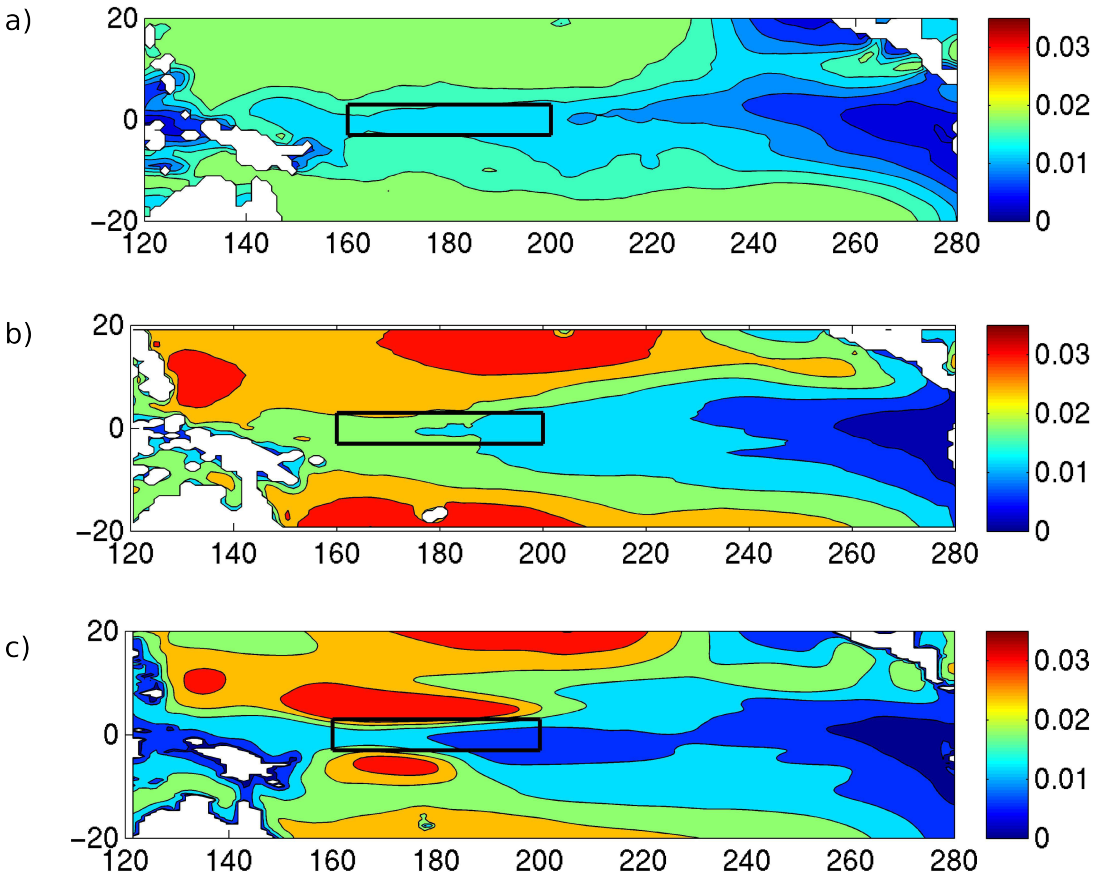

Figure 3.8: The standard deviation of R_τ as a function of latitude and longitude for a) ERA-40 b) CM2.1 c) CCSM4. The box outlines the area averaged in the time series, R_τ. It corresponds with the large area of higher variability in the windstress forcing.

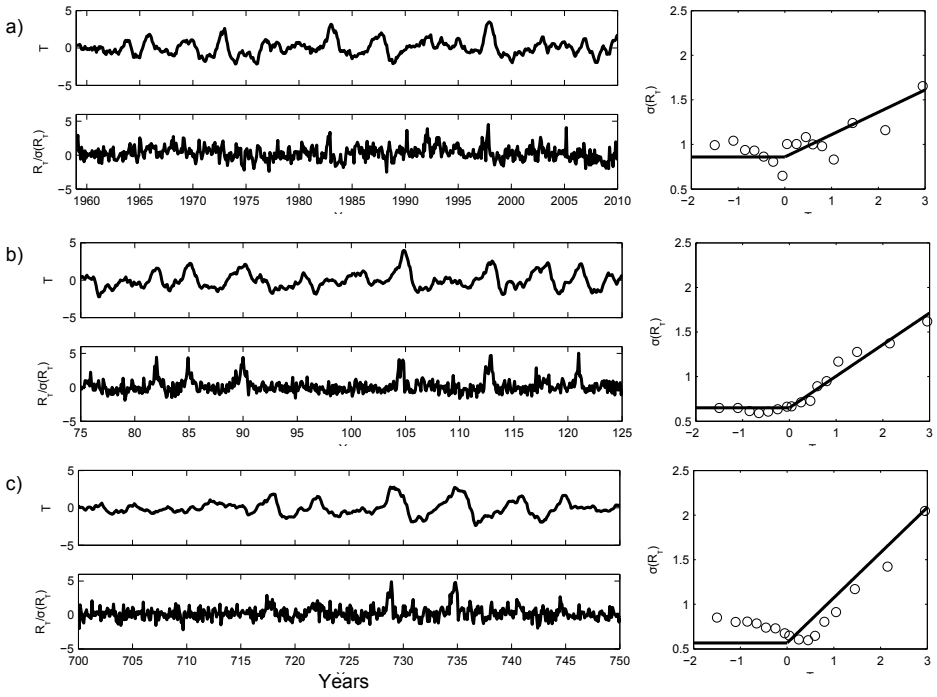

Figure 3.9: time series of SSTA (upper left) and central Pacific zonal windstress noise forcing (lower left) and conditional standard deviation of R_τ as a function of T (right) for a) Reanalysis b) CM2.1 c) CCSM4. The values of B estimated are 0.29, 0.54, and 0.82 respectively.

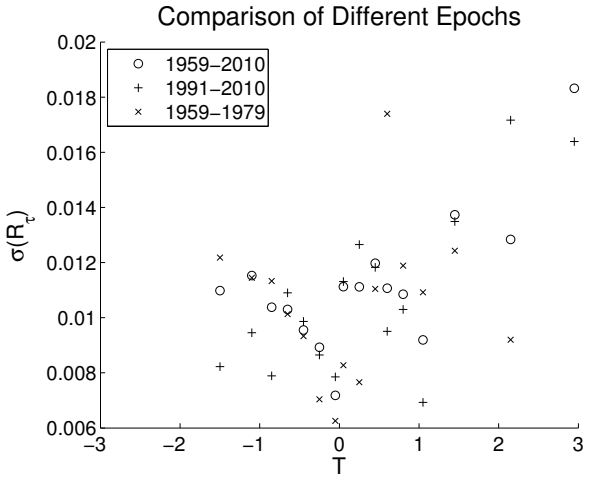

Figure 3.10: Comparison of two different periods (1959-1979 and 1991-2010) with the full 51-year Reanalysis conditional standard deviations. Because of the reduced period, the threshold of 15 points per bin is not used to create this plot. The two different periods both show overall changes in standard deviation as a function of T and within the error for such a short period of evaluation suggest that the longer decadal scale changes in the tropical Pacific mean state are not responsible for the multiplicative noise variability.

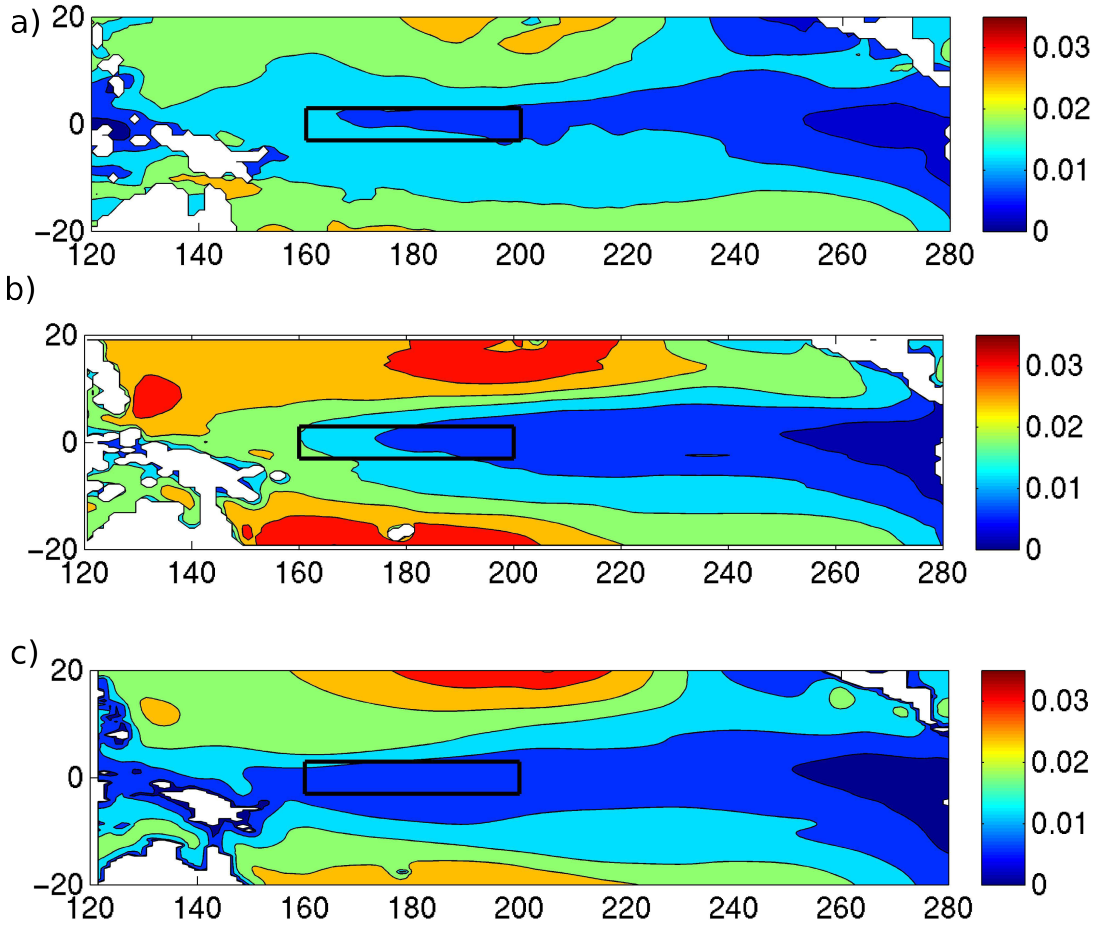

Figure 3.11: The standard deviation of the additive component of the windstress noise, ξ, as a function of latitude and longitude for a) ERA-40 b) CM2.1 c) CCSM4. The box outlines the area averaged in the time series, R_τ. The additive component has a stronger signal in the extratropics than in the tropics much like the total windstress noise (as seen in Figure 3.8).

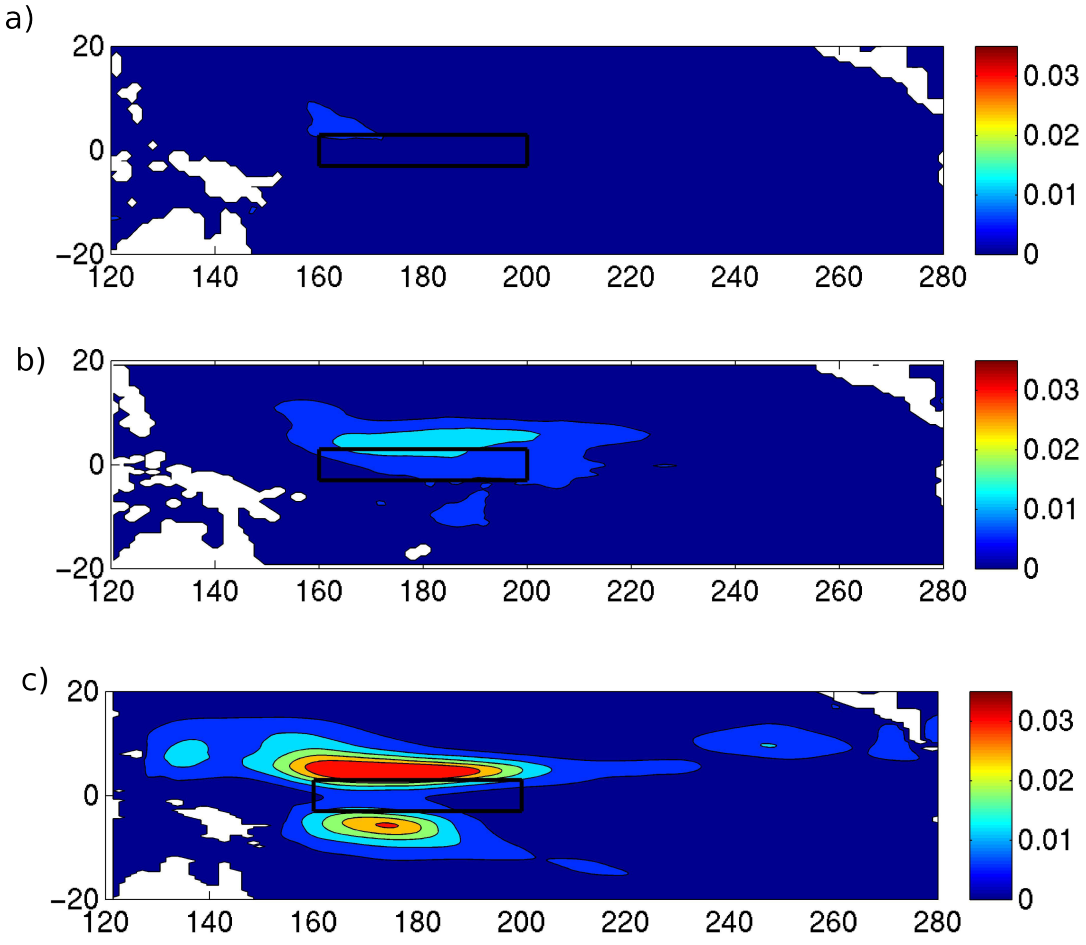

Figure 3.12: The standard deviation of the multiplicative component of the windstress noise, $BH(N)N\xi$, as a function of latitude and longitude for a) ERA-40 b) CM2.1 c) CCSM4. The box outlines the area averaged in the time series, R_τ. It corresponds with the large area of higher variability in the windstress forcing. These values are more tropically focused, although off-equator, than the total noise forcing (as seen in Figure 3.8) or additive noise forcing (Figure 3.11).

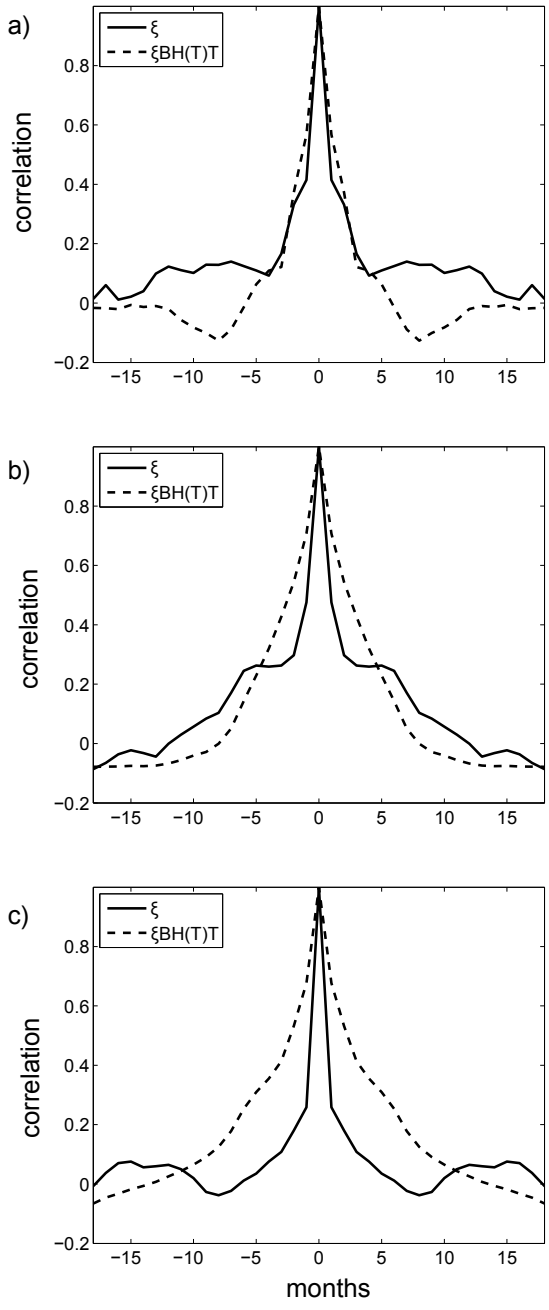

Figure 3.13: Autocorrelation of ξ, the additive component, and $BH(N)N\xi$, the multiplicative component for a) Reanalysis b) CM2.1 c) CCSM4. The multiplicative component increases the e-folding time of the system.

Chapter 4

The Physical Processes of Multiplicative Noise

4.1 Introduction

Having established that there is multiplicative noise in the windstress forcing of ENSO, this chapter will examine the physical processes that create the multiplicative noise, how multiplicative noise fits within the context of previous studies of noise forcing of ENSO, and its role in the triggering and growth phases of El Niño events. First the spatial and temporal characteristics associated with multiplicative noise forcing and its association with the low frequency component of the noise forcing of ENSO will be examined. Next, the respective roles of ocean and atmosphere will be explored. Finally, a number of experiments have been conducted to examine the role of coupling the ocean and atmosphere for the generation of multiplicative noise.

4.2 Spatial and Temporal Evolution of Multiplicative Noise

In Chapter 2, a method was derived to isolate the windstress noise from the total windstress averaged over 160°E-160°W and 3°S-3°N.

$$\tau_x = \mu T + \mu_2 H(T) T + \mu_{AC} H(T) T cos(\omega_{AC}(t - t_0)) + \mu_{SAC} H(T) T cos(\omega_{SAC}(t - t_0)) + R_\tau \tag{4.1}$$

This approach can be expanded spatially such that R_τ is calculated at each grid point. When averaged over the same region as the index in chapter 3, the spatial residual, $R_\tau(x, y, t)$, returns the same time series used previously. The spatial expansion allows for further investigation of the evolution of the low frequency component of the noise both spatially and temporally, which will further allow for better comparisons with previous studies on WWBs. To examine the large and extreme cases of low frequency noise forcing, $R_\tau(x, y, t)$ is composited when $R_\tau > \sigma(R_\tau)$ and $R_\tau > 3\sigma(R_\tau)$ over 160°E-160°W and 3°S-3°N for large and extreme low frequency noise events, respectively. The reanalysis contains 128 large events and 5 extreme events. CM2.1 contains 470 large and 79 extreme events, and CCSM4 contains 827 large and 116 extreme events. Compositing the events is chosen over other methods of aggregation due to the non-linear response of the noise forcing to ENSO state as demonstrated previously. Spatially, the patterns of the large noise events and the extreme noise events do not look very different. They all consist of strong westerly wind forcing in the equatorial wave guide over the western Pacific warm pool. They differ from the stochastic optimals found by Moore and Kleeman (1999) by being narrower and not symmetric about the equator (Figure 4.1). These differences could be caused by model differences, Moore and Kleeman (1999) used much simpler model, or also by annual cycle interactions, which could limit the strongest westerly events to specific times of year when the ITCZ is displaced from the equator. However, in all cases the extreme low frequency noise events extend further east than their large low frequency noise event counterparts. Both the reanalysis and CM2.1 show the wind burst centered on and fairly symmetric about the equator. CCSM4 has its strongest signal north of the equator with a smaller maximum south of the equator, creating a

strong signal through the equatorial wave guide.

However, the time evolution associated with the differences in amplitude are important. The large low frequency noise events show a westerly wind forcing that is concentrated mainly during the month of the peak event with reduced signals in the months before and after the burst. It is a short duration event that quickly decays. In these cases the westerly winds are also confined to a more narrow region along the warm pool edge. However, in the case of the extreme noise events, the wind burst is not confined spatially or temporally. The extreme events show a build up in intensity in the months leading up to the peak of the wind forcing (a low frequency component of the noise forcing) with an eastward progression of the strongest anomalies moving from the warm pool edge expanding eastward (Figure 4.2). The extreme events begin a couple of months earlier with an event of similar magnitude and spatial scale as observed with the large events. While the increase in amplitude and the eastward propagation are less clear in the reanalysis than in the models, this is consistent with a smaller value of B for the reanalysis than for either of the models. The smaller value of B implies that the background ENSO state is less important in forcing the extreme events in reanalysis than in the analyzed models, which should give a more independent event-like structure to the extreme events in the reanalysis.

These differences are even more apparent when examining the multiplicative component of the noise forcing. To do this, the shape of the multiplicative noise function is assumed to be $[1 + BH(T)T]\xi$ and set $R_\tau = [1 + BH(T)T]\xi$. Using $B = 0.29$, $B = 0.54$, and $B = 0.89$ for the reanalysis, CM2.1, and CCSM4 respectively, the "additive" noise, ξ, and "multiplicative" noise, $BH(T)T\xi$ components are then roughly isolated by solving for ξ.

$$\xi = \frac{R_\tau}{(1 + BH(T)T)} \tag{4.2}$$

The results of this separation on the estimation of ξ were shown in Figure 2.10b, which shows that using this simple separation does a good job of estimating the correct values of ξ. The relative values of R_τ, ξ, and $BH(T)T\xi$ are shown in Figure 4.3. Here we see that the additive noise accounts for the bulk of the variability and that this variability

is fairly constant over time with the multiplicative noise component adding significant noise forcing in short event like bursts. These events usually occur a couple of months before the peak of an El Niño event (Figure 4.4). This difference in the low-frequency component is a key characteristic of multiplicative noise.

Using the additive and multiplicative noise time series, the analysis done in Figures 4.1 and 4.2 is redone to examine the differences between multiplicative and additive noise. In these cases, composites are created for $\xi > \sigma(R_\tau)$ for the additive cases, and $BH(T)T\xi > \sigma(R_\tau)$ for the multiplicative cases. The reanalysis contains 115 large additive events and 2 large multiplicative events, CM2.1 contains 336 large additive and 102 large multiplicative events, and CCSM4 contains 396 large additive and 302 large multiplicative events. Here we see that the multiplicative noise composites are just exciting the stochastic optimal with higher amplitude forcing than the additive noise cases (Figure 4.5). The multiplicative noise event composites are very similar to the extreme low frequency noise event composites in Figure 4.1 for all cases The additive noise cases are similar to the large low frequency noise events. The multiplicative case of the reanalysis shows even greater eastward extent of the westerly winds than the extreme low frequency case, but this maybe a result of too few events to composite and, hence, over emphasizing the 1997-8 El Niño. Combining these spatial similarities with the differences in number of events suggests that multiplicative noise is responsible for increasing the likelihood of the occurrence of extreme westerly wind events, which can be found in the partial distribution functions of R_τ in Figure 3.4.

While spatially somewhat similar in shape, the temporal differences between the additive and multiplicative noise cases show a very clear distinction (Figure 4.6). The multiplicative noise forcing shows a clear build-up in amplitude over the months preceding the event with additional forcing after the composited time and an eastward propagation of the noise forcing from the Warm Pool edge across the dateline and potentially into the eastern Pacific. The additive noise forcing shows a much more isolated event-like structure without prior events or eastward progression, much like the spatial composites. The Hovmoeller diagrams of the multiplicative noise case are similar to the extreme low frequency noise case and the additive noise case Hovmoeller diagrams are similar to the

large low frequency noise events (Figure 4.6). The multiplicative noise composite shows even more clearly the increasing strength of the westerly wind and the overall eastward propagation of the forcing than was seen in the extreme low frequency noise case. The reanalysis results further show propagation of the westerly winds further to east beyond the area averaged box in the months after the composited event. This build-up of the forcing and its eastward progression is consistent with previous studies on multiplicative noise (Gebbie and Tziperman, 2009a) and with observations of the windstress leading up to the 1997-8 El Niño event (McPhaden, 1999).

4.3 Coupled Processes of Multiplicative Noise

4.3.1 Warm Pool Advection

Lengaigne et al. (2004), Lopez et al. (2013) and Lopez and Kirtman (2013) found that idealized state dependent noise forcing created an anomalous temperature response on the warm pool edge. Observational studies from the TOGA-COARE project (Webster and Lukas, 1992) also found anomalous warm temperatures and zonal heat transport after the passage of a westerly wind burst in the central Pacific (McPhaden et al., 1988). These warm anomalies are driven by the wind bursts and represent a possible mechanism for multiplicative noise forcing. To determine the non-ENSO component of the zonal advection of the warm pool, a similar assumption to Jin et al. (2006) is made here where $< u >_E = \beta_u[\tau_x] + \beta_{uh} < h >_w$ and β_u and β_{uh} are the linear regressions of the zonal current anomaly on the windstress and the western Pacific thermocline depth, respectively (Jin et al., 2006; Kim and Jin, 2011a,b). Since the comparison is between the zonal current anomaly and the windstress anomaly, $\beta_u[\tau_x]$ is replaced with $\beta_{uT}T$, which takes advantage of the fact that windstress is also linearly related to ENSO state to eliminate the zonal current response to ENSO state irrespective of windstress. Then, a similar isolation method on the zonal current is used as previously used for the windstress, eliminating the zonal current signals due to ENSO non-linearity and interactions with annual cycle combination tones, where the area-averaged zonal current, $< U >$, can be

decomposed into the deterministic part, U_D, and a residual, R_U.

$$< U >= U_D + R_U \tag{4.3}$$

Since upper ocean heat transport is important for the spreading of the warm pool, the zonal advection of temperature by the anomalous zonal current $ZA = -R_u \frac{\partial T}{\partial z}$ averaged over the upper 50m of the ocean is examined. By compositing on the additive and multiplicative noise events, the difference in zonal advection of temperature can be compared. The additive case shows a weaker zonal advection of the warm pool SSTs eastward in the wake of the wind burst. This has been observed following westerly wind bursts before (McPhaden et al., 1988). The difference in the multiplicative noise case is that the zonal advection of SST begins before the strongest wind stress event, progressing eastward and increasing in magnitude before the peak of the wind stress (Figure 4.7). This is similar to the difference between the large additive and multiplicative events in the wind stress and corresponds to an eastward advection of the warm pool edge. This agrees with what has been shown by Gebbie and Tziperman (2009b) and Lopez et al. (2013). Additionally, in both the models and the reanalysis, there is a continuation and eastward propagation of the anomalous zonal temperature advection after the peak of the multiplicative noise windstress event which is not apparent after additive noise cases. Similar to what was observed in the reanalysis windstress the zonal advection of the temperature continues to push further east after the peak of the multiplicative noise in comparison to the models.

The eastward expansion of the Warm Pool happens during both large additive and multiplicative westerly wind events (Figure 4.7). The difference between the large additive events and the large multiplicative events is that the large multiplicative events happen when additional westerly wind bursts occur shortly after the initial eastward warm pool excursion, reinforcing the initial excursion and pushing the westerly wind bursts further east through the central Pacific due to an increased availability of warm SSTs. This further reinforces the incipient El Niño event, creating a low frequency component of the noise forcing.

4.3.2 Precipitation Response

As shown previously, the multiplicative noise exhibits a distinct threshold non-linearity component. The leading mechanism to explain this non-linearity, due to the underlying mean SSTs, would be convection. Examining the 1982-3 and 1997-8 El Niño events, the eastward propagation of this anomalous convection is evident based on observed monthly mean outgoing longwave radiation (Figure 4.8a). As the warmer water advects east along the warm pool edge, the atmosphere responds to these changes in boundary forcing with changes in local convergence where the westerly anomalies combine with the climatological easterlies to produce a region of zero net wind. The precipitation anomalies are located in this region of zero net wind. In the multiplicative noise case, the anomalous precipitation progresses eastward in conjunction with the anomalous zonal temperature advection and the anomalous westerly wind stress. This does not occur in the additive cases (Figure 4.8b), stressing the importance of the eastward migration of the forcing as an important characteristic of the multiplicative noise forcing. CCSM4 shows a significant increase in precipitation in the multiplicative noise composite over the entire eastern Pacific (Figure 4.8c). In all cases, there is enhanced drying occuring over the warm pool region. This is consistent with the observations and model experiments that have suggested that the largest El Niño events are forced by a series of westerly wind events that move further and further to the east over the course of the growth phase of El Niño (McPhaden, 1999; Gebbie and Tziperman, 2009b).

4.3.3 Coupled Ocean-Atmosphere Experiments

The precipitation response, which drives the eastward propagation of the wind bursts, is driven by changes in the eastern edge of the western Pacific warm pool. However, beyond just propagating eastward, the wind response amplifies as the incipient El Niño intensifies. To determine whether the atmosphere itself was the cause of the amplification, an experiment was conducted with GFDL AM2.1 (The GFDL Global Atmospheric Model Development Team, 2004). Three cases of boundary forcing were examined. The reanalysis SST case (HadSST) was run with HadISST SSTs forcing the atmosphere. In

this case, 10 ensemble members of 50-years each were examined. The second case, CM-SST, used the previously analyzed 300-year SSTs from CM2.1 as forcing. In this case, a single 300-year realization was examined. The final case, CM-anom, used the HadISST monthly mean SSTs plus the CM2.1 monthy SST anomalies. This experiment also used a single 300-year realization. The SSTs are prescribed over a region of 20° N-20° S and 100° E-80° W and use climatological SSTs elsewhere. The horizontal resolution of AM2.1 is approximately 2.5 degree longitude by 2 degree latitude and uses 24 vertical levels.

The mean standard deviation of R_τ with respect to T of each case is shown with the ensemble standard deviation for the HadSST experiment in Figure 4.9. The value of B from the experimental cases show a significant decrease in B from the the value found previously in the analyzed 300-year integration of CM2.1. These differences in B indicate the role of the coupled system for windstress multiplicative noise forcing. The windstress response triggers an ocean response, which can then enhance the windstress response of any additional noise event that occurs. When these two components, the windstress and warm pool advection, of the system are not allowed to communicate, as is the case without coupling, the windstress memory of previous westerly wind bursts that would normally be maintained in the multiplicative noise is lost.

This can be seen more clearly in the spectra of the windstress noise forcing in the experiments compared with the fullly-coupled run (Figure 4.10). In the coupled case, the noise forcing has stronger low frequency noise forcing. However, both the CM-SST and CM-anom experiments show additional spectral peaks. Both have peaks at frequencies much lower than the ENSO peak. Outside of this low-frequency peak, the CM-SST experiment shows less energy at all other frequencies than the coupled case. It shows a larger deficit in energy in the low frequencies compared with the coupled case than in the high frequency component. The CM-anom experiment has less energy from the low frequency peak until periods of approximately 1 year. There is additional energy in the periods between 6 and 12 months. However, as has been shown by Levine and Jin (2010), high frequency energy is unable to force ENSO, so this extra energy is unimportant. In the HadSST case, the noise forcing is white instead of red. From this it can be seen

that the role of the coupling is to increase the total memory of the system, which is an importantant component of the multiplicative noise forcing of ENSO.

Comparing the composite for the multiplicative noise between the coupled simulation and CM-SST, the role of the ocean-atmosphere coupling is clearly evident. In the CM-SST experiment, the extreme westerly wind events do not show the same eastward propagation (Figure 4.11) or the increase in magnitude of the westerly wind forcing over the previous months. This was previously identified as important component of the multiplicative noise. Instead the CM-SST experiment retains the more solitary, event-like structure of the additive forcing, only at a larger magnitude (Figure 4.11). Coupling enhances the multiplicative noise and provides the impetus for the combined eastward migration of the westerly wind events and of the warm pool edge.

In the CM-SST simulation, the Warm Pool edge propagates eastward with or without the previous westerly wind forcing. Since the precipitation changes are a response to the location of the warm pool edge, the precipitation in the CM-SST simulation shows an eastward propagation (Figure 4.12) unlike the westerly wind response. However, the difference in the precipitation response between the large and extreme westerly wind events is merely one of magnitude and not one of kind as observed for the coupled case. The increase precipitation in CM-anom over the CM-SST experiment is related to the changes in climatological SST from the removal of the Cold Tongue bias.

As the Warm Pool edge moves further east, convection spreads to the east and the westerly wind events push further to the east. This, in turn, expands the warm pool even more and provides a positive feedback within the noise forcing of ENSO and can lead to even larger El Niño events. This is consistent with the prediction of an increased number of large El Niño events with greater multiplicative noise forcing from Levine and Jin (2010). The implication of all of these results combined is that the magnitude of the multiplicative noise is set by two things, the eastward migration of the Warm Pool edge in response to a westerly wind burst and the ability for convection to form further to east in response to the expanded Warm Pool. Additionally, the shape of the multiplicative noise (threshold nonlinearity) is set by atmospheric convection.

4.4 Summary

The extreme low frequency noise events of El Niño have a similar spatial pattern to other westerly wind bursts. These spatial patterns differ from the stochastic optimals of Moore and Kleeman (2001) in width and symmetry about the equator. These differences are most likely due to differences in model and the seasonality of WWBs. The major difference between the large low frequency noise forcing events and the extreme ones are the the extreme low frequency noise forcing events are not isolated in time. These extreme events have preceding large noise events which prime the ocean, by forcing zonal advection of the western Pacific Warm Pool, for the creation of the extreme events. This is in agreement with Gebbie and Tziperman (2009b). This priming of the ocean can be demonstrated by multiplicative noise. The total noise forcing can be split into additive and multiplicative components. The multiplicative noise component is responsible for the additional magnitude of the extreme low frequency noise forcing events.

Organized anomalous precipitation in the region occurs contemporaneously with the eastward march of the westerly wind anomalies and the eastward progression of the Warm Pool edge. The anomalous precipitation connects the oceanic response to the westerly wind anomalies and the future westerly wind anomalies that are the critical atmospheric manifestation of multiplicative noise. A westerly wind event creates positive zonal temperature advection, expanding the western Pacific Warm Pool. The expanded Warm Pool supports additional convection further to the east. The difference in eastward extent of the additional westerly wind forcing between the reanalysis and the models could therefore be explained by the existence of the coupled model Cold Tongue bias preventing convection from forming further to the east. Continuing the cycle, if the convection forms further to the east, additional westerly wind anomalies occur due to convergence. These new westerly wind anomalies expand the Warm Pool further to east, allowing for more eastward propagation of the convection (Figure 4.11). This is in agreement with previous studies on multiplicative noise (Lengaigne et al., 2004; Eisenman et al., 2005; Gebbie and Tziperman, 2009b). The positive feedback loop is then broken by the delayed response of the thermocline and the limited resource of ocean heat content

which eventually outcrops cooler waters at the outset of La Niña as well as interactions with the annual cycle.

By examining the uncoupled model experiments compared to the coupled model, it can be seen that the value of B is reduced by 50% without coupling. As has been shown, the multiplicative noise acts to increase the memory of the system by 2-3 months (Figure 3.13) and the low-frequency component of the noise which has been shown to be important for noise forcing of ENSO. The uncoupled experiments have a more event-like structure to the most extreme WWBs (Figure 4.11). The more event-like structure displays the fact that the low-frequency component of the noise is reduced without coupling. This reduction can also be seen in the power spectra of the uncoupled experiments versus the coupled simulation. This is consistent with a reduction of the measured value of B that is seen by applying the methodology previously developed to the uncoupled experiments.

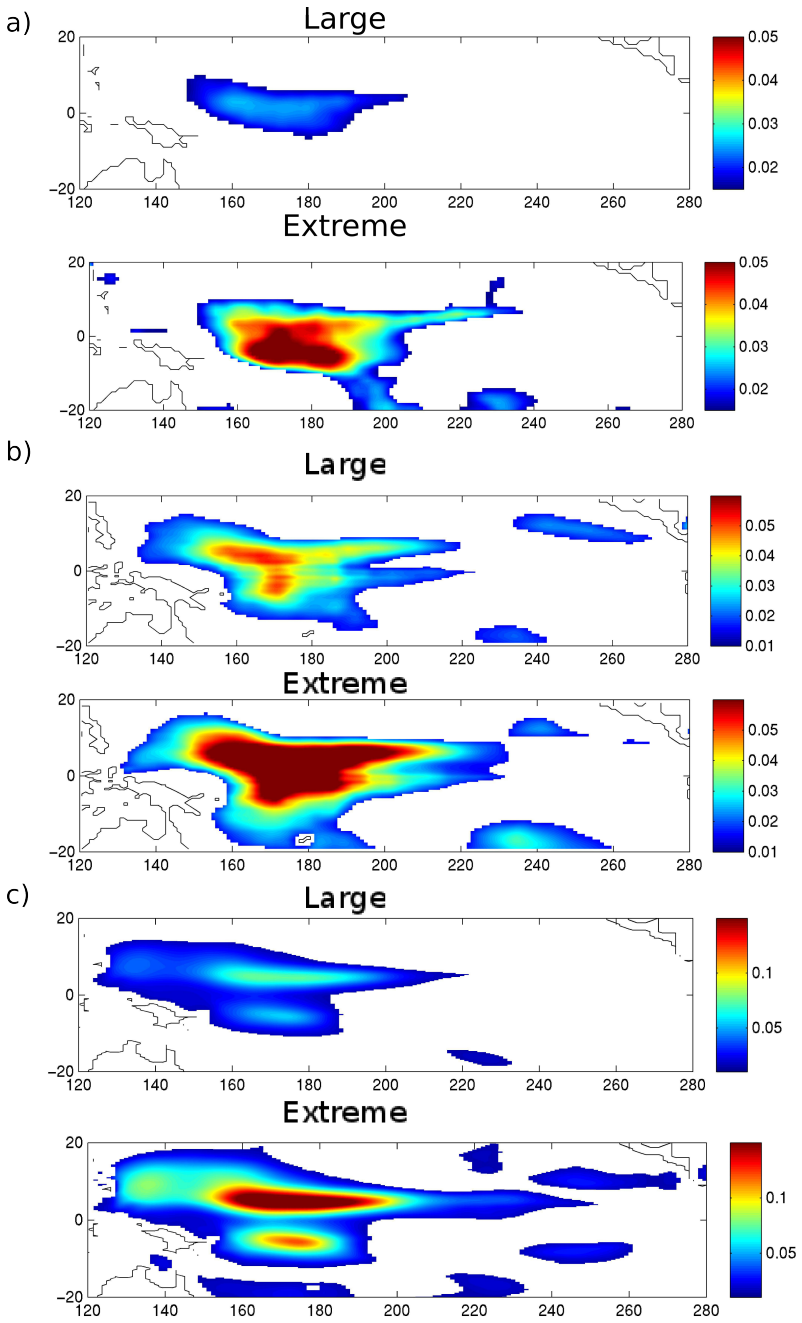

Figure 4.1: Spatial distribution of large ($R_\tau > \sigma R_\tau$) and extreme ($R_\tau > 3\sigma R_\tau$) westerly wind ($\frac{N}{m^2}$) events for a) ERA-40, b) GFDL CM2.1 c) CCSM4.

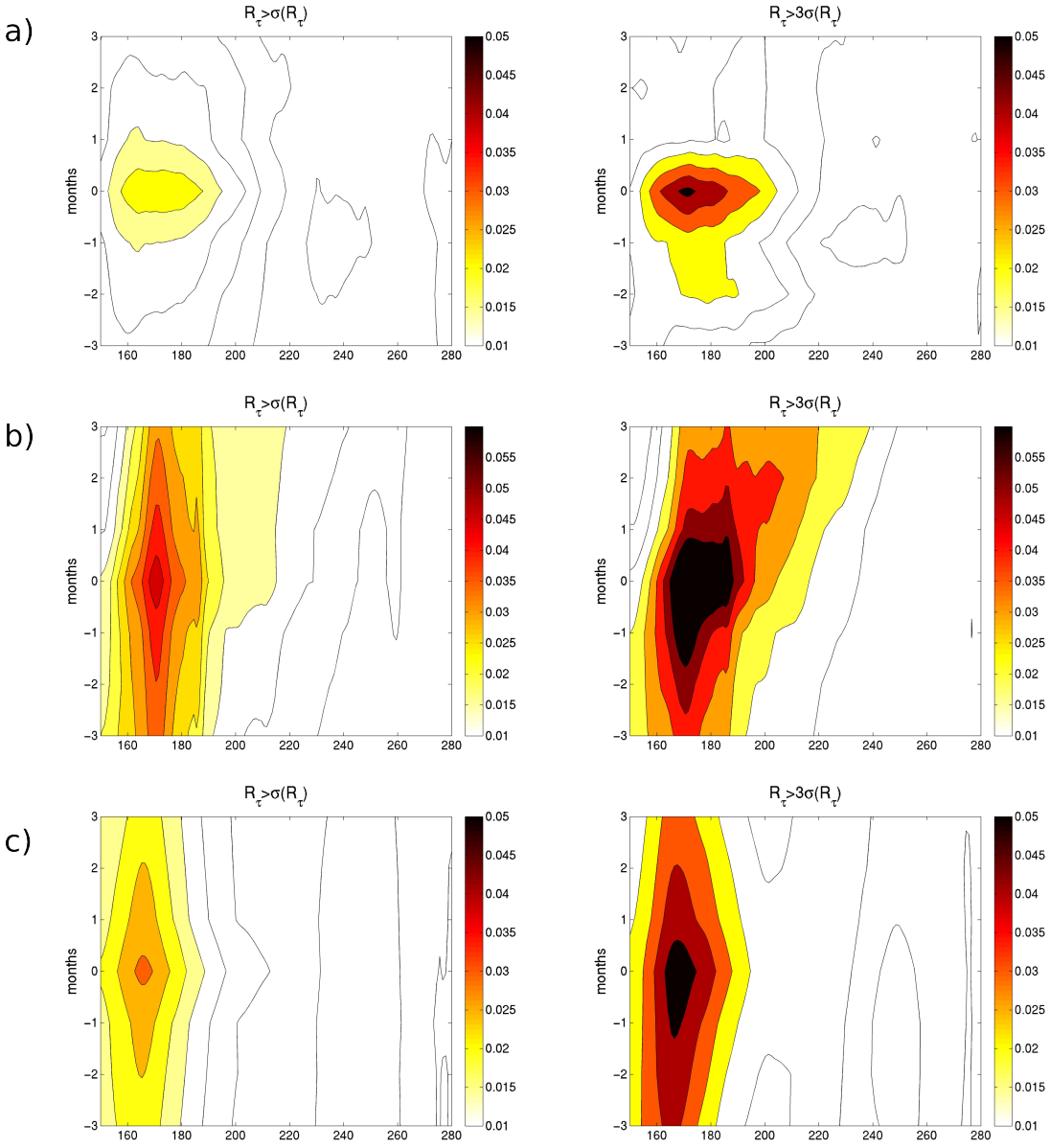

Figure 4.2: Hovmoeller diagrams of the anomalous westerly wind forcing ($\frac{N}{m^2}$) averaged over 5° S - 5° N preceding and following large (left) and extreme (right) westerly wind events for a) ERA-40, b) GFDL CM2.1 c) CCSM4. The large events are isolated while the extreme events have a longer lasting low frequency component to them.

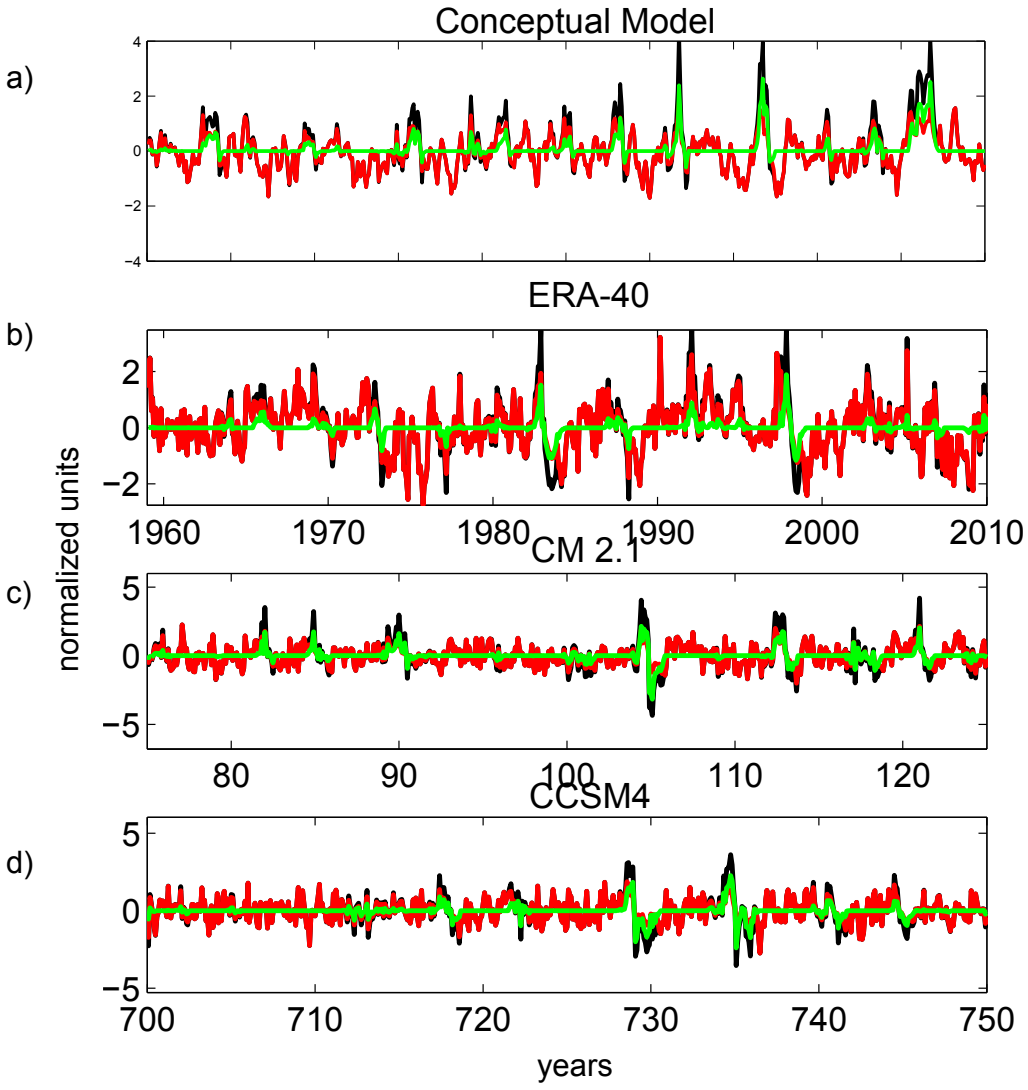

Figure 4.3: Time series of total noise (R_τ, black), additive noise (ξ, red), and multiplicative noise ($BTH(T)\xi$, green) for a) conceptual model with $B = 0.5$ b) ERA-40, c) GFDL CM2.1 d) CCSM4.

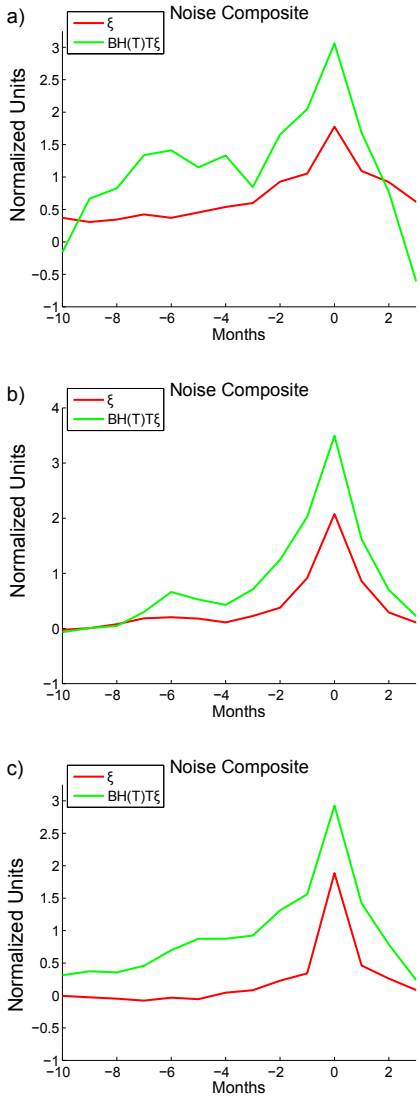

Figure 4.4: Composites in time of the total noise (R_τ), for large additive noise (ξ, red), and multiplicative noise ($BTH(T)\xi$, green) events for a) ERA-40, b) CM2.1 c) CCSM4.

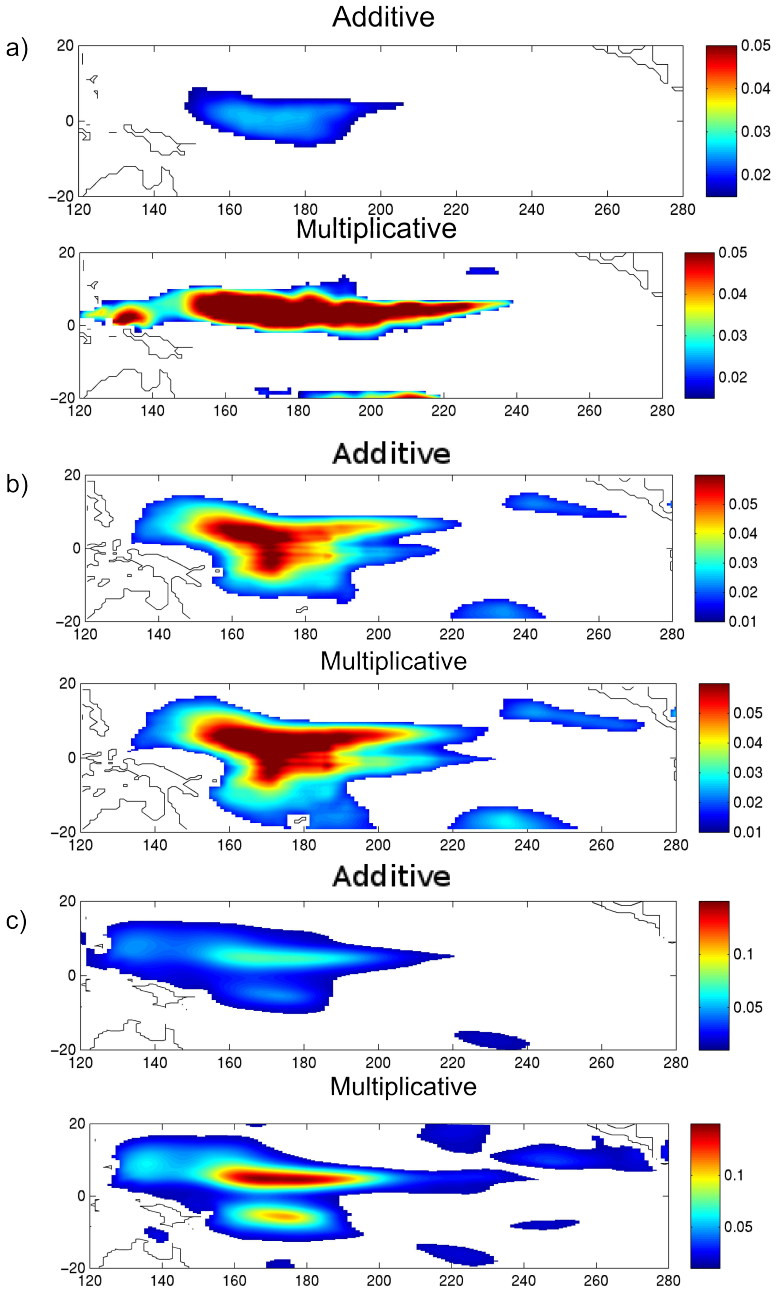

Figure 4.5: Spatial distribution of large additive and multiplicative westerly wind ($\frac{N}{m^2}$ events for a) ERA-40, b)CM2.1 c)CCSM4. The additive events are similar to the large total noise events and the multiplicative events are similar to the extreme events.

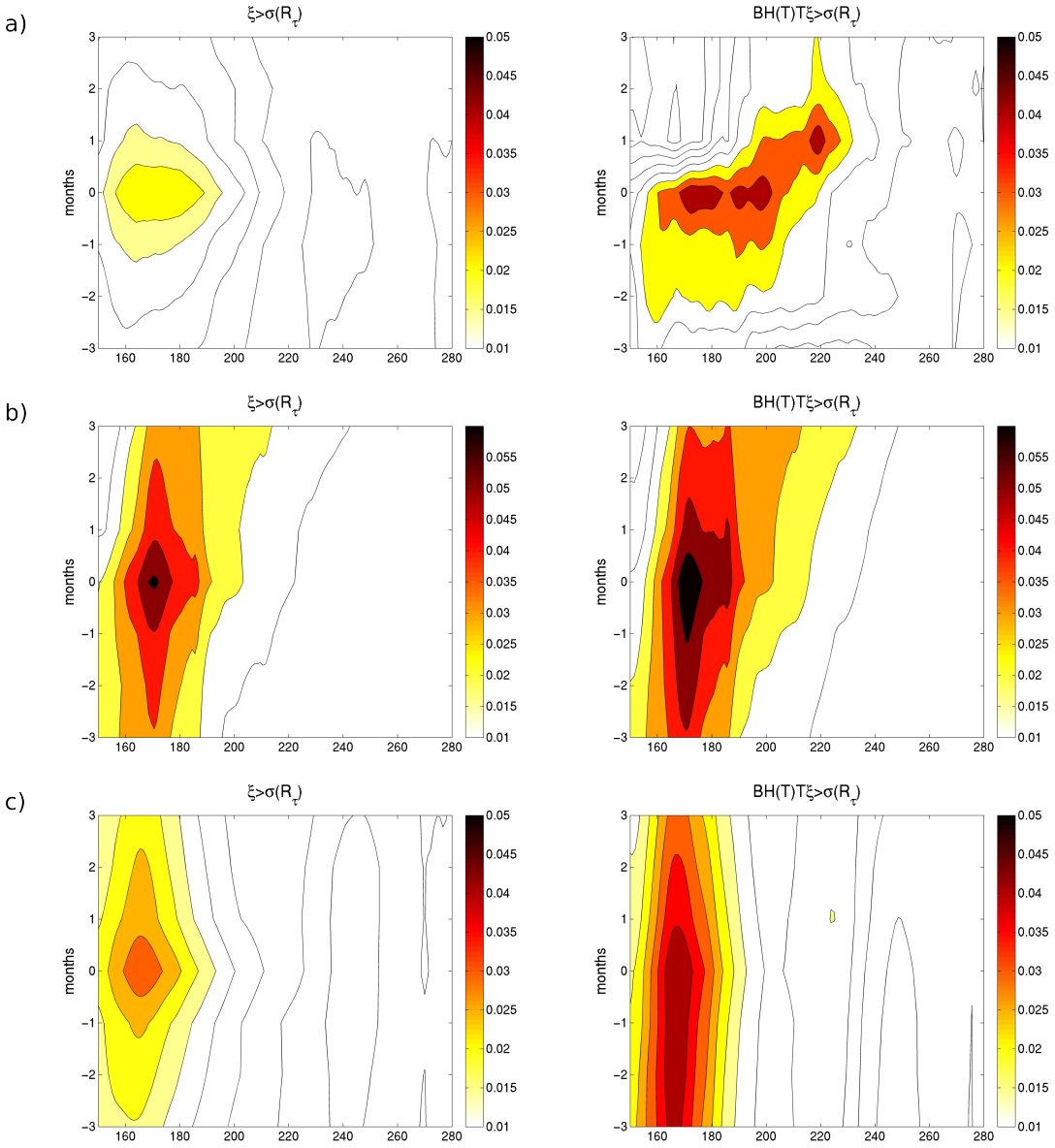

Figure 4.6: Hovmoeller diagrams of the anomalous westerly wind forcing ($\frac{N}{m^2}$) averaged over 5° S - 5° N preceding and following large additive (left) and multiplicative (right) westerly wind events for a) ERA-40, b) GFDL CM2.1 c) CCSM4. The additive events are similar to the large total noise events and the multiplicative events are similar to the extreme events.

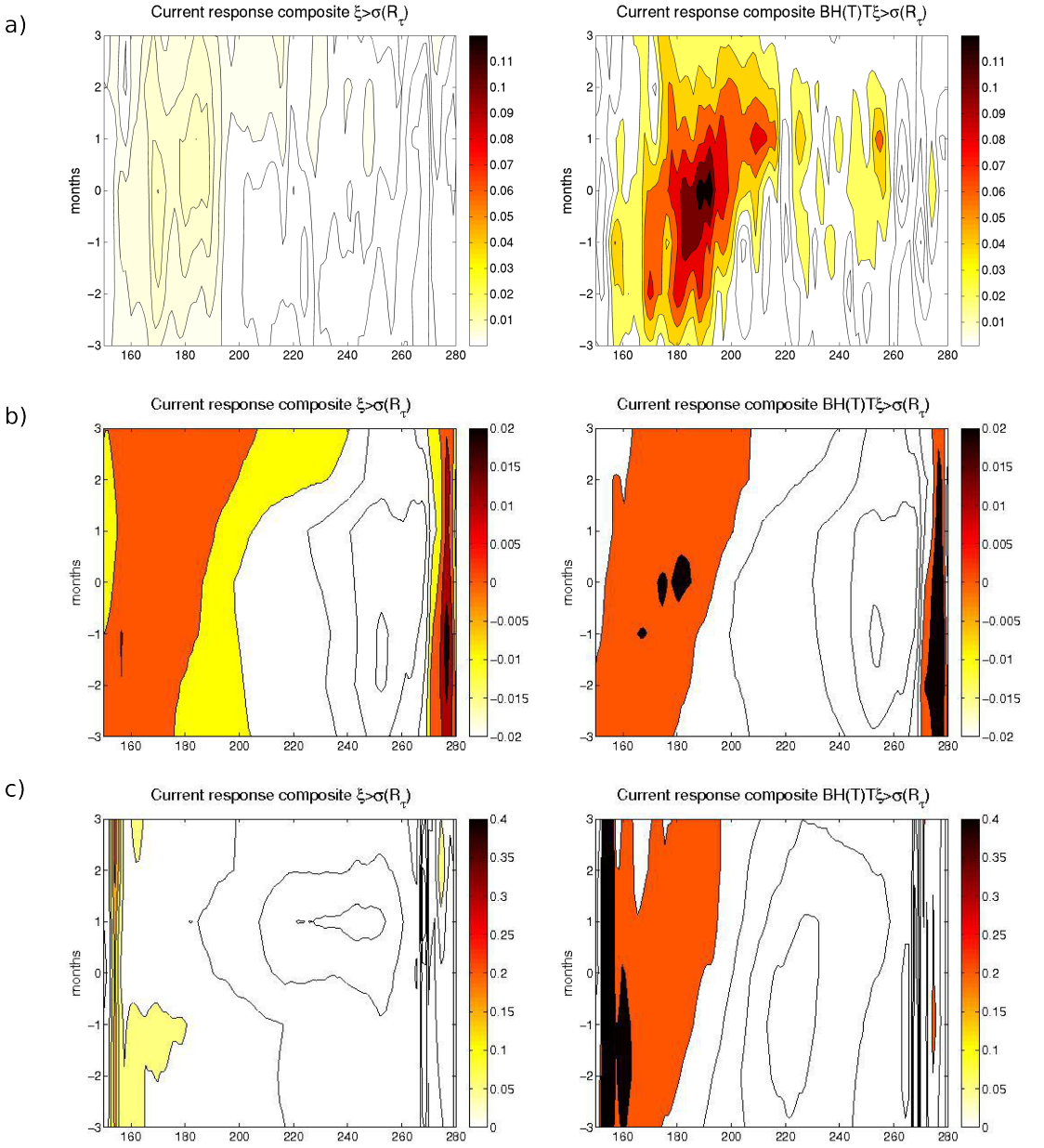

Figure 4.7: Hovmoeller diagrams of the anomalous zonal temperature advection $10^{-5}\frac{K}{s}$ from the upper 50m and averaged over 5° S - 5° N preceding and following large additive (left) and multiplicative (right) westerly wind events for a) ORA-S3, b) GFDL CM2.1 c) CCSM4. The additive events are more single event-like, while the multiplicative events have a longer lasting low-frequency component to it.

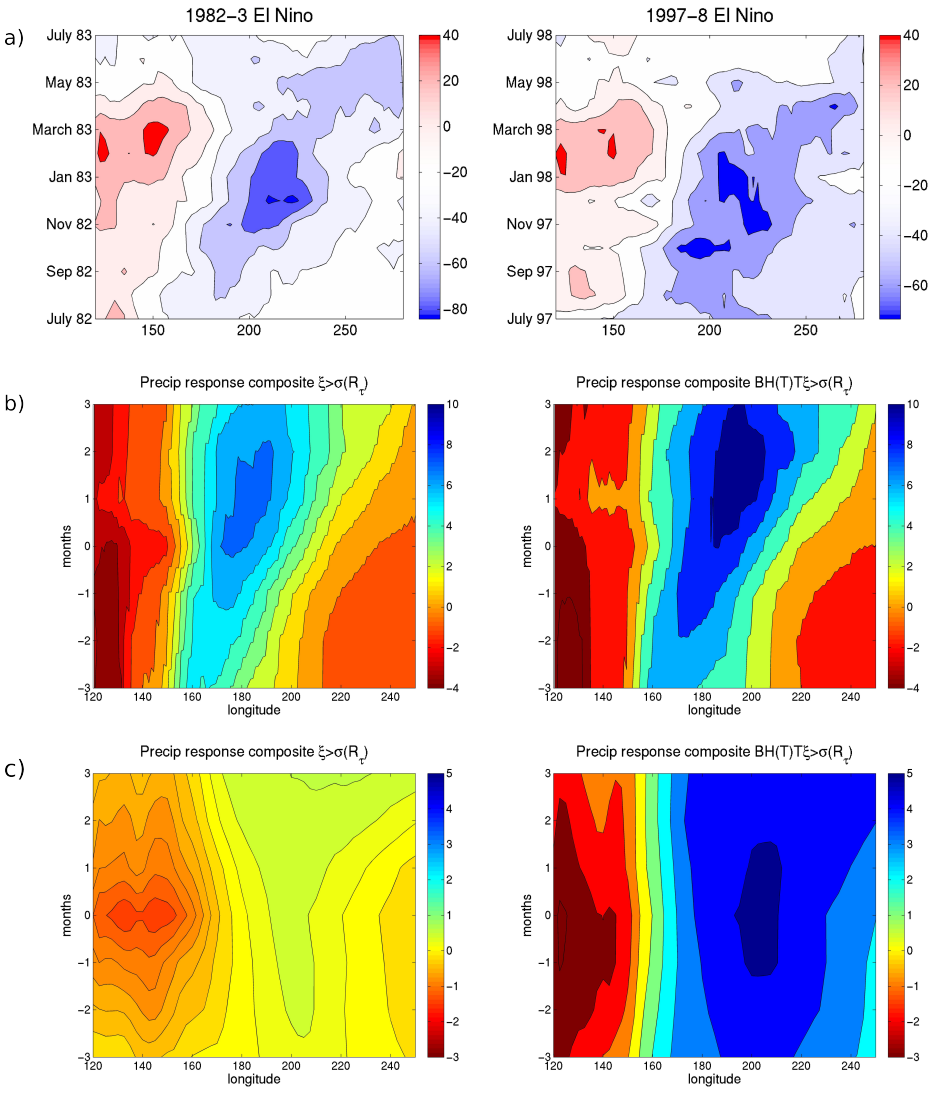

Figure 4.8: Hovmoeller diagrams of a) the anomalous outgoing longwave radiation $\frac{W}{m^2}$ for the 1982-3 and 1997-8 El Niño events and b) and c) the anomalous precipitation ($\frac{mm}{day}$) preceeding and following large additive (left) and multiplicative (right) westerly wind events for GFDL CM2.1 and CCSM4 respectively. The multiplicative noise forcing and the two observed extreme El Niño events show strong eastward propagation.

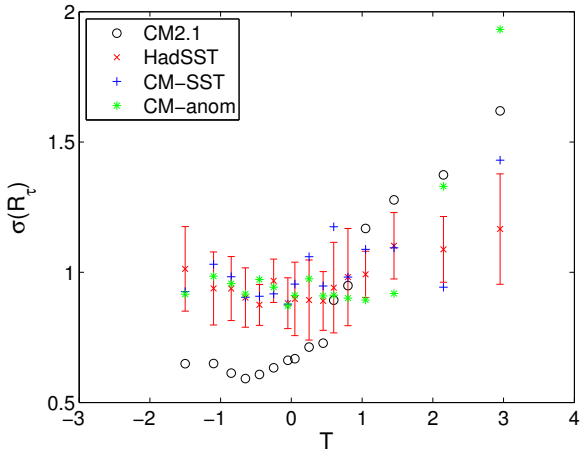

Figure 4.9: The standard deviation of noise forcing as a function of temperature for the 300-year CM2.1 results, the HadISST forced AM2.1 experiment, the CM2.1 SST, and the CM2.1 SST anomaly forced AM2.1 experiments.

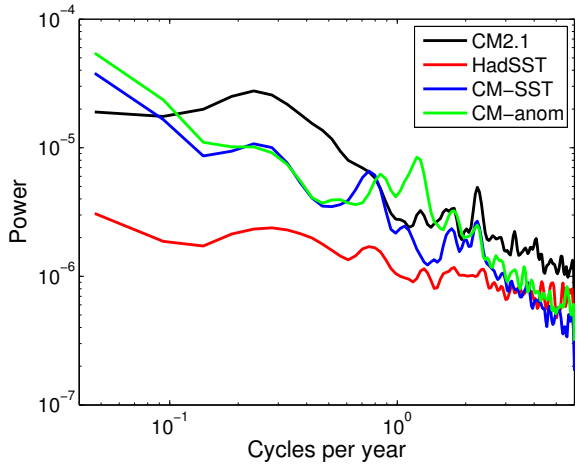

Figure 4.10: The noise spectrum of R_τ for the 300-year CM2.1 results, the HadISST forced AM2.1 experiment, the CM2.1 SST, and the CM2.1 SST anomaly forced AM2.1 experiments.

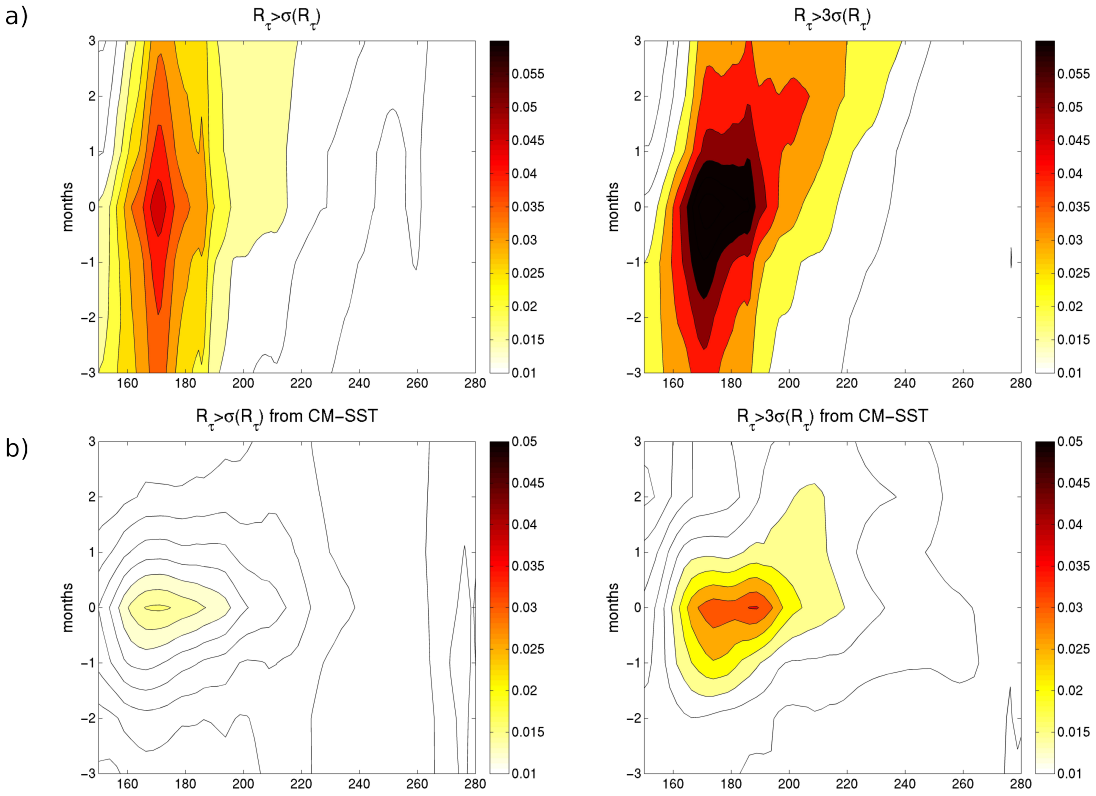

Figure 4.11: Hovmoeller diagrams of the anomalous westerly wind forcing ($\frac{N}{m^2}$ averaged over 5° S - 5° N preceding and following large (left) and extreme (right) westerly wind events for the a) GFDL CM2.1 and b) CM2.1 SST anomaly forced experiment. The extreme events do not show the same magnitude of anomaly or the eastward propagation observed in the coupled scenario.

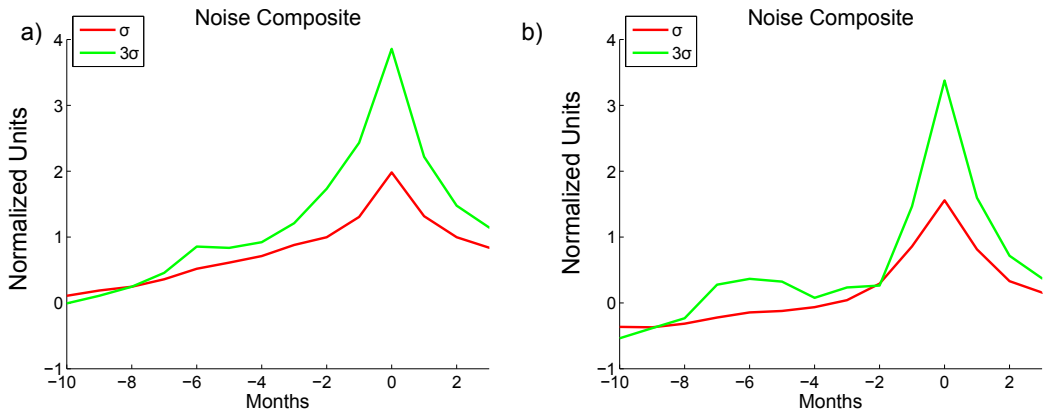

Figure 4.12: Composites in time of the total noise (R_τ), for large additive noise (ξ, red), and multiplicative noise ($BTH(T)\xi$, green) events for a) GFDL CM2.1 b) CM-SST.

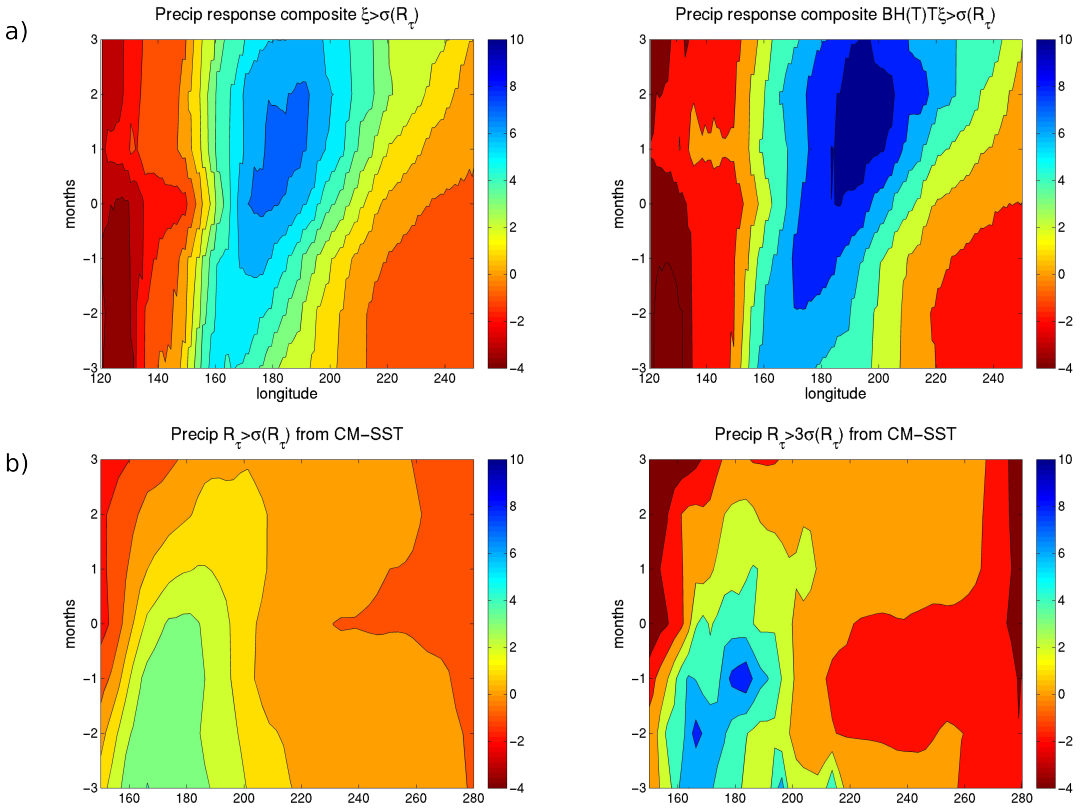

Figure 4.13: Hovmoeller diagrams of the anomalous precipitation ($\frac{mm}{day}$) preceding and following large (left) and extreme (right) westerly wind events for the a) GFDL CM2.1 and b) CM2.1 SST anomaly forced experiment.

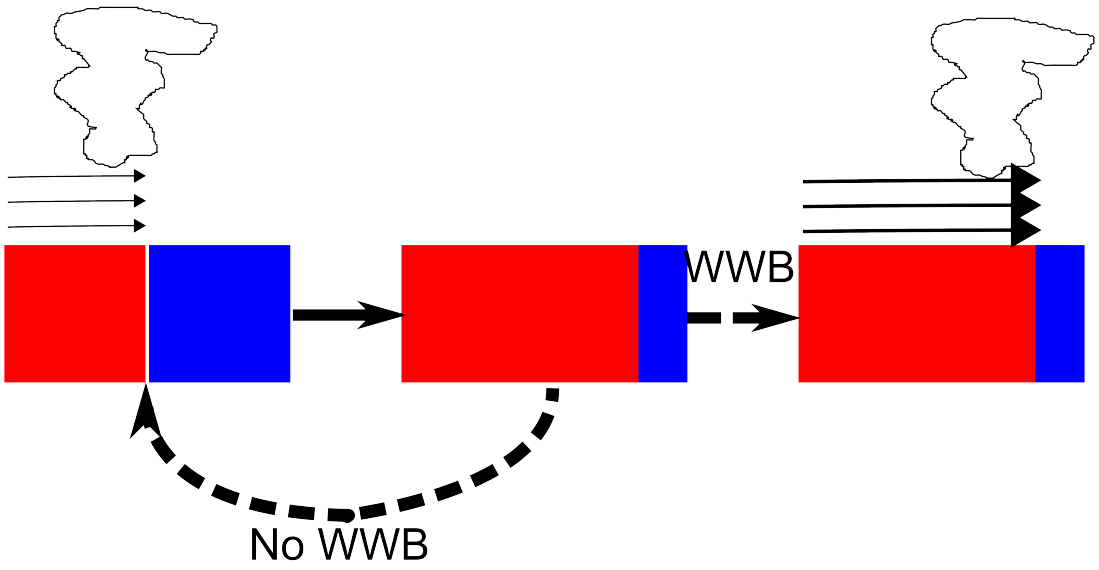

Figure 4.14: A schematic diagram of the interaction of the westerly wind bursts and western Pacific warm pool SSTs. An initial weserly wind burst expands the warm pool to the east. If another westerly wind burst occurs, it has a greater zonal extent and is stronger due to the eastward spread of the warm pool, but if one does not occur, than the warm pool relaxes back to its initial extent.

Chapter 5

The Simulation of ENSO Multiplicative Noise in CMIP5 Models

5.1 Introduction

Coordinated experiments have been run to examine the changes in the climate under anthropogenic climate change. The most recent of these is CMIP5. In CMIP5, the coupled models did a better job of replicating ENSO amplitude, pattern, and period compared with their CMIP3 counterparts (Bellenger et al., 2014). However, the models still struggle to correctly simulating these aspects of ENSO. Further, Bellenger et al. (2014) showed that in many of the models that simulated these properties accurately, the "accuracy" was caused by a cancellation of errors instead of getting the physical processes involved in ENSO correct. Since multiplicative noise is known to affect ENSO properties, it is useful to examine how the different CMIP5 models simulate multiplicative noise forcing of ENSO.

5.2 The Estimation of the State-Dependence of ENSO Noise in the Windstress

5.2.1 State-Dependent Noise

The coordinated model experiments and archived data from CMIP5 allow for testing the accuracy of the current generation of climate models with respect to simulating the multiplicative noise forcing of ENSO. In this chapter, 21 different CMIP5 models for the pre-industrial control (piControl), RCP4.5, RCP8.5 scenarios as well as for reanalysis (HadISST and ERA-40 winds), the CM2.1 1990 control and CCSM4 2° pre-industrial control simulation previously used are compared. The pre-industrial control simulation is a long continuous model simulation where the greenhouse gas levels are held constant at levels from before the industrial revolution. RCP4.5 and RCP8.5 are experiments that project the climate into the future by estimating different amounts of greenhouse gasses that are emitted into the atmosphere over the course of the simulation. These simulations extend at a minimum through 2099. Some modelling groups extend the simulation further. Additionally, many of the modelling groups have run multiple realizations of the experiments. The length of data used for each simulation is shown in Table 5.1.

Using the methodology outlined in chapter 2, the magnitude of B can be estimated for the different models across the different scenarios (Table 5.2). The standard deviation of R_τ as a function of ENSO state shows significant uncertainty between the models and scenarios (Figure 5.1). Many models fail to capture any change of noise variance with a positive ENSO state. During a negative ENSO state, most of the models that have a variance increase during the positive ENSO state show little or no change in the noise variance. This agrees with the previous conclusion that there is a threshold non-linearity involved in the formation of multiplicative noise. A few models show an increase in the noise variance during a negative ENSO state. Most of these cases have a reduced rate of change of noise variance in the negative ENSO state compared with the positive one, with CanESM2 being the notable exception.

B is evaluated in the other scenarios as well (Figure 5.2). In this figure, the solid

line is the estimated value from the reanalysis and the dashed lines are $\pm 1\sigma$. More than half of the models fail to simulate B within this interval in the pre-industrial control simulation. In all but one of these cases, GFDL-CM3, the value of B is too low. In examining the global warming simulations, most of the models do not have a consistent trend from the pre-industrial control simulation to RCP4.5 to RCP8.5. Three of the models, ACCESS-1.0, CESM1-CAM5, and GFDL-CM3, show significant increases from preindustrial control to both RCP4.5 and RCP8.5. Of these, only CESM1-CAM5 has a pre-industrial control simulation within the estimated range of B from the reanalysis. ACCESS-1.0 has too small of a simulated B and GFDL-CM3 has too large of a simulated B. Three models, CCSM4, CNRM-CM5, and IPSL-CM5A-LR, show a consistent significant decrease in B from the pre-industrial control simulation to RCP4.5 and RCP8.5. Only two, CCSM4 and CNRM-CM5, of these three models have a reasonable simulation of B in the pre-industrial control simulations. IPSC-CM5A-LR has too weak a simulation of B. Overall, it is clear that the CMIP5 models do a poor job in simulating B and have too wide a variance on the change of B due to climate change to draw any strong conclusions as to how this processes will be effected. Our attempts at drawing any strong conclusions about the changes in B due to climate change are also hampered by the uncertainty in estimating B.

Initially, limiting the analysis to the pre-industrial control simulations, the model mean state biases are examined. In the previous chapter, convection and the Warm Pool edge were found to be important for multiplicative noise, therefore, the SST in the central Pacific is examined. The estimated value of B is correlated with the model temperature bias in the central Pacific (3° S-3° N, 160° W- 160° E), $r = 0.32$ (Figure 5.3). This correlation with the model Cold Tongue bias is consistent with the physical mechanism explored in Chapter 4. While graphically clear with a few outliers, the correlation of the temperature bias to the B is low suggesting that there are other factors responsible for the poor simulation of B. These causes could include, but are not limited to, convective biases and model representation of the MJO or WWBs. A future study into the poor simulation of B in the models should take this into account to test other possible causes that factor into the models' poor performance in simulating B.

In agreement with this, the spatial pattern of tropical temperature anomaly, defined as $T' = T(x, y) - \bar{T}$, where $\bar{T}$ is the global mean tropical temperature, shows a significant correlation of positive anomalies in the central Pacific and larger values of B (Figure 5.4). There are also significant negative correlations in the equatorial Indian Ocean and eastern Pacific. In the eastern Pacific Ocean, the correlation maximum occurs north of the equator and not on the equator. This could be related to the simulation of the equatorial cold tongue and resultant warming of off-near equatorial SSTs as a result.

The correlations with precipitation are more complicated. B is positively correlated with increases in precipitation over the equatorial cold tongue region and generally drier areas of the tropics while it is negatively correlated with precipititation in the Inter-Tropical Convergence Zone (ITCZ) and South Pacific Convergnce Zone (SPCZ) regions (Figure 5.5). The relationship between the precipitation in the cold tongue region and B is potentially another manifestation of the cold tongue bias which inhibits the eastward propagation of the WWBs by inhibiting convection further to the east. Combined with the anti-correlation of the precipitation in the northeast Pacific ITCZ and B, the meridional contrast of precipitation in the eastern equatorial Pacific is on the whole anticorrelated to B. Merkel et al. (2010) and Watanabe et al. (2011) found that ENSO amplitude is anticorrelated to the meridional contrast in precipitation. Since, Jin et al. (2007) and Levine and Jin (2010) found that ENSO amplitude is directly proportionaly to B, these results are in agreement with the previous studies linking ENSO amplitude and eastern Pacific meridional precipitation contrast.

5.2.2 Total Windstress Noise Forcing

In equation (2.2), the noise forcing of ENSO is represented as

$$F = \sigma_N[1 + BH(T)T]\xi \tag{5.1}$$

Described in this manner, B is dependent on σ_N. σ_N represents the magnitude of the noise forcing of ENSO. The magnitude of the noise forcing has been shown to be important for ENSO amplitude (Jin et al., 2007; Levine and Jin, 2010). Therefore, the

standard deviation of R_τ is used as a proxy value for σ_N and is compared across the different CMIP5 models and the reanalysis (Table 5.3). With three exceptions, CESM1-CAM5, CMCC-CMS, and GFDL-ESM2M, $\sigma(R_\tau)$ is underestimated in the pre-industrial control simulations (Figure 5.6). This underestimation of the windstress noise forcing could be related to coupled models' inability to correctly simulate the MJO. In about half of the models, the value of $\sigma(R_\tau)$ is fairly constant across the different global warming scenarios. Seven of the models show decreases in $\sigma(R_\tau)$ with anthropogenic climate change and three show consistent increases. The rest do not have a consistent direction of change in the global warming simulations.

The windstress noise forcing is positively correlated, although not significantly, with increased tropical temperature anomalies along the equator in the western and central Pacific, presumaly due to the relationship between SST and precipitation in that region where SSTs lies near or above the convective threshold (Figure 5.7). There are narrow regions of negative correlations on either side of this positive correlation. This is assumed to be related to the correct location of the ITCZ and SPCZ and the role that convection in those areas plays in producing equatorial windstresses. There are also negative correlations in the tropical Indian Ocean and Maritime continent region perhaps related to poorly simulated MJO variability and propagation from the Indian ocean through to the Pacific.

The increase in variance of the total noise created by the state-dependent component of the noise is small enough that it does not contribute in large quantities to the total windstress noise forcing of ENSO. This relationship leads to a small correlation, $r = 0.4$, between B and $\sigma(R_\tau)$ (Figure 5.8). While the larger values of B all occur at larger values of $\sigma(R_\tau)$, the smaller values of B are not confined to the smaller values of $\sigma(R_\tau)$. An unusual feature seen in Figure 5.8 is that the largest values of B occur around the middle values of $\sigma(R_\tau)$. However, all three of those extreme B values are from GFDL CM3, which suggests that that feature is due to a single model and not an important part of the relationship between B and $\sigma(R_\tau)$.

ENSO magnitude is related to the noise magnitude and the magnitude of the state-dependence factor (Jin et al., 2007; Levine and Jin, 2010). It was shown that in the

simple conceptual model,

$$Gr \approx \frac{\sigma^2(R_\tau)B^2/r + \lambda}{2} \tag{5.2}$$

where r is the red noise timescale and λ is the linear growth rate. The magnitude of the windstress noise forcing and the magnitude of ENSO are correlated at $r = 0.67$ (Figure 5.9). Given the effect of linear growth rate on ENSO magnitude, this is a strong relationship. Also, not considered here are other types of noise forcing on ENSO, which could change the value of the total noise forcing and this relationship. Although there are not enough points at the higher values of windstress noise forcing to fully determine the relationship between the ENSO magnitude and windstress forcing, the ENSO magnitude appears to approach an asymtote where the windstress forcing can no longer increase the ENSO magnitude. This could be a real part of the system due to non-linear controls on ENSO magnitude or it could also be a result of coupled model tuning of ENSO magnitude.

5.3 Simulated Changes to ENSO Noise Forcing Due to Climate Change

The multi-model ensemble change in B due to climate change is small and not robust due to the large variability between the different models' respective change and the uncertainty in the estimate of B. Only 10 models show large changes, $\Delta B > 0.1$, between the pre-industrial control and RCP4.5 simulations and 9 show large changes between the pre-industrial control and RCP8.5 simulations. Of those changes, 13 show a decrease in B and 6 show an increase. The large variability between models and the lack of consistent changes due to climate change in the models' estimation of the state dependence is similar to the uncertainty in predicting the changes to ENSO under climate change and may point to a direction for improving ENSO simulation in the models.

Examining only the models and scenarios with large changes in B between the pre-industrial control simulation and the different RCP scenarios, a better understanding of the role of the tropical Pacific mean climate state can be developed. The change in B due

to climate change is compared with the spatial pattern of changes in tropical temperature. The spatial pattern of warming due to climate change is described by the difference in the total change in temperature as a function of latitude and longitude from the change in tropical mean temperature. There are areas of significant correlations along the cold tongue, the South American coast, and the eastern Pacific ITCZ (Figure 5.10). The change in B is positively correlated with relative increases in SST in the eastern Pacific ITCZ region and negatively correlated with changes in the western Pacific warm pool region and SPCZ. Considering the non-statistically significant correlations, the general pattern is that if there is greater warming in the equatorial central Pacific and along the Cold Tongue, there is an increase in B. The expansion of this into the western Pacific Warm Pool region is due to the multi-model ensemble (MME) Cold Tongue bias where the cold tongue extends too far to the west. The significant negative correlations with changes in southern tropical Pacific are presumably related to shifts in the SPCZ and the double ITCZ bias found in most couple models. The relationship between B and the change in tropical temperature distribution is consistent with the role of convection found previously and in the effects of convective parameterization on ENSO amplitude found by Watanabe et al. (2011) as well as the previously found relationship with the cold tongue bias.

Using the 19 simulations that show large changes in B from the pre-industrial control simulation, the changes in the precipitation are examined (Figure 5.11). Positive changes in the precipitation over the central and eastern Pacific are correlated with increases in B. The increase in the standard deviation of precipitation shows a greater variability of preciptation is associated with increases in B. This is consistent with the westward propagation of precipitation shown to coexist with the multiplicative noise forcing as opposed to the additive noise forcing cases in Chapter 4. Further, given the relationship of B and ENSO amplitude predicted by Jin et al. (2007) and Levine and Jin (2010) and shown in Figure 5.9, this result suggests that an increase in B corresponds to increased eastward spread of precipitation and more extreme ENSO events from the Cai et al. (2014) definition.

The relationship of the changes of $\sigma(R_\tau)$ to the changes in tropical SST distribution

are small (Figure 5.12). The only significant correlations exist with the SSTs slightly to the east of the examined region. This suggests that an important component of getting the ENSO noise forcing magnitude correct is the Cold Tongue bias. It is also consistent with the mechanism for eastward propagation of the westerly winds in the region. Since precipitation is confined to tropical regions of sufficient temperature, a decrease in SST gradient across the equatorial Pacific would allow for greater eastward propagation of the precipitation. If this eastward propagation of the precipitation allows more precipitation to occur to the east of the forcing box, then there will be an increase in the occurrence of westerly wind anomalies within the forcing region. This increase of westerly wind anomalies will increase the standard deviation of the residual within the forcing region because it represents the increased variaiblity from the climatic easterlies that occur in that region. This result suggests that overall spatial warming pattern of the equatorial Pacific is important to understanding future ENSO forcing changes.

5.4 Summary

The methodology used to estimate B developed in Chapters 2 and 3 is applied to 21 different CMIP5 models over the pre-industrial control and 2 different global warming scenarios. More than half of the models underestimate B. The poor model performance in simulating multiplicative noise is shown to be related to the model biases in the Cold Tongue and Tropical precipitation. Changes in tropical temperature distribution and precipitation are shown to have a potential impact on B in the future. However, due to the multiple uncertainties related to the models' simulation of B, there is no robust change in B due to anthropogenic climate change.

The magnitude of the noise forcing, $\sigma(R_\tau)$, is also examined across the 21 different CMIP5 models and 3 different climate scenarios. All but three of the different models underestimate the magnitude of the noise forcing. The underestimation of $\sigma(R_\tau)$ is found to be related to the Cold Tongue bias and potentially to the models' poor simulation of the MJO. Again, no consistent change due to anthropogenic climate change is found. The poor simulation of both B and $\sigma(R_\tau)$ in the climate models suggests that there are still

Table 5.1: Number of years used for each of the CMIP5 models and scenarios.

	Model	piControl	RCP 4.5	RCP 8.5
1	ACCESS1-0	500	95	95
2	ACCESS1-3	500	95	95
3	CanESM2	996	875	380
4	CCSM4	501	674	475
5	CESM1-BGC	500	95	95
6	CESM1-CAM5	319	485	285
7	CMCC-CM	330	95	95
8	CMCC-CMS	500	95	95
9	CNRM-CM5	850	295	675
10	CSIRO-Mk3-6-0	500	N/A	95
11	EC-EARTH	452	1140	950
12	FIO-ESM	800	285	95
13	GFDL-CM3	800	485	95
14	GFDL-ESM2G	500	95	95
15	GFDL-ESM2M	500	95	95
16	inmcm4	500	95	95
17	IPSL-CM5A-LR	1000	580	580
18	IPSL-CM5A-MR	300	295	N/A
19	IPSL-CM5B-LR	300	95	95
20	MRI-CGCM3	500	95	95
21	NorESM1-M	501	295	95

physical processes that these models are not correctly representing that are important to the correct simulation of the tropical climate. If the struggles simulating B and $\sigma(R_\tau)$ are related to the Cold Tongue bias, it is possible that improving the simulation of them will reduce the Cold Tongue bias, or that reducing the Cold Tongue bias will improve the simulation of B and $\sigma(R_\tau)$ and therefore improve the simulation of ENSO.

Table 5.2: Value of B for all models and scenarios used. The uncertainty of the estimation is a function of data length and magnitude of B. From estimates using the conceptual model, for data lengths of approximately 100 years, the uncertainty is approximately ± 0.1.

Model	piControl	RCP 4.5	RCP 8.5
ACCESS1-0	0.05	0.10	0.17
ACCESS1-3	0.30	0.11	0.17
CanESM2	0.08	-0.01	0.08
CCSM4	0.42	0.34	0.33
CESM1-BGC	0.46	0.25	0.37
CESM1-CAM5	0.30	0.47	0.53
CMCC-CM	0.06	0.00	0.03
CMCC-CMS	0.07	0.20	0.06
CNRM-CM5	0.35	0.22	0.19
CSIRO-Mk3-6-0	0.05	N/A	-0.03
EC-EARTH	0.07	0.14	0.18
FIO-ESM	0.39	0.28	0.36
GFDL-CM3	0.58	0.68	0.73
GFDL-ESM2G	0.15	-0.02	0.23
GFDL-ESM2M	0.36	0.38	0.32
inmcm4	0.08	0.06	0.08
IPSL-CM5A-LR	0.03	-0.04	-0.10
IPSL-CM5A-MR	0.12	-0.01	N/A
IPSL-CM5B-LR	0.18	0.04	0.07
MRI-CGCM3	0.21	0.05	0.34
NorESM1-M	0.23	0.05	0.18

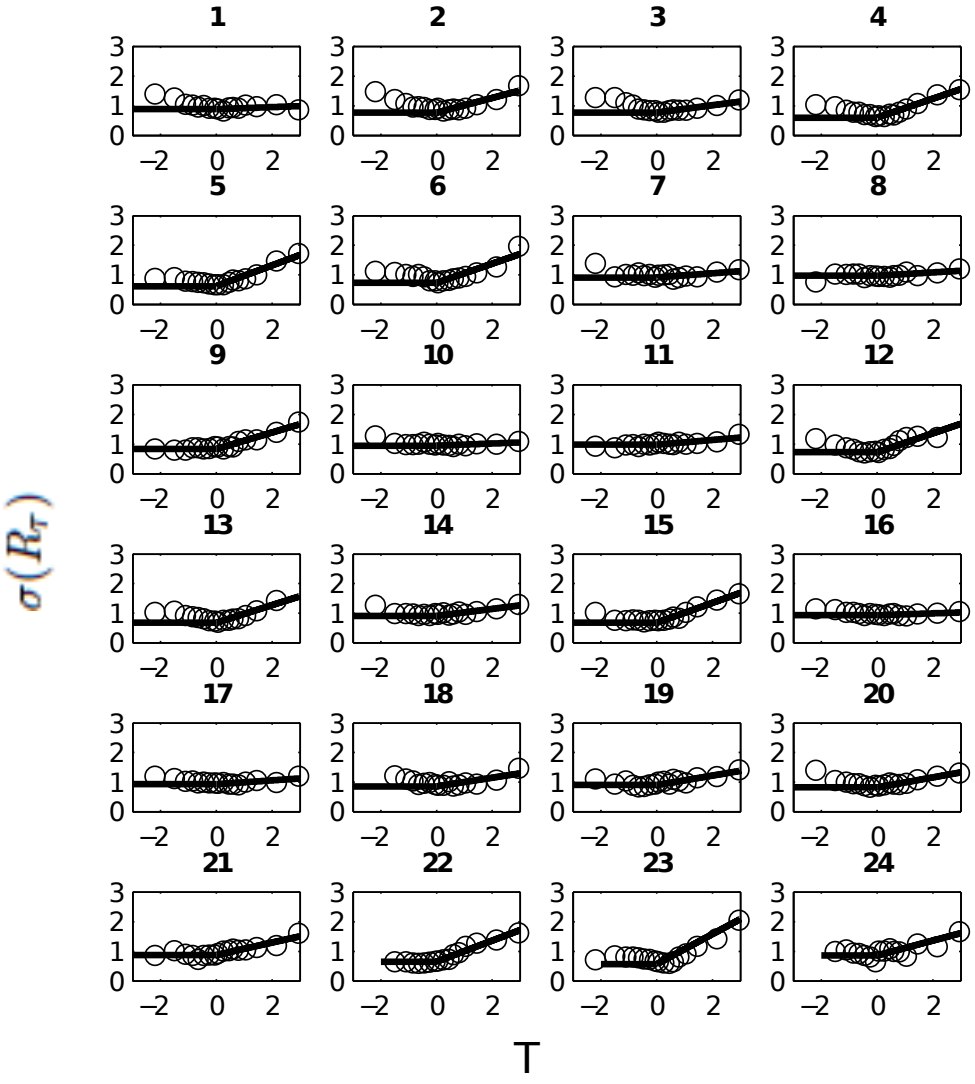

Figure 5.1: Standard deviation of R_τ as a function of ENSO state for CMIP5 models pre-industrial control simulation. Most models do not capture the multiplicative noise process correctly. Numbers refer to the numbers on Table 1. Plots 22, 23, 24 are CM2.1, CCSM4 2 degree simulation, and the reanalysis, respectively.

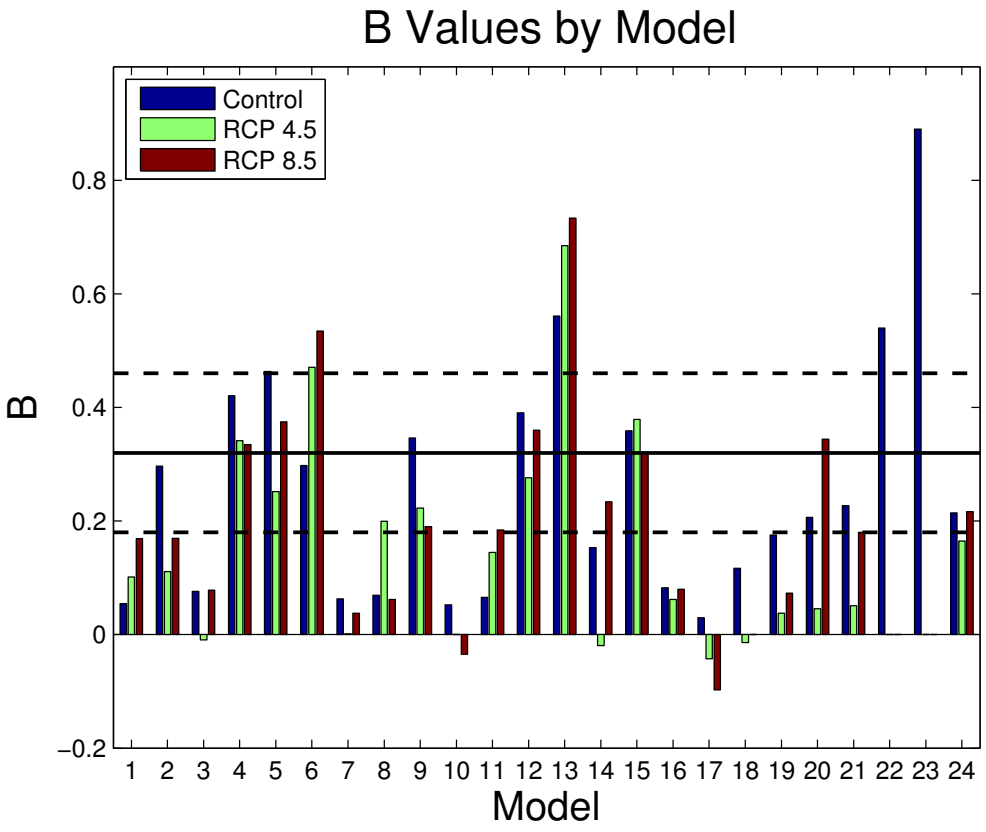

Figure 5.2: B as simulated by all the models. The solid line is the estimate from reanalysis and the dashed lines are $\pm\sigma$. Most models do not capture the multiplicative noise process correctly. Numbers refer to the numbers on Table 1. Plots 22, 23, 24 are CM2.1, CCSM4 2 degree simulation, and the MME respectively.

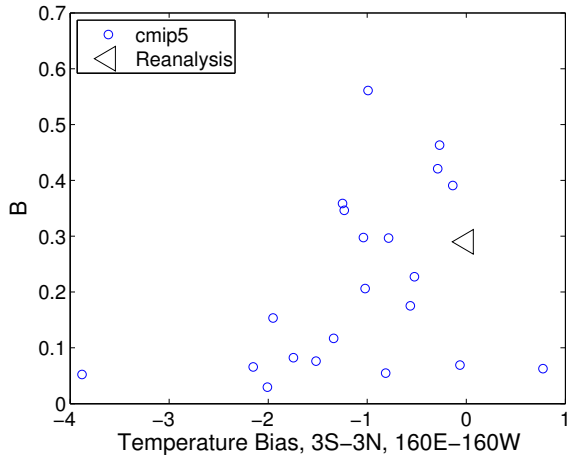

Figure 5.3: CMIP5 pre-industrial control simulations B versus the area averaged temperature bias from observations along the western Pacific warm pool edge from 160E-160W, 3S-3N. A correlation of $r = 0.35$ is found.

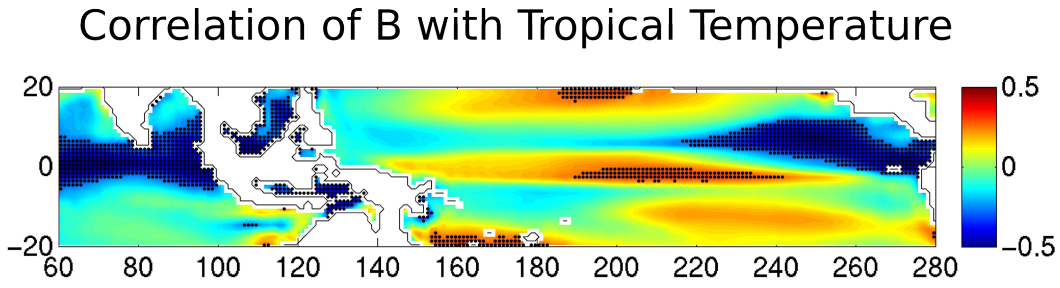

Figure 5.4: Correlation of B with $(T - \bar{T})$ for all models. The regions with statistical significance have stipling.

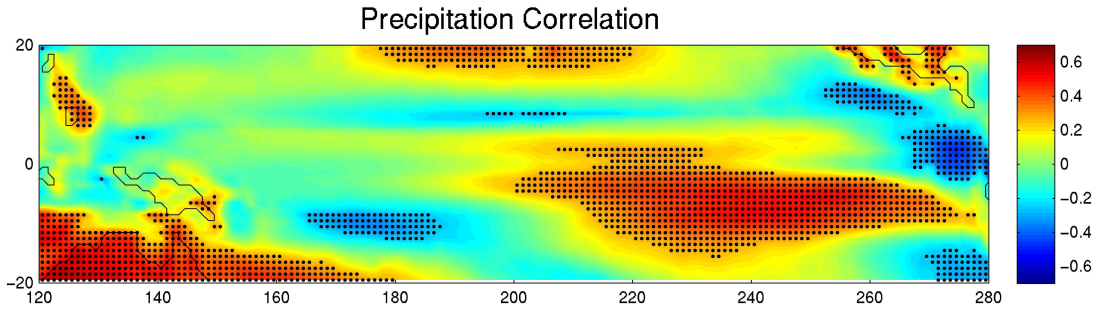

Figure 5.5: Correlation of B with precipitation for all models. The regions with statistical significance have stipling.

Table 5.3: Value of $\sigma(R_\tau)$ for all models and scenarios used.

Model	piControl	RCP 4.5	RCP 8.5
ACCESS1-0	0.0070	0.0066	0.063
ACCESS1-3	0.0070	0.0073	0.0070
CanESM2	0.0061	0.0050	0.0047
CCSM4	0.0098	0.0080	0.0080
CESM1-BGC	0.0095	0.0085	0.0085
CESM1-CAM5	0.0082	0.0112	0.0126
CMCC-CM	0.0073	0.0054	0.0063
CMCC-CMS	0.0121	0.0133	0.0128
CNRM-CM5	0.0099	0.0109	0.0106
CSIRO-Mk3-6-0	0.0085	N/A	0.0109
EC-EARTH	0.0079	0.0085	0.0113
FIO-ESM	0.0116	0.0103	0.0104
GFDL-CM3	0.0085	0.0099	0.0091
GFDL-ESM2G	0.0078	0.0082	0.0080
GFDL-ESM2M	0.0125	0.0123	0.0124
inmcm4	0.0044	0.0046	0.0043
IPSL-CM5A-LR	0.0059	0.0058	0.0070
IPSL-CM5A-MR	0.0071	0.0063	N/A
IPSL-CM5B-LR	0.0080	0.0080	0.0065
MRI-CGCM3	0.0074	0.0072	0.0068
NorESM1-M	0.0068	0.0065	0.0064

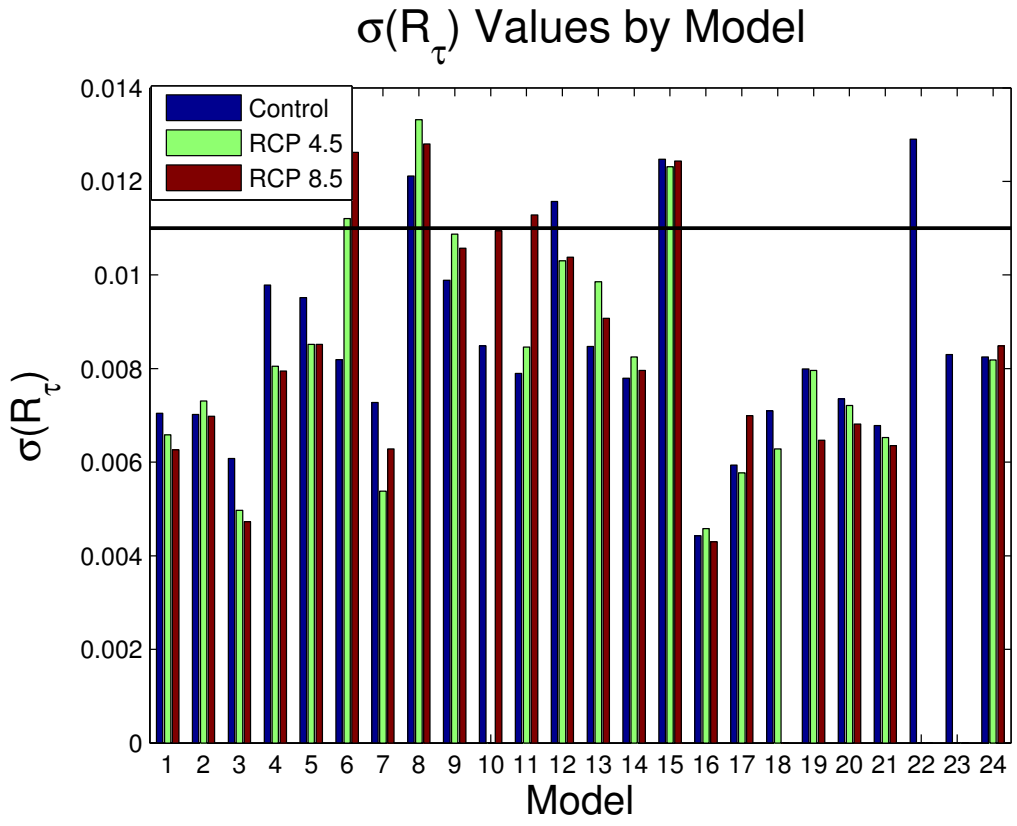

Figure 5.6: The standard deviation of the noise time series, $\sigma(R_\tau)$, as simulated by all the models. The solid line is the estimate from reanalysis. Numbers refer to the numbers on Table 1. Nearly every model underestimates this value compared with the reanalysis. Plots 22, 23, and 24 are CM2.1, CCSM4 2 degree simulation, and the MME respectively.

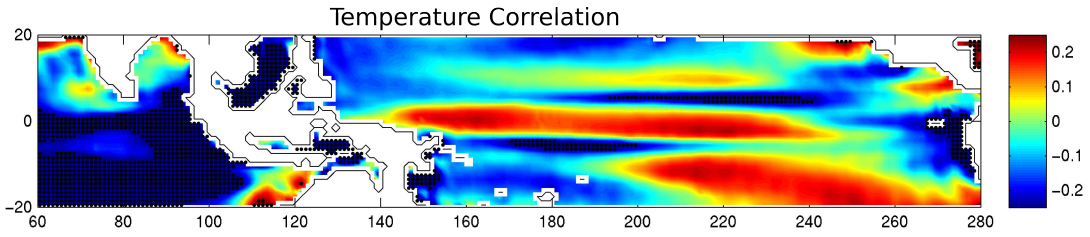

Figure 5.7: Correlation of $\sigma(R)$ with $(T - \bar{T})$ for all models. The regions with statistical significance have stipling.

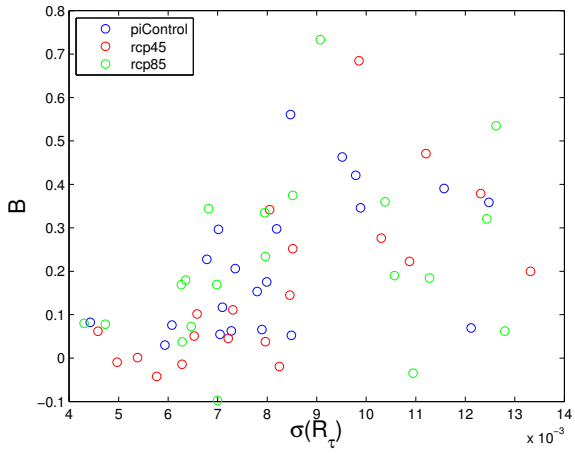

Figure 5.8: The relationship of B and $\sigma(R)$. Most models that underestimate B underestimate $\sigma(R)$ proportionately. Meanwhile, models that overestimate B tend have an anti-correlation with σ.

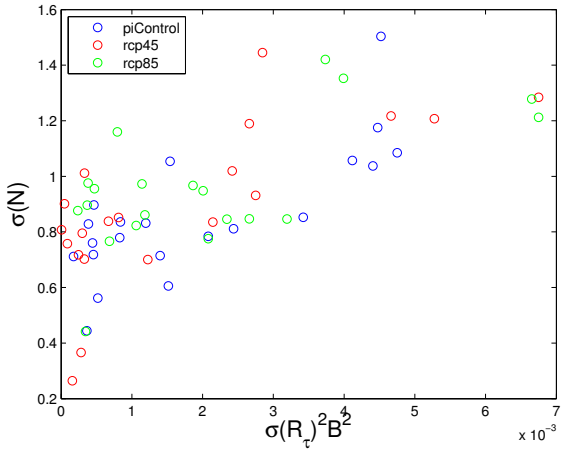

Figure 5.9: $B^2\sigma^2$ is related with ENSO growth rate and amplitude. The correlation in the CMIP5 models between $B^2\sigma^2$ and $\sigma(N)$ is $r = 0.67$.

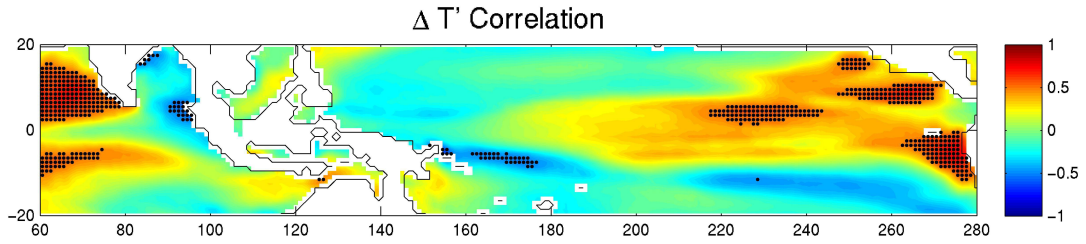

Figure 5.10: Correlation of ΔB with ΔT for models with $\Delta B > 0.1$. Large areas of positive correlation exist in the cold tongue region and a negative correlation exists in the warm pool. The stippling denotes statistical significance.

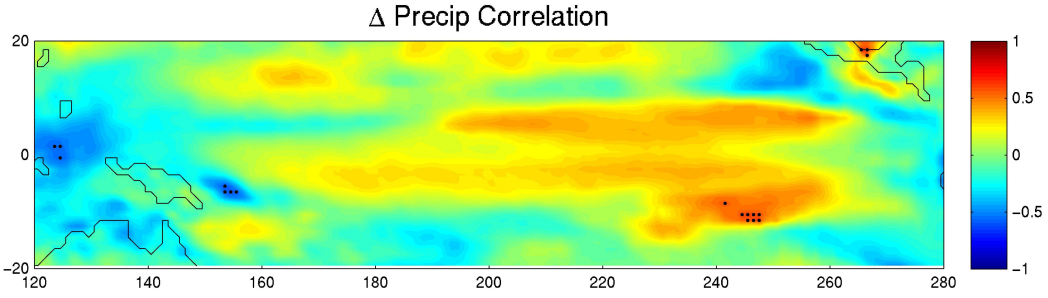

Figure 5.11: Correlation of ΔB with Δ precipitation for models with $\Delta B > 0.1$. Large areas of positive correlation exist in the cold tongue region suggesting an increase in precipitation variability in the region. The stippling denotes statistical significance.

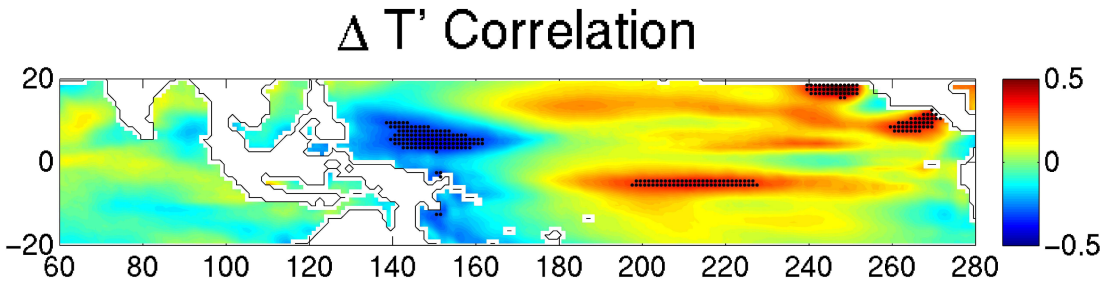

Figure 5.12: Correlation of $\Delta\sigma$ with ΔT. Large areas of positive correlation exist in the cold tongue region and a negative correlation exists in the warm pool. The stippling denotes statistical significance.

Chapter 6

Extreme El Niño Events

6.1 Introduction

Using precipitation as a metric, Cai et al. (2014) found that in response to global warming the number of extreme El Niño events significantly increased. Extreme El Niño events have a much larger societal impact than regular El Niño events. Damage from the impacts associated with the 1997-8 event are estimated at over 35 billion USD (Nicholls, 2001). Due to the costly potential impacts of extreme El Niño events, it is important for disaster mitigation and resiliency planning to understand the predictability and the frequency of occurrence of these extreme events. Here, a potential cause for the change in frequency of extreme El Niño events is examined from both a theoretical view point and within the coupled climate models.

Jin et al. (2007) found that in the conceptual recharge oscillator model, the addition of multiplicative noise forcing created more large El Niño events while not enhancing La Niña in the same manner. These distributional differences echoed the findings of Perez et al. (2005) where state dependent forcing was applied to an intermediate ENSO model and found to produce a more realistic ENSO distribution than additive noise alone. Following up, Levine and Jin (2010) found that increasing the magnitude of the state-dependence of the multiplicative noise increased the number of extreme El Niño events and that the skewness was more strongly influenced by noise-induced instability

than the lower order moments like variance and mean. Given these previous findings of the effect of multiplicative noise on ENSO skewness and extreme events, the application of the method of estimation of the state-dependence factor of multiplicative noise to the coupled models allows the theoretical results to be further scrutinized amongst the coupled models.

6.2 A Theory for the Relationship of Multiplicative Noise to ENSO Skewness

6.2.1 Theory and Conceptual Model

Multiplicative noise has been shown to impact ENSO amplitude and skewness (Eisenman et al., 2005; Jin et al., 2007; Gebbie et al., 2007; Perez et al., 2005; Gebbie and Tziperman, 2009b; Levine and Jin, 2010). From the conceptual model, it can be shown that ENSO amplitude is also strongly influenced by linear ENSO growth rate and noise amplitude (Jin et al., 2007; Levine and Jin, 2010). However, the skewness of ENSO, where skewness is defined as $S = \frac{\bar{T'^3}}{(\bar{T'^2})^{3/2}}$, being a higher moment, is influenced significantly more by the state-dependence factor (Sardeshmukh and Sura, 2009; Levine and Jin, 2010). It can be derived that the skewness of ENSO is linearly proportional to B if the multiplicative noise does not have a threshold non-linearity (see Appendix 1 for derivation) (Personal Communication, Jin).

$$S \propto \frac{2Ba}{\lambda^2 + \frac{\omega^2}{2}} \tag{6.1}$$

where λ is the growth rate, ω the frequency, and a is an empirical closure constant, which Levine and Jin (2010) found to be $a \approx 0.7$. This result is further supported by conceptual model results from a series of 50,000 year integrations (Figure 6.1). Here the conceptual model is run with multiplicative noise both with and without the threshold non-linearity. If the threshold non-linearity is included in the multiplicative noise, the skewness has a non-linear relationship with B. For the values of B examined, the threshold non-linearity reduces the skewness of ENSO.

6.2.2 CMIP5 Models Results

As previously discussed, the coupled models, while improved in their representation of ENSO, still have significant difficulties in reproducing certain aspects of ENSO (Bellenger et al., 2014). The spatial pattern of tropical Pacific SST skewness is compared between the models and reanalysis (Figure 6.2). The reanalysis shows the largest values of the skewness of the SST in the eastern Pacific, decreasing towards the west. The westward extension of the skewness is greatest along the equator and the South American coast. The multi-model ensemble (MME) skewness of the SST has a slight westward displacement of the large values of the skewness. This is most likely related to the westward displacement of the maximum ENSO variance in the coupled models. The overall structure of the maximum in the eastern Pacific which is continuously decreasing towards to the west along the equator is not present. Instead, both the central and eastern Pacific have local maxima with a minimum value approaching zero or slightly negative in between. Away from the coast, the positive values of the the skewness slowly decrease poleward. The decrease is faster in the central Pacific than in the eastern Pacific. The MME does not capture the slant of the decrease, leaving the skewness of the SST too zonally uniform. The model mean shows little change in the skewness of the SST between the different climate change scenarios and the pre-industrial control simulation. Given the theoretical results relating ENSO skewness and B, the failure to reproduce the SST skewness in the tropical Pacific and the poor simulation of B in the CMIP5 models could be related. This could also be related to the ENSO pattern bias and the model cold tongue bias and should be the subject of further study.

Using the theoretical and conceptual model results, the values of ENSO skewness are compared with the model values of B across the different climate change simulations. One and two standard deviation uncertainty intervals for a sample of 50 years are generated from a set of 10,000 year conceptual model simulations and shown in the darker and lighter gray shaded regions respectively (Figure 6.3). The models have a large spread in their simulated magnitude of multiplicative noise. This spread is also present in the models' simulation of ENSO skewness. The models' ENSO skewness is calculated by

taking the area averaged SST anomalies over a box from 5° S-5° N and of 50 ° longitude centered on the point on the equator which has the largest loading of the 1^{st} EOF of tropical Pacific SSTs. When the different RCP scenarios are examined, the multi-model ensemble estimations of B do not change significantly. However, due to the large spread between the models, the result that B does not change due to anthropogenic climate change is not particularly robust. On the whole, the CMIP5 models fit well within the theoretical prediction of the relationship of B and ENSO skewness. As has been previously shown, this figure clearly illustrates that the models have a tendency to both underestimate ENSO skewness and B.

6.3 The Relationship of ENSO Skewness to Extreme El Niño Events

The skewness of a distribution is important because it measures the ratio of width and symmetry of the tails of the distribution to the width of the center. In a positively skewed distribution, as is observed with ENSO, this means that there is a negative median value, a reduction in the large negative values, and an increase in the large positive values (Figure 6.4). Applying this to ENSO, the mean state has a slight negative anomaly, consistent with the lengthy recharge process (Kessler, 2002; Jin et al., 2007). Further, the positive tails of the SST anomaly distribution, exceed the expected number from a Gaussian distribution and there is a corresponding decrease in the small positive part of the distribution. This heavy positive tail is representative of the large number of extreme El Niño events that have occurred during the observational record. Given the impacts of extreme El Niño events, this tail is worthy of further examination.

For the purposes of this study, extreme El Niño events are defined as any event with a peak magnitude greater than 2.5 standard deviations, while regular events are defined with a peak magnitude greater than .5 standard deviations. As seen from the conceptual model, the frequency of occurrence of extreme events, defined as the number of extreme events divided by the total number of events, is strongly related to the

skewness (Figure 6.5). These results in the conceptual model are independent of the threshold non-linearity.

The extreme El Niño events are not just larger than the regular events, they also have a greater impact on the SST state in following years (Figure 6.6). In the reanalysis composite, these extreme El Niño events are followed by not just one year, but a second year of La Niña. This double-dip into La Niña is necessary for the further recharge of equatorial heat content that has been discharged during the El Niño event. The CMIP5 MME mean also shows a similar strong La Niña following an extreme El Niño event which does not occur for regular El Niño events. There is little difference in the strength of the average extreme El Niño events between the different emissions scenarios, consistent with the results that the mean skewness of ENSO in the models does not shift.

The extreme El Niño events in the CMIP5 models do not change in shape between the different emissions scenarios. In comparison with the reanalysis, the extreme El Niño representation in the models is reasonable (Figure 6.7). It captures the large zonal extent, although perhaps extending the warm anomalies too far to the west. The meridional extent of the warm anomalies is slightly reduced from reanalysis, but not hugely so. However, missing in the models is the strong warming in the extreme eastern Pacific that plays a major role in rainfall anomalies along the Pacific coast of South America and is a key defining portion of the traditional eastern Pacific El Niño.

It has already been shown that ENSO skewness is proportional to B. It is therefore not surprising that the frequency of occurrence of extreme El Niño events is also proportional to B (Figure 6.8). Due to event counting and sample size issues, the smaller the time period examined, the greater the uncertainty with the frequency of occurrence of extreme El Niño events with respect to B. However, the relationship for the skewness with the frequency of occurrence is much stronger. The frequency of occurrence is directly measured by the skewness, independent of the threshold non-linearity in the conceptual model. Therefore, while this analysis is consistent with the multiplicative noise framework, in order to simulate the frequency of extreme events correctly, it is only necessary to correctly simulate ENSO skewness.

Beyond the conceptual model, applying these results to the suite of CMIP5 models

and scenarios already examined produces similar results. There is a clear relationship between the models' simulation of B and the percentage of extreme El Niño events (Figure 6.9). Considering the event like nature, the inherent randomness of the samples and the length of the simulations, the fit is very good. As was previously found with the CMIP5 models' simulation of ENSO skewness, the frequency of occurrence of extreme El Niño events is likewise underestimated. Also, as was previously found, the frequency of occurrence of extreme El Niño events does not change in response to the different global warming scenarios considered. This differs from the results of Cai et al. (2014), but this difference is likely caused by a different metric (precipitation averaged over the Niño3 region) being used to define extreme El Niño events. Their metric is affected by changes in both the mean state and ENSO amplitude, while this one is not. As was found in the conceptual model, the fit is significantly improved when comparing model skewness to the frequency of extreme events ($r = 0.78$) (Figure 6.10).

6.4 Slow Noise Forcing and Extreme El Niño Event

Multiplicative noise has already been shown to decrease predictability of El Niño events compared with the additive noise case (Gebbie and Tziperman, 2009b,a; Levine and Jin, 2010). However, it has also been shown that the extreme El Niño events require a low-frequency component of the noise forcing (Levine and Jin, 2010). Furthermore, it has been shown earlier in this dissertation that multiplicative noise enhances the low-frequency component of the noise forcing. This can be seen in the conceptual model by comparing the frequency of El Niño events at different decorrelation timescales (Figure 6.11). The shorter the decorrelation timescale (the more even the energy distribution is among all frequencies), the longer the return period is between El Ni
no events. Additionally, multiplicative noise forcing decreases the return period particularly at shorter timescales. Therefore, the role of the low-frequency noise forcing of ENSO in producing extreme El Niño events will be further examined.

Starting with an examination of the 1997-98 El Niño, the event was preceded by a series of WWBs (McPhaden, 1999; McPhaden and Yu, 1999; Gebbie et al., 2007). The

WWBs can be identified as strong westerly wind anomalies in the pentad zonal wind anomalies (Figure 6.12). The WWBs can be seen to precede the SST anomalies intially in the central and later in the eastern Pacific. The high-frequency variability of the WWBs can similarly be found in the monthly zonal wind anomalies (Figure 6.13). The monthly anomalies show the low-frequency component of the noise forcing. Unlike the pentad anomalies, the monthly anomalies do not show increases and decreases of the noise forcing, but rather only show an increase in the growth phase of the El Niño event. This is the low frequency component of the noise forcing of ENSO, which has previously been shown to be more important in forcing ENSO (Roulston and Neelin, 2000; Levine and Jin, 2010).

Returning to the conceptual model, what has been seen in the 1997-8 El Niño event between the high and low frequency components of the noise forcing is typical. The high-frequency variability is superimposed upon a low-frequency envelope. This is important for forcing an El Niño event. During the El Niño growth phase, the low-frequency component of the noise, as seen by the monthly mean values, increases while the high-frequency variability is larger but both positive and negative. This can be more clearly seen by subtracting the monthly mean noise from the total noise to create a high frequency analog $\xi' = \xi - \bar{\xi}$. This shown over 5 different El Niño events (Figure 6.14). The high-frequency analog (ξ') has a mean of zero. The monthly mean noise captures the slow growth of the low frequency component which is key for forcing El Niño.

Multiplicative noise has been shown to increase the low-frequency component of the noise forcing. In order to examine the role of multiplicative noise (and the low frequency component of the noise more generally) in differentiating between regular and extreme El Niño events, the El Niño events are composited on the peak of El Niño. The differences between regular and extreme events begin to develop early in the evolution of the event. In regular events, the the noise grows slowly and inconsistently while the multiplicative component of the noise remains small. In extreme events, after the initial burst of noise, the noise component steadily grows. A few months before the peak of the event, the multiplicative noise component becomes very large. It is shown that as a fraction of the total noise forcing, the multiplicative component of the noise increases significantly

for the extreme events but does not for the moderate ones (Figure 6.15). Thus, the multiplicative component of the noise plays an integral role in producing an extreme El Niño event. The noise forcing and, in particular, its multiplicative component become negative ahead of the peak of the El Niño event and can contribute to the beginning of the transition of El Niño to La Niña along with other aspects of the transition like the annual cycle combination tones found by Stuecker et al. (2013) and the delayed negative feedbacks described by the delayed (Battisiti and Hirst, 1989; Suarez and Schopf, 1988) and recharge oscillators (Jin, 1997a).

The 1997-8 El Niño event also had an eastward propagation of the WWBs over the series of events (McPhaden, 1999; McPhaden and Yu, 1999). This is in agreement with other studies on multiplicative noise in coupled models (Gebbie et al., 2007; Gebbie and Tziperman, 2009b) and has been shown previously in this dissertation. Examining the Hovmuller diagrams of the composite extreme El Niño events shows the relationship between the low-frequency noise forcing and the creation of extreme El Niño events (Figure 6.16). The the zonal temperature advection (colors), total noise forcing (black contours), and total temperature (green contours) all precede the event and propagate eastward together. The zonal temperature advection is co-located with and to the east of the maximum noise forcing. The positive total noise forcing is located over warm waters of approximately $28^{\circ}C$ in the western and central Pacific ocean. Starting approximately seven or eight months prior to the peak of El Niño event, all three components, the total noise forcing, the zonal temperature advection, and the warm waters on the edge of the warm pool migrate in tandem slowly eastward. As the eastward migration occurs, the composite temperature advection and total noise forcing increase to a maximum 2-3 months before the peak of the El Niño event. Hovmuller diagrams of the extreme El Niño composites for all the CMIP5 models and scenarios used here can be found in Appendix C. Combining this information with the inclusion of a Heaviside function of ENSO amplitude as part of the shape of the multiplicative noise forcing of ENSO further emphasizes that the multiplicative noise forcing of ENSO is due to the eastward progression of warm pool edge and the corresponding eastward movement of convection in the build up to an El Niño event.

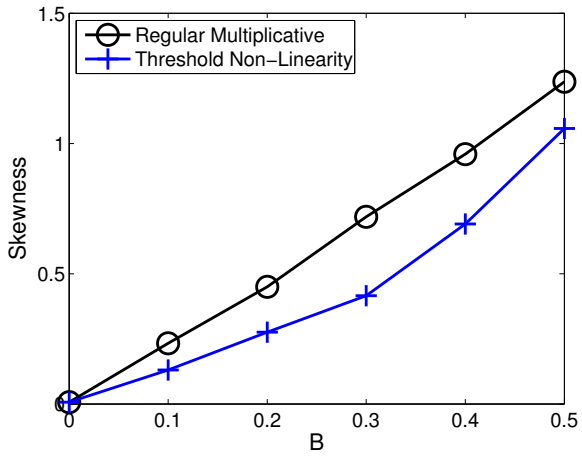

Figure 6.1: The skewness of the conceptual model as a function of B from 50,000 years of simulation. The skewness is linearly related to B when regular multiplicative noise is considered and non-linearly when multiplicative noise with a threshold non-linearity is considered.

6.5 Summary

Multiplicative noise forcing has impacts on the general ENSO properties, such as skewness and extreme events. In particular, these extreme events increase in frequency of occurrence with an increase in B. This is due to an increase in the slow noise component from the inclusion of multiplicative noise. The slow frequency component of the noise has been previously shown to be responsible for triggering El Niño events, while the high frequency component is unable to trigger El Niño events in isolation (Roulston and Neelin, 2000; Levine and Jin, 2010). This low frequency component of the noise corresponds to the coupled eastward propagation of the western Pacific warm pool and the westerly wind bursts. The series of westerly wind bursts that occurred prior to the 1997-8 El Niño event is shown to be a characteristic of extreme El Niño events and is related back to the low frequency component of the noise forcing.

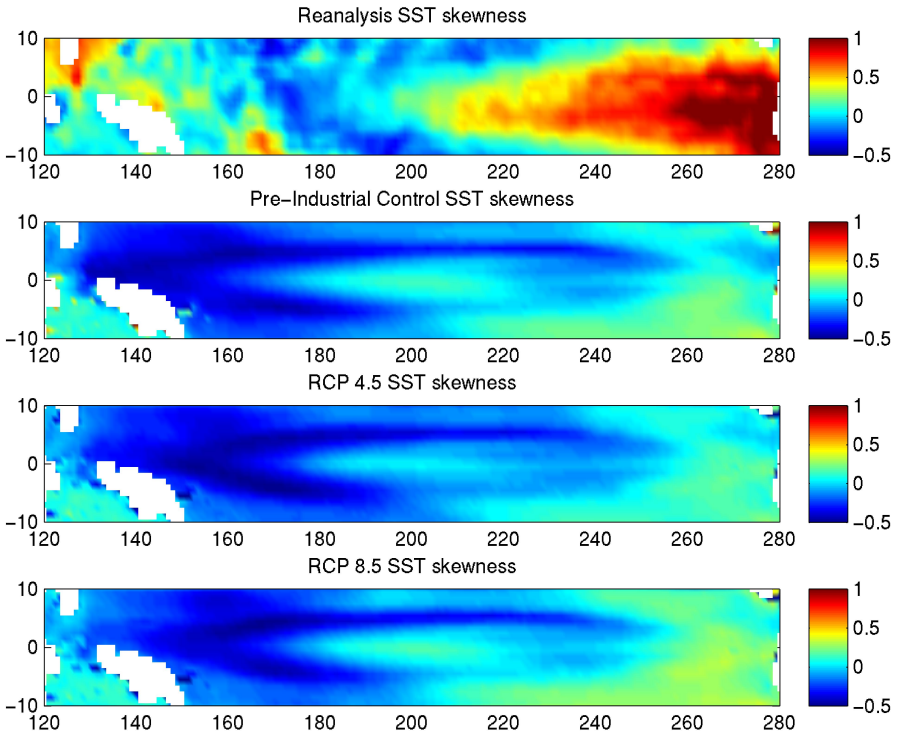

Figure 6.2: The skewness of the SST anomaly for a) reanalysis and CMIP MME for b) Pre-Industrial Control c) RCP 4.5, and d) RCP 8.5. None of the MMEs correctly capture SST anomaly assymetry in the equatorial regions.

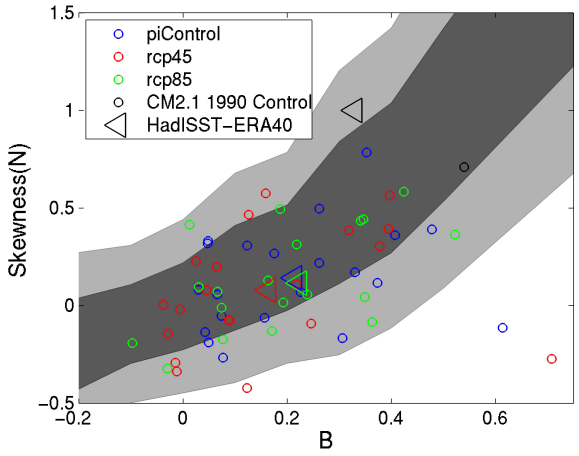

Figure 6.3: CMIP5 models simulation of the relationship between state dependence, B, and skewness of the model defined Nino box. Most models fail to adequately simulate the state-dependence. There is also a large amount of variability between the models and little variability between the different emissions scenarios.

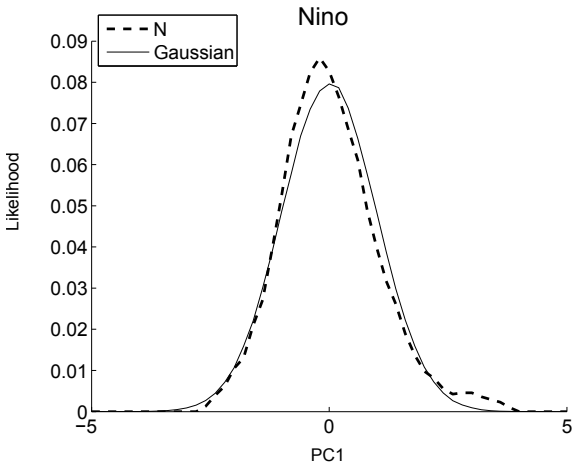

Figure 6.4: The difference between a skewed distribution and a normal distribution as demonstrated using the reanalysis PC1 normalized histogram. The skewed normalized histogram has a negative median and fatter positive tail than the normal distribution.

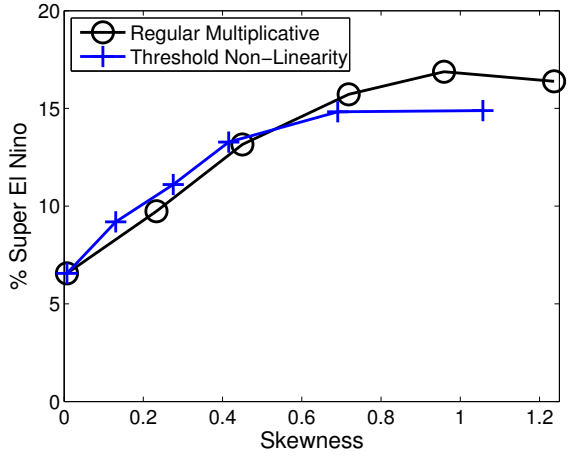

Figure 6.5: The percentage extreme ($T > 2.5\sigma(T)$) El Niño events of the total ($T > 0.5\sigma(T)$) El Niño events as a function of the skewness in a 50,000 year simulation of the conceptual model for different values of B. There is a clear relationship between the skewness and frequency of occurrence of extreme El Niño events until the percentage of extreme events saturates.

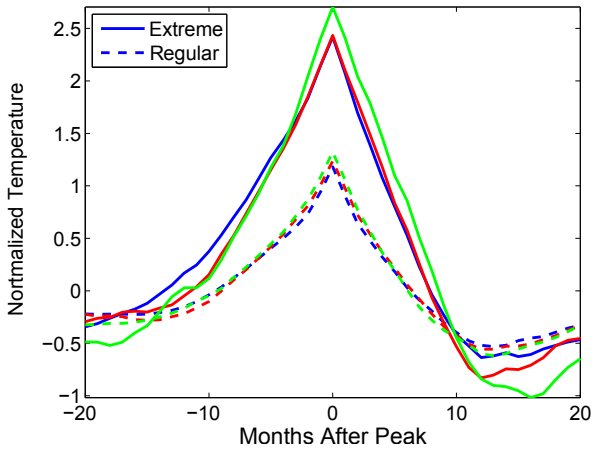

Figure 6.6: The MME composite regular and extreme El Niño events for the Pre-Industrial Control (blue), RCP4.5 (red), and RCP 8.5 (green). The extreme El Niño events tend to be followed by a long-lasting La Niña, which is different than the regular El Niño events.

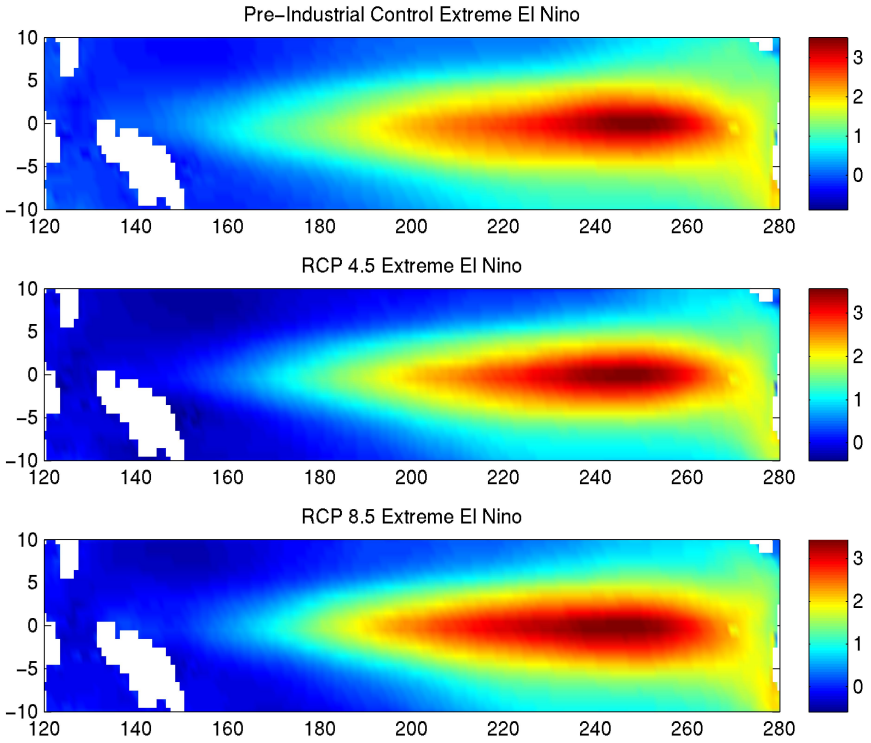

Figure 6.7: The MME composite extreme El Niño events. The extreme El Niño events have maxima in the eastern Pacific, although the tend to miss the large anomalous SSTs along the western coast of South America.

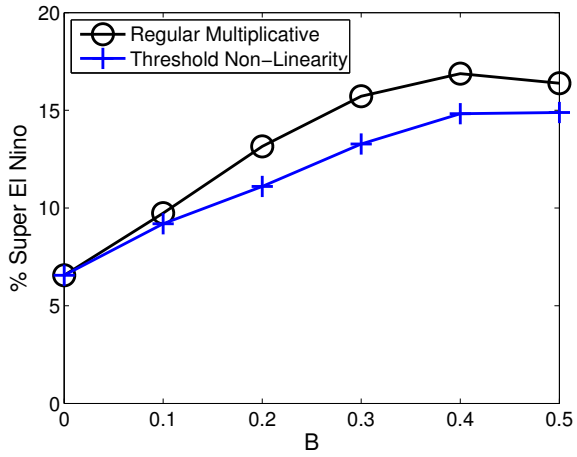

Figure 6.8: The percentage extreme ($T > 2.5\sigma(T)$) El Niño events of the total ($T > 0.5\sigma(T)$) El Niño events as a function of B in a 50,000 year simulation of the conceptual model for different values of B. Similar to skewness, there is a relationship between frequency of occurrence of extreme El Niño events and B.

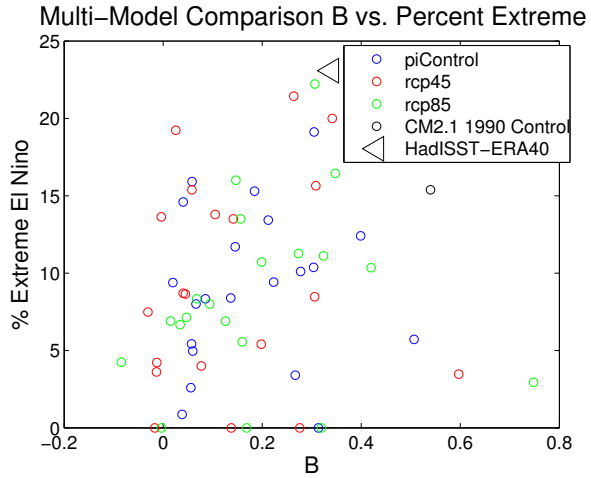

Figure 6.9: The percentage extreme ($T > 2.5\sigma(T)$) El Niño events of the total ($T > 0.5\sigma(T)$) El Niño events as a function of B in the CMIP5 models. The relationship between frequency of occurrence of extreme El Niño events an B is weaker because of too short simulations to get accurate statistics on extreme event frequency.

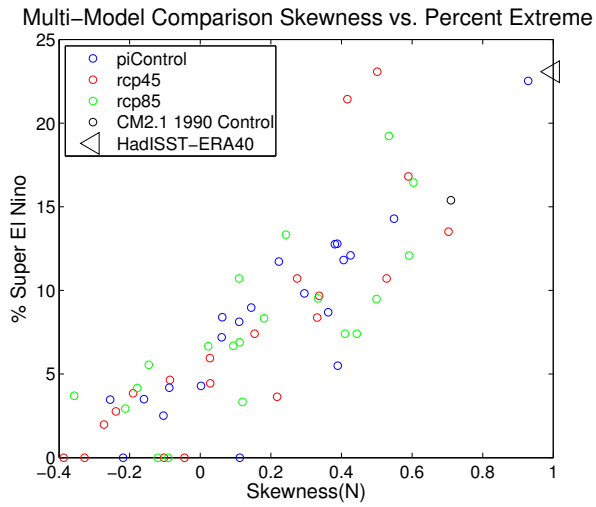

Figure 6.10: The percentage extreme ($T > 2.5\sigma(T)$) El Niño events of the total ($T > .5\sigma(T)$) El Niño events as a function of the skewness in the CMIP5 models ($r = 0.78$). Like the conceptual model, there is a good relationship of frequency of occurrence of extreme El Niño events to skewness.

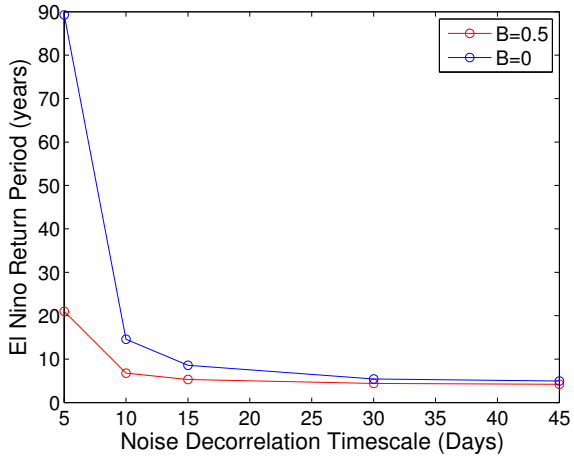

Figure 6.11: The return period of El Niño events in the conceptual model for different noise decorrelation timescales. The return period increases as the decorrelation timescale decreases. This shows the importance of the low frequency component of the noise forcing.

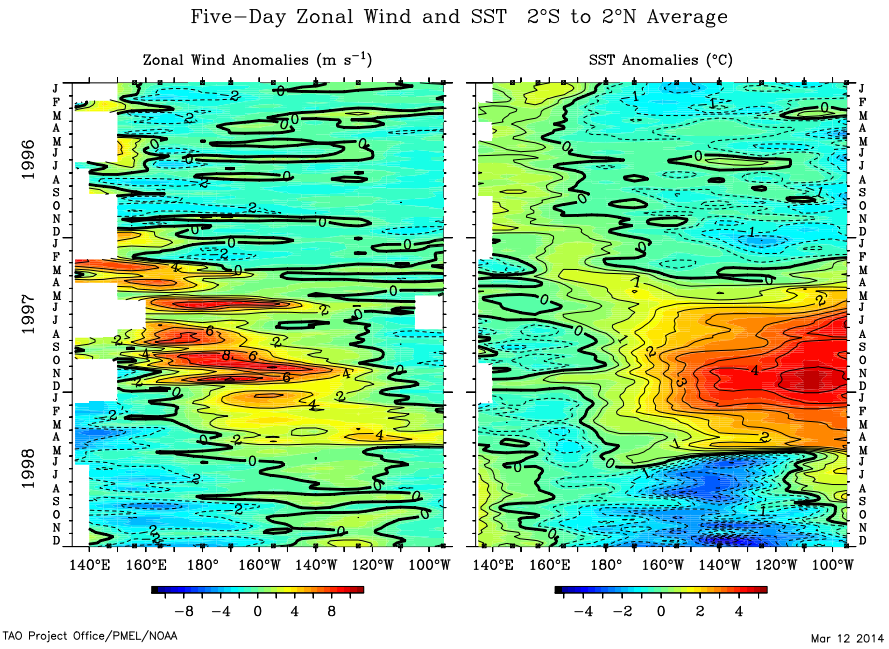

Figure 6.12: The zonal wind and SST anomalies averaged over 5-days from 1996-8. There are both positive and negative windstress anomalies that occur in the pentad windstress field. From NOAA PMEL.

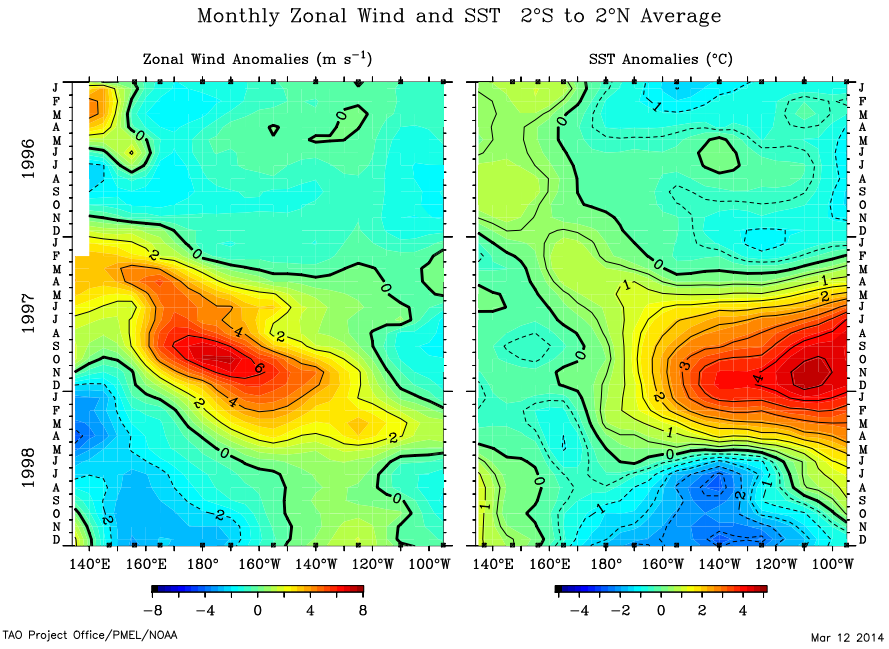

Figure 6.13: The zonal wind and SST monthly anomalies from 1996-8. Unlike the pentad windstress field, the anomalies from the monthly mean are consistently positive in the growth phase of El Niño. From NOAA PMEL.

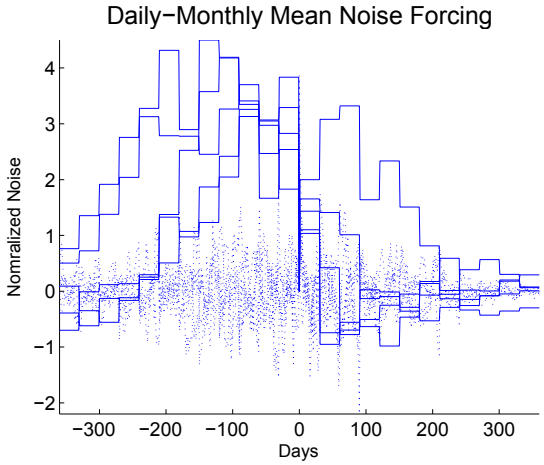

Figure 6.14: El Niño composites for 5 El Niño events showing the difference of the daily and monthly mean forcing values (dotted lines) and monthly mean forcing values (solid lines). The monthly values capture the low frequency modulation of the noise, which is what is necessary for the forcing of an El Niño event.

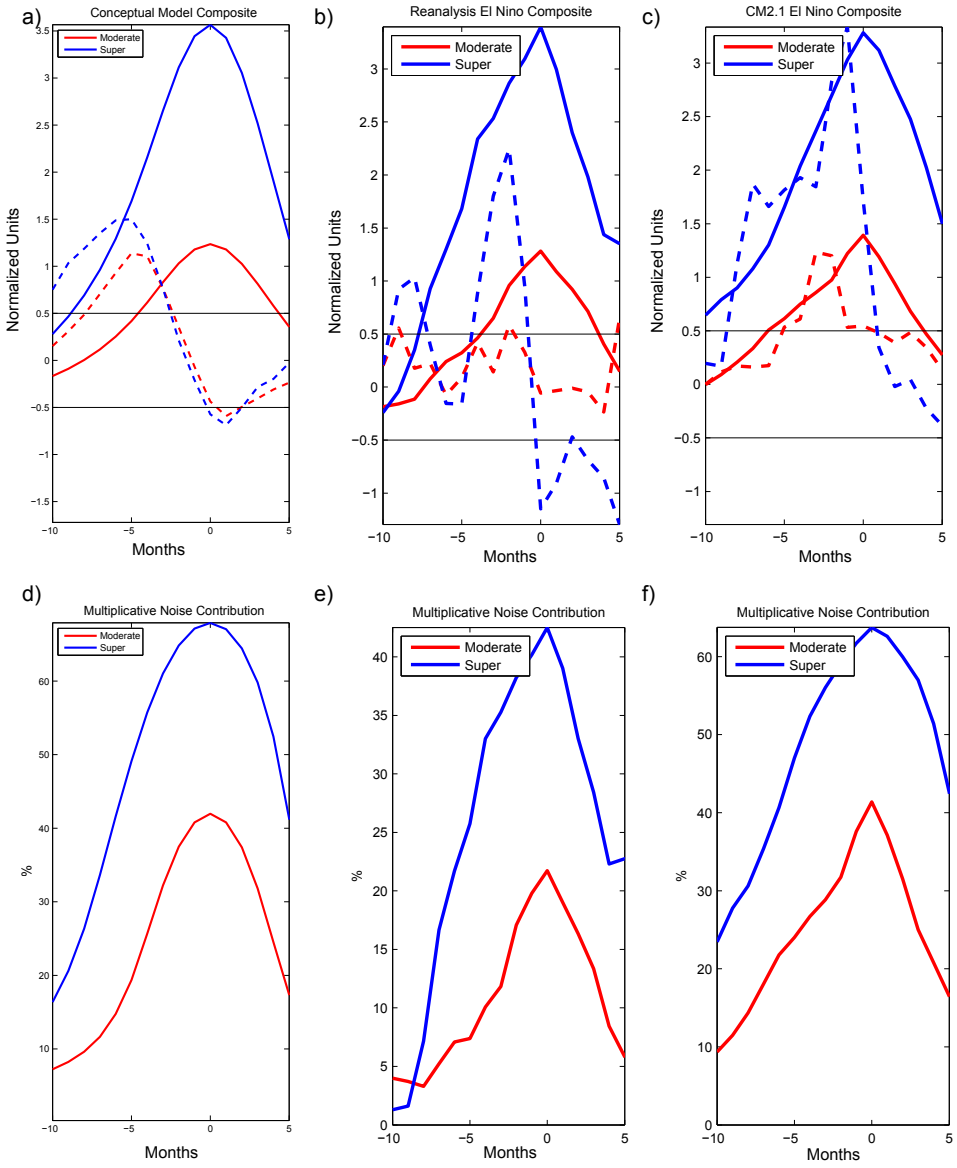

Figure 6.15: Composites of moderate ($T > .5\sigma(T)$) and extreme ($T > 2.5\sigma(T)$) El Niño events of the total noise forcing and percentage multiplicative noise forcing for (a,d) conceptual model $B = 0$ and $B = 0.5$, (b,e) reanalysis, and (c,f) CM2.1. In (a-c) the solid lines are the El Niño composite and the dashed lines are the R_τ composite. Multiplicative noise plays a larger role in forcing extreme events than regular ones.

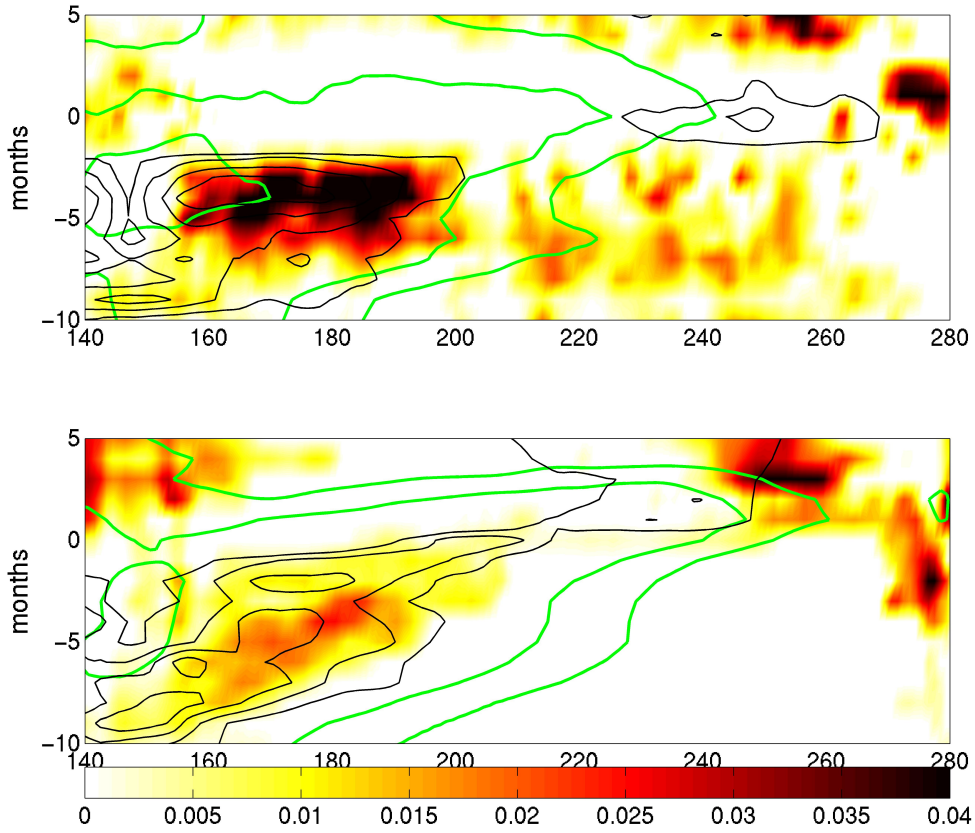

Figure 6.16: Composite Hovmoeller diagrams of the extreme ($T > 2.5\sigma(T)$) El Niño events of the total noise forcing, zonal temperature advection, the SST, and, SST anomaly for (a) reanalysis, and (b) CM2.1. The complete set of multiplicative noise physical processes (as outlined in Chapter 4) occur in the months leading up to an extreme El Niño event.

Chapter 7

Conclusion

7.1 Key Points

This dissertation has presented a new method for diagnosing the magnitude of the state-dependence and the intensity of the noise forcing of ENSO. This method has been applied to the equatorial zonal windstress in reanalysis and coupled climate models. Using the reanalysis and two of the coupled climate models, the physical processes of the windstress multiplicative noise were explored. An anomalous westerly windstress is found to expand the warm pool, promoting convection further to the east in the equatorial Pacific. This eastward shift of the convection can enhance the future westerly wind anomalies creating a positive feedback. This positive feedback is shown to then affect the ENSO skewness and extreme El Niño events. In general, it was found that the CMIP5 models underestimate the strength of this feedback compared to observations.

7.2 Summary and Discussion

The multiplicative noise forcing of ENSO plays a key role in ENSO asymmetry and extreme El Niño events. These extreme events have very large societal impacts, yet it is still poorly understood what causes one El Niño event to become a normal event while another event to become an extreme event. Here, it is shown that a key contributor

to these extreme events is multiplicative noise. The dynamics of the oceans and the atmosphere contribute to increasing the strength of the forcing and to reddening of the wind stress spectrum, which are important for the cascade of energy from higher frequencies to lower ones and transferring energy from WWBs, including MJO events, to ENSO.

Previous attempts at characterizing multiplicative noise forcing of ENSO have treated the WWBs as function of many parameters to fully describe them over time and space (Eisenman et al., 2005; Gebbie et al., 2007; Gebbie and Tziperman, 2009b,a; Lopez et al., 2013; Lopez and Kirtman, 2013). They have assumed numerous properties such as Gaussanity in space and time or being more deterministic in nature during the development of an El Niño event. I have developed a systematic approach starting from a simple conceptual model to focus on two parameters of the system, namely, the intensity, σ, and the magnitude of the state-dependence, B, of ENSO noise forcing. Furthermore, the conceptual model has allowed for the development and testing of simple methods to estimate the ENSO noise forcing and these parameters. By applying this methodology, the magnitude of the state dependence and the intensity of the ENSO noise forcing from reanalysis and coupled climate models can be more simply estimated.

Another major strength of this approach is its use of monthly mean values of wind stress and SST in determining the magnitude of the state dependence factor. This allows the method to be easily applied to coupled GCM simulations from which the daily output is significantly more cumbersome to use. This is in contrast to the method of estimation from Kug et al. (2008). Also, in contrast to their method of estimation, the method presented in this dissertation does not use spectral filtering to isolate the noise component. As has been shown by many previous studies, including Roulston and Neelin (2000) and Levine and Jin (2010), the high frequency component of noise forcing is unable to effectively force ENSO. Filtering for the high frequency noise removes the low frequency component of the noise forcing that is so important to force ENSO. By eliminating this component of the forcing, some of the signal is potentially missed. It has been further demonstrated in this dissertation the extent to which the high-frequency variability is not responsible for the creation of El Niño events and in particular the

extreme events.

With the conceptual model, the methodology can be tested for its resiliency to various different assumptions. By comparing the difference between the conceptual model with daily output and only monthly output, it is clear that the low frequency noise is the important component. This is what allows the methodology to use monthly mean data. Further, the effect of the length of the time series on the estimation of the magnitude of state-dependent factor can be can be tested. This method is relatively accurate over time lengths of 50 years allowing it to be applied to reanalysis products of those lengths.

This method produces an estimate of $B = 0.29 \pm 0.14$ which is within the range of the estimate from Kug et al. (2008) of $B = 0.1 - 0.5$. The importance of having a correct value for B was shown in Jin et al. (2007) and Levine and Jin (2010). Both of these studies showed that as B increases so does the ENSO growth rate. Levine and Jin (2010) further showed that as B increases, there are more super El Niños and the predictability of ENSO decreases.

Both GFDL-CM2.1 and CCSM4 model simulations were examined in depth and found to significantly over estimate the strength of the state-dependence of multiplicative noise of zonal wind on SST (CM2.1 has $B = 0.54$ and CCSM4 has $B = 0.89$) with respect to reanalysis despite the fact that the last 50 years includes extremely active ENSO periods. It has previously been noted that both of these models generate overly active and highly non-linear ENSO variaiblity (Wittenberg, 2009; Deser et al., 2012). Jin et al. (2007) and Levine and Jin (2010) both showed that increases in B cause increases in ENSO growth rate, potentially forcing a stable oscillatory regime to become unstable, requiring non-linear controls to prevent runaway El Niño states in their conceptual models. While additional processes in coupled models preclude these runaway states in the GCMs, this could potentially be an important factor in both the overly large and multi-year El Niño events simulated by these GCMs. Moreover, both models show significant amounts of multi-decadal scale ENSO variability (Wittenberg, 2009; Deser et al., 2012). How related this longer time scale variability is to these larger values of multiplicative state-dependence, whether cause or effect, is still to be determined, but the potential for increased variability due to the amplifying effect of multiplicative noise forcing can not

be ignored.

Additionally, this study shows that the strong state-dependent windstress noise forcing for ENSO occurs along the warm pool edge. This region has already been the target of numerous studies examining the relationship of westerly wind bursts to ENSO. The results shown here are consistent with the findings of changes in westerly wind burst properties in the western Pacific in the growth phase of ENSO with those found by Harrison and Chiodi (2009). The importance of this region and the threshold non-linearity found as part of the state-dependence further emphasizes the potential importance of convection and the role of the warm pool in forcing ENSO.

While the 50-year time frame of the reanalysis data leaves a large uncertainty in the structure of the existence of the threshold non-linearity, the GCMs with much longer data lengths give robust results. CM2.1 unambiguously shows the threshold non-linearity in the multiplicative noise forcing, while CCSM4 shows a slightly more complicated pattern suggesting that the threshold non-linearity exists not at $T = 0$, but at a different value of T. However, this difference does little to affect the overall impacts of multiplicative noise on ENSO and is similar to shifting the region of windstress anomaly being examined. The threshold non-linearity was not accounted for previously by Kug et al. (2008). The inclusion of a threshold non-linearity suggests an important role for atmospheric convection in shaping this feedback. This fits with other studies on multiplicative noise forcing of ENSO which have discussed the role of convection as a key physical process for multiplicative noise. The coupling of the ocean state and the windstress forcing are also consistent with many previous studies on multiplicative noise forcing of ENSO which have found a eastward propagation of the western Pacific warm pool and the westerly wind bursts as key processes within the multiplicative noise framework (Lengaigne et al., 2004; Eisenman et al., 2005; Gebbie et al., 2007).

Additionally, by showing the role of atmospheric convection and the threshold non-linearity within the multiplicative noise forcing, it is clear that simply using linear regressions may result in an overemphasis of the symmetric response to both warming and cooling when estimating properties of ENSO. The challenges of accounting for the non-linear responses in examining ENSO, using tools like the Bjerknes Instability Index

(Jin et al., 2006; Kim and Jin, 2011a,b), has been noted (Graham et al., 2014). ENSO noise forcing may be part of the solution to these errors. Additionally, the non-linearity of the precipitation response to ENSO has been examined as a method for determining the extreme El Niño events (Cai et al., 2014) and in future projections of the effect of global warming on changing ENSO teleconnections (Power et al., 2013).

Due to the asymmetric response of the multiplicative noise to ENSO state, the physical processes involved in producing multiplicative noise are investigated using composites. The composites of additive and multiplicative noise are analyzed and shown to be similar to the WWBs characterized both from observations and modeling studies (Kleeman and Moore, 1997; Moore and Kleeman, 1999; Yu et al., 2003; Tziperman and Yu, 2007).

These extreme noise forcing events of El Niño have a similar spatial pattern to other westerly wind bursts (Tziperman and Yu, 2007). The major difference between the large noise forcing events and the extreme ones are that the extreme noise forcing events are not isolated but have a strong low-frequency contribution. These extreme events have preceding large noise events which prime the ocean, by forcing zonal advection of the western Pacific warm pool, for the creation of the extreme events. This is in agreement with Gebbie and Tziperman (2009b). This priming of the ocean can be represented as multiplicative noise. Separating the total noise forcing into multiplicative and additive components, it is shown that the multiplicative noise is responsible for the creation of most of the extreme noise forcing events.

Further, it is shown that organized anomalous precipitation in the region occurs contemporaneously with the eastward march of the westerly wind anomalies and the eastward progression of the warm pool edge. The anomalous precipitation connects the oceanic response to the westerly wind anomalies and the future westerly wind anomalies which are the critical atmospheric manifestation of multiplicative noise. A westerly wind event creates positive zonal temperature advection, expanding the western Pacific warm pool. The expanded warm pool supports additional convection further to the east. The difference in eastward extent of the additional westerly wind forcing between the reanalysis and CM2.1 and CCSM4 could therefore be explained by the exisitence of the coupled model cold tongue bias preventing convection from forming further to the east.

Continuing the cycle, if the convection forms further to the east, additional westerly wind anomalies occur due to convergence. These new westerly wind anomalies expand the warm pool further to east, allowing for more eastward propagation of the convection. This is in agreement with previous studies on multiplicative noise (Lengaigne et al., 2004; Eisenman et al., 2005; Gebbie and Tziperman, 2009b). The positive feedback loop is then broken by the delayed response of the thermocline and the limited resource of ocean heat content which eventually outcrops cooler waters at the outset of La Niña and changes in the background state due to the annual cycle.

The distinction between additive and multiplicative noise is that for additive noise, each noise event is independent of the background state, while in the case of multiplicative noise, each noise event contains a dependence on the state of the system which itself can be altered by noise events. In the ENSO system, the noise, WWBs, can create a positive feedback loop where one WWB creates conditions such that a second burst is more likely (Gebbie and Tziperman, 2009b). From this analysis, it becomes evident not just in the initial event but also in the largest events. When composited, the largest events show a strengthening through time. Months prior to the peak windstress forcing event, an initial windstress event occurs of normal strength. The initial oceanic response to windstress produces an expansion of the warm pool to the east. Without another WWB, the warm water anomaly dissipates returning the warm pool edge to its pre-WWB location. However, if another WWB happens while the warm pool is expanded eastward, the WWB gets enhanced by the previously forced changes to the underlying SSTs and progresses further eastward. Both the enhancement of the westerly wind event and the propagation of the event further to the east are responsible for increased El Niño forcing.

Additionally, this new WWB further expands the warm pool to the east allowing for a repetition of the process. In this way, the largest westerly wind events have a tendency to be preceded by smaller westerly wind events, successively increasing in magnitude and migrating eastward over time. This low-frequency modulation of the noise forcing is important to the cascade of energy from the high-frequencies to the low-frequencies and has been shown to be vital to the creation of El Niño events and explicitly to the

occurrence of extreme El Niños. The increase in system memory that drives the largest westerly wind events is well explained by the multiplicative noise driven aspect of the conceptual ENSO oscillator hypothesis. The initial trigger for an ENSO event begins to create the conditions for additional forcing events of ENSO to occur. If the additional forcing does not occur, a small El Niño event takes place. However, every additional forcing event that occurs increases the strength of the growing El Niño and improves the effectiveness of future forcing events such that El Niño can be forced to grow larger and larger much like was seen during the 1997-8 El Niño event (McPhaden, 1999; Gebbie and Tziperman, 2009b).

Much like previous work on the impacts of SSTs in creating red noise atmospheric forcing (Frankignoul and Hasselmann, 1977), the coupling between the ocean and the atmosphere is important for the low-frequency modulation of the noise forcing of ENSO achieved by the multiplicative noise. In atmosphere only experiments forced by different SST anomalies, the low frequency component of the noise forcing is reduced over the coupled simulation. In these situations, a new peak in the spectrum of the noise forcing occurs at the low-end of the ENSO spectrum. This peak is similar to what exists when a smoothed ENSO signal is used to remove the ENSO signal from the windstress. There is a deficit of energy in the semi-annual to inter-annual energy bands in these experiments that results in the lack of coupling and its role in facilitating the multiplicative noise process.

The state-dependent low-frequency noise forcing of ENSO is important for the simulation of extreme El Niño events, as previously shown by prevous studies (Levine and Jin, 2010) and in the conceptual model. These extreme El Niño events are responsible for large amounts of damage and significant weather anomalies in many parts of the world. These extreme El Niño events, however, only happen occasionally, with three in the last 50 years and potentially fewer per 50 years over the previous millennium from paleoclimate reconstructions (Conroy et al., 2008). In a future climate, the current climate ENSO SST anomalies create larger societal impacts than are currently experienced (Power et al., 2013). Additionally, there is a suggestion that the societal impacts could be even larger than would be created by a simple addition of the projected tropical

warming to the current ENSO record (Cai et al., 2014). Here, a potential mechanism for the creation of these extreme El Niño events has been examined. It has been shown that the extreme events can be related to multiplicative stochastic noise forcing.

Looking at the CMIP5 model simulations across three different scenarios, the relationship between the strength of the state-dependence of multiplicative noise, B, the overall ENSO skewness, and the frequency of extreme El Niño events matches well with the prediction of a conceptual model El Niño model. It is observed that as the state-dependence increases, so too does the ENSO skewness and the frequency of extreme El Niño events. However, it is also shown that the current generation of coupled climate models does a poor job at simulating the processes involved in multiplicative noise. As these are related to convection along the warm pool edge, it is not surprising that the cold tongue bias and the location of the ITCZ are found to play a role in the poor model simulation of this process and the under-representation of ENSO skewness among the coupled climate models.

While the significant spread of the model simulations of multiplicative noise make it difficult to make a projection for the change in the magnitude of multiplicative noise forcing of ENSO or ENSO skewness due to climate change, the relationship of the spatial patterns of precipitation and temperature anomalies can provide some potential information. Positive changes in B are positively correlated with decreases in east-west SST gradient in the equatorial Pacific. These changes are also positively correlated with increased precipitation in the eastern Pacific. The meridional precipitation contrast in the eastern Pacific is anti-correlated with B, which is consistent with the findings of Merkel et al. (2010) and Watanabe et al. (2011) on the relationship of precipitation and ENSO amplitude. This result is opposite to the correlation between B and the total precipitation. Additionally, there is also a relationship between B and total precipitation that is likely due to the impact of the cold tongue bias. Whereas, the change in meridional precipitation contrast, in conjunction with the wet get wetter hypothesis (Xie et al., 2010), and the reduction of the east-west SST gradient all suggest an increase in ENSO skewness in response to global warming in agreement with the results from Cai et al. (2014).

7.3 Future Work

The ability to quantify the state-dependent factor of multiplicative noise points to new directions of study. ENSO variability has been shown to be large in observations and unforced climate control runs (Wittenberg, 2009; Cobb et al., 2013; Ogata et al., 2013). Many attempts have been made to explain this as interaction of ENSO and the mean climate state, which modifies the dominant positive and negative feedbacks of ENSO and the relative importance of thermocline processes and SST-advection. In a simplified model framework, Jin and Neelin (1993b,a) and Neelin and Jin (1993) found that these processes coexist over a wide range of realisitic parameters. The relative dominance between these two processes is sensitive to the chosen values of the parameters. Fedorov and Philander (2000, 2001) translated these parameters to changes in the mean state of the tropical Pacific. They found that the observed changes in the tropical Pacific mean state across the 1970s Pacific climate shift could account for the changes observed in ENSO over the same period of time. Bejarano and Jin (2008) further examined changes to ENSO amplitude and frequency, showing that ENSO had two dominate modes with periods of approximately 2 and 4 years matching with the different types of variability obsreved by Jin and Neelin (1993b). The dominant mode was found to be sensitive to small changes in ocean mean state. Of these physical processes, the central Pacific El Niño is more dominated by SST-advection processes than by thermocline processes and thus is less affected by the state-dependent westerly wind bursts than the eastern Pacific El Niños (Harrison and Chiodi, 2009; Ren and Jin, 2013; Lopez and Kirtman, 2013). The relationship between multiplicative noise forcing and the different types of ENSO must be further explored.

The spreading of the western Pacific warm pool in response to westerly wind bursts has been noticed in observations (McPhaden et al., 1988) and simulated in coupled climate models (Lengaigne et al., 2004; Lopez et al., 2013). Harrison and Chiodi (2009) found that there were changes in the westerly wind burst location and strength of the anomalous easterlies converging with the westerly wind burst over the last few decades, which were related to the differences El Niño over the multidecadal observed period.

Similarly, Lopez and Kirtman (2013) found that the state-dependent component of the westerly wind bursts was more important for eastern Pacific type El Niño events than for central Pacific ones in a single climate model, due to the impact of state-dependent westerly wind bursts on the thermocline. The process that has been outlined here has shown the impact of advection of the warm poool for creating the multiplicative component of the forcing. Given the effects of noise on ENSO diversity found by Lopez and Kirtman (2013) and its relationship to multiplicative noise forcing, it is possible that the recent trends in ENSO differences, the well documented changes in ENSO amplitude between the period of 1976-1998 and 1999-current as well as changes in its location of maximum SST anomaly, from central Pacific El Niño to eastern Pacific El Niño, are purely noise driven as opposed to a physical mode of multidecadal scale variability. To what extent is the multiplicative noise forcing component important in differentiating between these two ENSO flavors.

An aspect of additional complexity that was ignored in this work is the annual cycle of WWBs. In agreement with Harrison and Chiodi (2009), large noise forcing events are found to happen less frequently in the boreal summer months (Figure 7.1). How this modulation of the WWB timing might effect ENSO should be further explored in the conceptual model. Another effect that needs to be explored in conjunction with the annual cycle of WWBs is the role of the annual cycle of ENSO growth rate. The interaction of these two different annual cycles with multiplicative noise needs to be explored in greater detail.

In this dissertation, the role of multiplicative noise in creating extreme El Niño events is explored. The low-frequency component of the noise manifests as an increase in the noise forcing during the growth phase of El Niño. This has implications for the predictability of El Niño. These implications for predictability need to be further explored in the conceptual model, reanalysis, and coupled climate models. In particular, greater attention should be paid to the frequency with which El Ni no and extreme El Niño events occur in the months following various size westerly wind events. This can help quantify the uncertainty in El Niño prediction.

In terms of broader impacts, beyond a better understanding of ENSO and ENSO

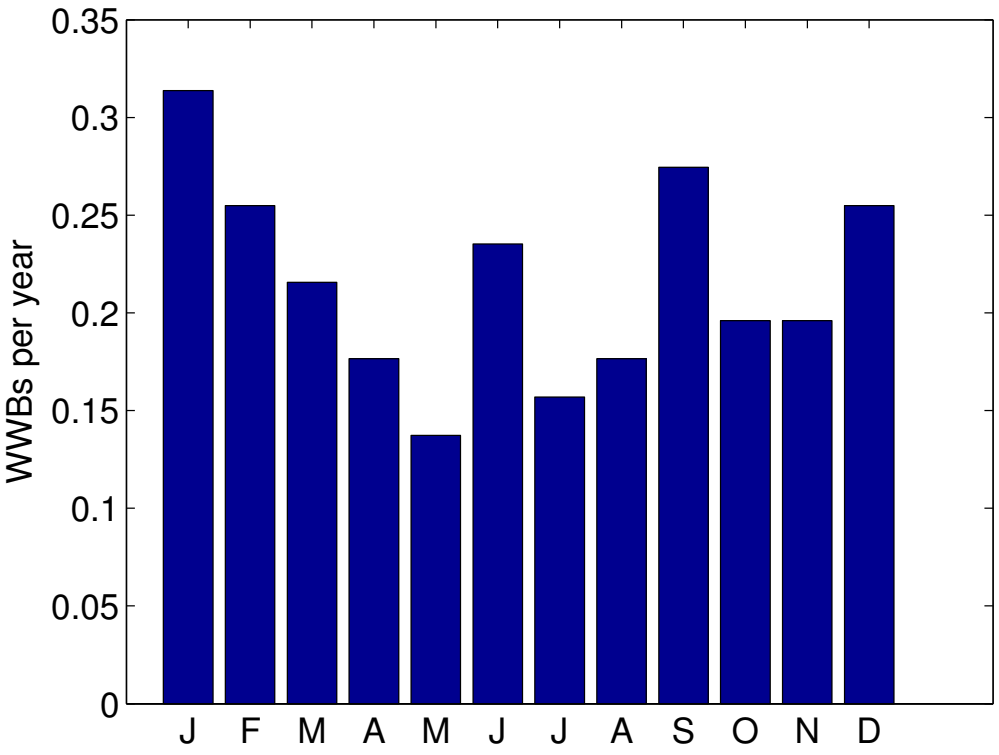

Figure 7.1: The average number of low frequency westerly wind events ($R_\tau > \sigma(R_\tau)$) per year by month for the Reanalysis. There is a weak seasonal cycle to the observed distribution of these events, with a minimum in boreal summer.

interactions, the question can be asked if there are other multiplicative systems in the climate system and if so, can the methodology developed here be used to help estimate the state dependence of those systems to increase our understanding and ability to simulate these systems.

Appendix A

Derivation of Analytical Solution to the Skewness

Starting from the second and third order terms in Levine and Jin (2010), we can add additional equations to solve analytically for the skewness, $S = \frac{T'^3}{(T'^2)^{\frac{3}{2}}}$. This is derived from Jin (personal communication).

$$\begin{aligned}
\frac{d < T'^2 >}{dt} &= -2\lambda < T'^2 > +2\omega < h'T' > +2\sigma(1 + B < T >) < \xi T' > \\
&\quad + 2\sigma B < \xi T'^2 > \\
\frac{d < h'^2 >}{dt} &= -2\omega < h'T' > \\
\frac{d < h'T' >}{dt} &= -\lambda < h'T' > +\omega(< h'^2 > - < T'^2 >) + \sigma(1 + B < T >) < \xi h' > \\
&\quad + 2\sigma B < \xi h'T' >
\end{aligned} \tag{A.1}$$

By multiplying $\frac{1}{3}T\frac{d<T'^2>}{dt}$ the equation for the third moment evolution of the temperature is found

$$\begin{aligned}
\frac{d < T'^3 >}{dt} &= -6\lambda < T'^3 > +6\omega < h'T'^2 > +6\sigma(1 + B < T >) < \xi T'^2 > \\
&\quad + 6\sigma B < \xi T'^3 >
\end{aligned} \tag{A.2}$$

Similarly, by multiplying $\frac{1}{3}h\frac{d<h'^2>}{dt}$ the equation for the third moment evolution heat content is found

$$\frac{d<h'^3>}{dt} = -2\omega < h'^2T' > \tag{A.3}$$

Finally, the mixed term $\frac{d<h'T'^2>}{dt}$ is solved for by multiplying $h*\frac{d<T'^2>}{dt}+\frac{1}{2}T*\frac{d<h'T'>}{dt}$

$$\begin{aligned}\frac{d<h'T'^2>}{dt} &= -2\lambda < h'T'^2 > +2\omega < h'^2T' + 2\sigma(1+B<T>) < \xi h'T' > \\ &- 2\lambda < h'T'^2 > +2\omega(< h'^2T' > - < T'^3 >) \\ &+ 2\sigma(1+B<T>) < \xi h'T' > +4\sigma B < \xi h'T'^2 >\end{aligned} \tag{A.4}$$

which simplifies to:

$$\begin{aligned}\frac{d<h'T'^2>}{dt} &= -4\lambda < h'T'^2 > -2\omega < T'^3 > +4\omega < h'^2T' > \\ &+ 4\sigma(1+B<T>) < \xi h'T' > +4\sigma B < \xi h'T'^2 >\end{aligned} \tag{A.5}$$

By assuming steady state, $\frac{d}{dt} = 0$, so from equation (3)

$$< h'^2T' >= 0 \tag{A.6}$$

Substituting into equation (5) and assuming fourth order closure condition, $< \xi h'T'^2 >= 0$ and that $< \xi h'T' >= 0$

$$0 = -4\lambda < h'T'^2 > -2\omega < T'^3 > \tag{A.7}$$

$$< h'T'^2 >= \frac{-\omega}{2\lambda} < T'^3 > \tag{A.8}$$

Substituting into equation (2)

$$0 = -6\lambda < T'^3 > -6\omega\frac{\omega}{2\lambda} < T'^3 > +6\sigma B < \xi T'^3 > +6\sigma B < \xi T'^2 > \tag{A.9}$$

which yields

$$< T'^3 >= \frac{\sigma B < \xi T'^3 > +\sigma < \xi T'^2 >}{\lambda^2 + \frac{1}{2}\omega^2} \tag{A.10}$$

Returning to Levine and Jin (2010), we find that

$$\frac{d<\xi T'^2>}{dt} = -(2\lambda + r) < \xi T'^2 > +2\omega < \xi h' T' > \\ + 2\sigma(1 + B < T >) < \xi^2 T' > -2\sigma B(\xi^2 T'^2 - < \xi T' >^2) \tag{A.11}$$

Again assuming steady state, $r >> \lambda$ and closure conditions $< \xi h' T' >= 0$, $< \xi T' >^2 = 0$, and $< \xi^2 T'^2 >= 2a < T'^2 >$

$$0 = -r < \xi T'^2 > +2\sigma < \xi^2 T' > -4\sigma B a < T'^2 > \tag{A.12}$$

which yields

$$< \xi T'^2 >= \frac{2\sigma}{r}(< \xi^2 T' > -2Ba < T'^2 >) \tag{A.13}$$

From Levine and Jin (2010),

$$\frac{d<\xi^2 T'>}{dt} = -(\lambda + 2r) < \xi^2 T' > +\omega < \xi^2 h' > +\sigma B < \xi^3 T' > \tag{A.14}$$

Again assuming steady state, $r >> \lambda$ and that closure conditions $< \xi^2 h' >= 0$, and $< \xi^3 T' >= 2a < \xi T' >$

$$0 = -2r < \xi^2 T' > +\sigma 2Ba < \xi T' > \tag{A.15}$$

which yields

$$< \xi^2 T' >= \frac{\sigma}{r} Ba < \xi T' > \tag{A.16}$$

From Levine and Jin (2010)

$$\frac{d<\xi T'>}{dt} = -(\lambda + r) < \xi T' > +\omega < \xi h' > +\sigma(1 + B < T >) + \sigma B < \xi^2 T' > \tag{A.17}$$

Again assuming steady state, $r >> \lambda$ and that closure conditions $< \xi h' >= 0$, and $< \xi^2 T' >= 0$

$$0 = -r < \xi T' > +\sigma \tag{A.18}$$

which yields

$$< \xi T' >= \frac{\sigma}{r} \tag{A.19}$$

Plugging equation (19) into equation (16)

$$< \xi^2 T' >= \frac{\sigma^2}{r^2} Ba \tag{A.20}$$

Plugging into equation (13)

$$< \xi T'^2 >= \frac{2\sigma}{r} Ba(\frac{\sigma^2}{r^2} - 2 < T'^2 >) \tag{A.21}$$

Assuming the fourth order closure condition $< \xi T'^3 >= 2a < \xi T' >< T'^2 >$ and plugging into equation (10)

$$< T'^3 >= \frac{\frac{-4Ba\sigma^2}{r} < T'^2 > + \frac{2Ba\sigma^3}{r^3}}{\lambda^2 + \frac{1}{2}\omega^2} \tag{A.22}$$

Since $r^3 >> r$,

$$\frac{< T'^3 >}{< T'^2 >} = \frac{\frac{2Ba\sigma^2}{r}}{\lambda^2 + \frac{1}{2}\omega^2} \tag{A.23}$$

Skewness is defined as $\frac{T'^3}{(T'^2)^{\frac{3}{2}}}$, so we must also solve for T'^2. Assuming steady state in equation (1) and $< h'T' >= 0$ yields

$$0 = -2\lambda < T'^2 > +2\sigma < \xi T' > +2\sigma B < \xi T'^2 > \tag{A.24}$$

Substituting in equations (21) and (19) and solving for $< T'^2 >$ yields

$$< T'^2 >= \frac{\frac{\sigma^2}{r}(1 + 2B^2 a \frac{\sigma^2}{r})}{\lambda + 4B^2 a \frac{\sigma^2}{r}} \tag{A.25}$$

Taking the square root of equation (25) and $r^2 >> r$

$$\sqrt{< T'^2 >} = \sqrt{\frac{\frac{\sigma^2}{r}}{\lambda + 4B^2 a \frac{\sigma^2}{r}}} \tag{A.26}$$

Since $\frac{<T'^3>}{<T'^2>}\frac{1}{\sqrt{<T'^2>}} = \frac{<T'^3>}{(<T'^2>)^{\frac{3}{2}}}$ divide equation (23) by equation (26).

$$S = \frac{< T'^3 >}{(< T'^2 >)^{\frac{3}{2}}} = \frac{2Ba\sqrt{\frac{\sigma^2}{r}}}{\lambda^2 + \frac{1}{2}\omega^2} * \sqrt{\lambda + 4B^2 a\frac{\sigma^2}{r}} \tag{A.27}$$

And thus the skewness is linearly dependent on B.

Bibliography

An, S.-I., 2008: Interannual Variations of the Tropical Ocean Instability Wave and ENSO. *Journal of Climate*, **21 (15)**, 3680–3686.

An, S.-I. and F.-F. Jin, 2004: Nonlinearity and asymmetry of ENSO. *Journal of Climate*, **17 (12)**, 2399–2412.

Ashok, K., S. K. Behera, S. A. Rao, H. Weng, and T. Yamagata, 2007: El Niño Modoki and its possible teleconnection. *Journal of Geophysical Research: Oceans (1978–2012)*, **112**, C11 007, doi:10.1029/2006JC003798.

Balmaseda, M. A., A. Vidard, and D. L. Anderson, 2008: The ECMWF ocean analysis system: ORA-S3. *Monthly Weather Review*, **136 (8)**, 3018–3034.

Battisiti, D. S. and A. C. Hirst, 1989: Interannual variability in the tropical atmosphere/ocean system: Influence of the basic state and ocean geometry. *Journal of the Atmospheric Sciences*, **46**, 1697–1712.

Bejarano, L. and F. F. Jin, 2008: Coexistence of Equatorial Coupled Modes of ENSO. *Journal of Climate*, **21**, 3501–3067.

Bellenger, H., E. Guilyardi, J. Leloup, M. Lengaigne, and J. Vialard, 2014: ENSO representation in climate models: from CMIP3 to CMIP5. *Climate Dynamics*, **42 (7-8)**, 1999–2018.

Boucharel, J., A. Timmermann, and F.-F. Jin, 2013: Zonal phase propagation of ENSO

sea surface temperature anomalies: Revisited. *Geophysical Research Letters*, **40 (15)**, 4048–4053.

Burgers, G., F.-F. Jin, and G. J. Van Oldenborgh, 2005: The simplest ENSO recharge oscillator. *Geophysical Research Letters*, **32 (13)**, L13 706, doi:10.1029/2005GL023110.

Cai, W., et al., 2014: Increasing frequency of extreme El Niño events due to greenhouse warming. *Nature Climate Change*, **4**, 111–116.

Choi, K., G. A. Vecchi, and A. Wittenberg, 2013: ENSO transition, duration, and amplitude Asymmetries: Role of the nonlinear wind stress coupling in a conceptual model. *Journal of Climate*, **26 (23)**, 9462–9476.

Cobb, K. M., N. Westphal, H. R. Sayani, J. T. Watson, E. Di Lorenzo, H. Cheng, R. L. Edwards, and C. D. Charles, 2013: Highly variable El Niño-Southern Oscillation throughout the Holocene. *Science*, **339**, 67–70.

Collins, M., et al., 2010: The impact of global warming on the tropical Pacific Ocean and El Niño. *Nature Geoscience*, **3 (6)**, 391–397.

Conroy, J. L., J. T. Overpeck, J. E. Cole, T. M. Shanahan, and M. Steinitz-Kannan, 2008: Holocene changes in eastern tropical Pacific climate inferred from a Galápagos lake sediment record. *Quaternary Science Reviews*, **27 (11)**, 1166–1180.

Delworth, T. L. and coauthors, 2006: GFDL's CM2 Global Coupled Climate Models. Part I: Formulation and Simulation Characteristics. *Journal of Climate*, **19**, 643–674.

Deser, C., et al., 2012: ENSO and Pacific Decadal Variability in the Community Climate System Model Version 4. *Journal of Climate*, **25 (8)**, 2622–2651.

DiNezio, P. N., B. P. Kirtman, A. C. Clement, S.-K. Lee, G. A. Vecchi, and A. Wittenberg, 2012: Mean Climate Controls on the Simulated Response of ENSO to Increasing Greenhouse Gases. *Journal of Climate*, **25 (21)**, 7399–7420.

Eisenman, I., L. Yu, and E. Tziperman, 2005: Westerly Wind Bursts: ENSO's tail rather than the dog? *Journal of Climate*, **18**, 5224–5238.

Fedorov, A. V., S. Hu, M. Lengaigne, and E. Guilyardi, 2014: The impact of westerly wind bursts and ocean initial state on the development, and diversity of El Niño events. *Climate Dynamics*, In press, doi:10.1007/s00382-014-2126-4.

Fedorov, A. V. and S. G. Philander, 2000: Is El Niño changing? *Science*, **288 (5473)**, 1997–2002.

Fedorov, A. V. and S. G. Philander, 2001: A stability analysis of tropical ocean–atmosphere interactions: Bridging measurements and theory for El Niño. *Journal of Climate*, **14 (14)**, 3086–3101.

Frankignoul, C. and K. Hasselmann, 1977: Stochastic climate models: Part II application to sea-surface temperature anomalies and thermocline variability. *Tellus*, **29 (4)**, 289–305.

Gebbie, G., I. Eisenman, A. Wittenberg, and E. Tziperman, 2007: Modulation of westerly wind bursts by sea surface temperature: a semistochastic feedback of ENSO. *Journal of the Atmospheric Sciences*, **64**, 3281–3295.

Gebbie, G. and E. Tziperman, 2009a: Incorporating a semi-stochastic model of ocean-modulated westerly wind bursts into an ENSO prediction model. *Theoretical and Applied Climatology*, **97 (1-2)**, 65–73.

Gebbie, G. and E. Tziperman, 2009b: Predictability of SST-modulated westerly wind bursts. *Journal of Climate*, **22**, 3894–3909.

Gent, P. R., et al., 2011: The Community Climate System Model Version 4. *Journal of Climate*, **24 (19)**, 4973–4991.

Graham, F. S., J. N. Brown, C. Langlais, S. J. Marsland, A. T. Wittenberg, and N. J. Holbrook, 2014: Effectiveness of the Bjerknes stability index in representing ocean dynamics. *Climate Dynamics*, In press, doi:10.1007/s00382-014-2062-3.

Ham, Y.-G. and J.-S. Kug, 2014: ENSO phase-locking to the boreal winter in CMIP3 and CMIP5 models. *Climate Dynamics*, **43 (1-2)**, 305–318.

Harrison, D. and A. Chiodi, 2009: Pre-and Post-1997/98 Westerly Wind Events and Equatorial Pacific Cold Tongue Warming. *Journal of Climate*, **22 (3)**, 568–581.

Hoerling, M. P., A. Kumar, and M. Zhong, 1997: El Niño, La Niña, and the nonlinearity of their teleconnections. *Journal of Climate*, **10 (8)**, 1769–1786.

Jin, F. F., 1997a: An equatorial ocean recharge paradigm for ENSO. Part I: Conceptual model. *Journal of the Atmospheric Sciences*, **54**, 811–829.

Jin, F.-F., 1997b: An equatorial ocean recharge paradigm for ENSO. Part II: A stripped-down coupled model. *Journal of the Atmospheric Sciences*, **54 (7)**, 830–847.

Jin, F.-F. and S.-I. An, 1999a: Thermocline and zonal advective feedbacks within the equatorial ocean recharge oscillator model for ENSO. *Geophysical Research Letters*, **26 (19)**, 2989–2992.

Jin, F.-F. and S.-I. An, 1999b: Thermocline and zonal advective feedbacks within the equatorial ocean recharge oscillator model for ENSO. *Geophysical Research Letters*, **26 (19)**, 2989–2992.

Jin, F.-F., S.-I. An, A. Timmermann, and J. Zhao, 2003: Strong El Niño events and nonlinear dynamical heating. *Geophysical Research Letters*, **30 (3)**, 20–1.

Jin, F. F., L. Lin, A. Timmermann, and J. Zhao, 2007: Ensemble-mean dynamics of the ENSO recharge oscillator under state dependent stochastic forcing. *Geophysical Research Letters*, **34**, L03 807, doi:doi:10.1029/2006GL027372.

Jin, F.-F. and D. Neelin, 1993a: Modes of interannual tropical ocean-atmosphere interaction-A unified view. Part III: Analytical results in fully coupled cases. *Journal of the Atmospheric Sciences*, **50 (21)**, 3523–3540.

Jin, F.-F. and J. D. Neelin, 1993b: Modes of interannual tropical ocean-atmosphere interaction-a unified view. Part I: Numerical results. *Journal of the Atmospheric Sciences*, **50 (21)**, 3477–3503.

Jin, F.-F., J. D. Neelin, and M. Ghil, 1994: El Niño on the devil's staircase: Annual subharmonic steps to chaos. *Science*, **264 (5155)**, 70–72.

Jin, F. F., L. L. Pan, and M. Watanabe, 2006: Dynamics of synoptic eddy and low-frequency flow feedback. Part I: A dynamic closure. *Journal of the Atmospheric Sciences*, **64**, 1677–1694.

Johnson, N. C., 2013: How Many ENSO Flavors Can We Distinguish? *Journal of Climate*, **26 (13)**, 4816–4827.

Kang, I.-S. and J.-S. Kug, 2002: El Niño and La Niña sea surface temperature anomalies: Asymmetry characteristics associated with their wind stress anomalies. *Journal of Geophysical Research: Atmospheres (1984–2012)*, **107 (D19)**, ACL–1.

Kapur, A. and C. Zhang, 2012: Multiplicative MJO forcing of ENSO. *Journal of Climate*, **25 (23)**, 8132–8147.

Keen, R., 1982: The role of cross-equatorial cyclone pairs in the Southern Oscillation. *Monthly Weather Review*, **119**, 1405–1416.

Kessler, W. S., 2002: Is ENSO a cycle or a series of events? *Geophysical Research Letters*, **29 (23)**, 40–1.

Kessler, W. S. and R. Kleeman, 2000: Rectification of the Madden-Julian Oscillation in to the ENSO cycle. *Journal of Climate*, **13**, 3560–3575.

Kim, S. T. and F.-F. Jin, 2011a: An ENSO stability analysis. Part I: results from a hybrid coupled model. *Climate Dynamics*, **36 (7-8)**, 1593–1607.

Kim, S. T. and F. F. Jin, 2011b: An ENSO stability analysis. Part II: Results from the twentieth and twenty-first century simulations of the CMIP3 models. *Climate Dynamics*, **36 (7-8)**, 1609–1627.

Kleeman, R. and A. M. Moore, 1997: A theory for the limitation of ENSO predictability due to stochastic atmospheric transients. *Journal of the Atmospheric Sciences*, **54**, 753–767.

Kug, J.-S., F.-F. Jin, and S.-I. An, 2009: Two types of El Niño events: Cold tongue El Niño and warm pool El Niño. *Journal of Climate*, **22 (6)**, 1499–1515.

Kug, J. S., F. F. Jin, K. P. Sooraj, and I. S. Kang, 2008: State-dependant atmospheric noise associated with ENSO. *Geophysical Research Letters*, **35**, L05 701, doi: 10.1029/2007GL032017.

Lengaigne, M., E. Guilyardi, J. P. Boulanger, C. Menkes, P. Delecluse, P. Inness, J. Cole, and J. Slingo, 2004: Triggering El Niño by westerly wind events in a coupled general circulation model. *Climate Dynamics*, **23**, 601–620.

Levine, A. F. Z. and F. F. Jin, 2010: Noise-induced instability in the ENSO recharge oscillator. *Journal of the Atmosmospheric Sciences*, **67**, 529–542.

Lopez, H. and B. P. Kirtman, 2013: Westerly wind bursts and the diversity of ENSO in CCSM3 and CCSM4. *Geophysical Research Letters*, **40 (17)**, 4722–4727.

Lopez, H., B. P. Kirtman, E. Tziperman, and G. Gebbie, 2013: Impact of interactive westerly wind bursts on CCSM3. *Dynamics of Atmospheres and Oceans*, **59**, 24–51.

Marzeion, B., A. Timmermann, R. Murtugudde, and F.-F. Jin, 2005: Biophysical feedbacks in the tropical Pacific. *Journal of Climate*, **18 (1)**, 58–70.

McGregor, S., A. Timmermann, N. Schneider, M. F. Stuecker, and M. H. England, 2012: The Effect of the South Pacific Convergence Zone on the Termination of El Niño Events and the Meridional Asymmetry of ENSO. *Journal of Climate*, **25 (16)**, 5566–5586.

McGregor, S., A. Timmermann, and O. Timm, 2010: A unified proxy for ENSO and PDO variability since 1650. *Climate of the Past*, **6 (1)**, 1–17.

McPhaden, M. J., 1999: Genesis and evolution of the 1997-98 El Niño. *Science*, **283**, 950–954.

McPhaden, M. J., H. P. Freitag, S. P. Hayes, B. A. Taft, Z. Chen, and K. Wyrtki, 1988: The response of the equatorial Pacific Ocean to a westerly wind burst in May 1986. *Journal of Geophysical Research: Oceans (1978–2012)*, **93 (C9)**, 10 589–10 603.

McPhaden, M. J. and X. Yu, 1999: Equatorial Waves and the 1997-98 El Niño. *Geophysical Research Letters*, **26**, 2961–2964.

Meinen, C. S. and M. J. McPhaden, 2000: Observations of warm water volume changes in the equatorial Pacific and their relationship to El Niño and La Niña. *Journal of Climate*, **13 (20)**, 3551–3559.

Merkel, U., M. Prange, and M. Schulz, 2010: ENSO variability and teleconnections during glacial climates. *Quaternary Science Reviews*, **29 (1)**, 86–100.

Moore, A. M. and R. Kleeman, 1999: Stochastic forcing of ENSO by the intraseasonal oscillation. *Journal of Climate*, **12**, 1199–1220.

Moore, A. M. and R. Kleeman, 2001: The differences between the optimal perturbation of coupled models of ENSO. *Journal of Climate*, **14**, 138–163.

Müller, D., 1987: Bispectra of sea-surface temperature anomalies. *Journal of Physical Oceanography*, **17 (1)**, 26–36.

Neelin, J. D. and F.-F. Jin, 1993: Modes of interannual tropical ocean-atmosphere interaction-a unified view. Part II: Analytical results in the weak-coupling limit. *Journal of the Atmospheric Sciences*, **50 (21)**, 3504–3522.

Nicholls, N., 2001: Atmospheric and climatic hazards: Improved monitoring and prediction for disaster mitigation. *Natural Hazards.*, **23**, 137–155.

Ogata, T., S.-P. Xie, A. Wittenberg, and D.-Z. Sun, 2013: Interdecadal amplitude modulation of El Niño-Southern Oscillation and its impact on tropical Pacific decadal variability. *Journal of Climate*, **26 (18)**, 7280–7297.

Okumura, Y. M. and C. Deser, 2010: Asymmetry in the duration of El Niño and La Niña. *Journal of Climate*, **23 (21)**, 5826–5843.

Okumura, Y. M., M. Ohba, C. Deser, and H. Ueda, 2011: A proposed mechanism for the asymmetric duration of El Niño and La Niña. *Journal of Climate*, **24 (15)**, 3822–3829.

Penland, C., 1996: A stochastic model of IndoPacific sea surface temperature anomalies. *Physica D*, **98**, 534–558.

Penland, C. and P. D. Sardeshmukh, 1995: The optimal growth of tropical sea surface temperature anomalies. *Journal of Climate*, **8**, 1999–2024.

Perez, C. L., A. M. Moore, J. Zavala-Garay, and R. Kleeman, 2005: A comparison of the influence of additive and multiplicative stochastic forcing on a coupled model of ENSO. *Journal of Climate*, **18**, 5066–5085.

Power, S., F. Delage, C. Chung, G. Kociuba, and K. Keay, 2013: Robust twenty-first century projections of El Niño and related precipitation variability. *Nature*, **502**, 541–545.

Rasmussen, E. M. and T. H. Carpenter, 1982: Variations in tropical sea surface temperature and surface wind fields associated with the Southern Oscillation/El Niño. *Monthly Weather Review*, **110 (5)**, 354–384.

Ray, S. and B. S. Giese, 2012: Historical changes in El Niño and La Niña characteristics in an ocean reanalysis. *Journal of Geophysical Research: Oceans (1978–2012)*, **117 (C11007)**, doi:10.1029/2012JC008031.

Rayner, N. A., D. E. Parker, E. B. Horton, C. K. Folland, L. Alexandre, D. P. Rowell, E. C. Kent, and A. Kaplan, 2003: Global analyses of sea surface temperature, sea ice an night marine air temperature since the late nineteenth century. *Journal of Geophysical Research*, **108 (D14)**, 4407.

Ren, H.-L. and F.-F. Jin, 2011: Niño indices for two types of ENSO. *Geophysical Research Letters*, **38 (4)**, L04 704, doi:10.1029/2010GL046031.

Ren, H.-L. and F.-F. Jin, 2013: Recharge oscillator mechanisms in two types of ENSO. *Journal of Climate*, **26 (17)**, 6506–6523.

Roulston, M. S. and J. D. Neelin, 2000: The response of an ENSO model to climate noise, weather noise and intraseasonal forcing. *Geophysical Research Letters*, **27 (22)**, 3723–3726.

Santoso, A., S. McGregor, F.-F. Jin, W. Cai, M. H. England, S.-I. An, M. J. McPhaden, and E. Guilyardi, 2013: Late-twentieth-century emergence of the El Niño propagation asymmetry and future projections. *Nature*, **504 (7478)**, 126–130.

Sarachick, E. and M. Cane, 2010: *The El Niño-Southern Oscillation Phenomenon*. Cambridge University Press, 369 pp.

Sardeshmukh, P. D. and P. Sura, 2009: Reconciling non-gaussian climate statistics with linear dynamics. *Journal of Climate*, **22**, 1193–1207.

Stein, K., 2008: The Effect of the Seasonal Cycle on ENSO in a Stochastic Recharge Oscillator Model. M.S. thesis, Department of Oceanography, University of Hawaii at Manoa.

Stein, K., N. Schneider, A. Timmermann, and F.-F. Jin, 2010: Seasonal synchronization of ENSO events in a linear stochastic model. *Journal of Climate*, **23 (21)**, 5629–5643.

Stein, K., A. Timmermann, and N. Schneider, 2011: Phase synchronization of the El Niño-Southern oscillation with the annual cycle. *Physical Review Letters*, **107**, 128 501, doi:10.1103/PhysRevLett.107.128501, URL `http://link.aps.org/doi/10.1103/PhysRevLett.107.128501`.

Stein, K., A. Timmermann, N. Schneider, F.-F. Jin, and M. F. Stuecker, 2014: ENSO seasonal synchronization theory. *Journal of Climate*, **27 (2014)**, 5285–5310.

Stevenson, S., B. Fox-Kemper, M. Jochum, R. Neale, C. Deser, and G. Meehl, 2012: Will there be a significant change to El Niño in the twenty-first century? *Journal of Climate*, **25 (6)**, 2129–2145.

Stuecker, M. F., A. Timmermann, F. F. Jin, S. McGregor, and H. Ren, 2013: A combination mode of the annual cycle and the El Niño/Southern Oscillation. *Nature Geosience*, **6**, 540–544.

Suarez, M. J. and P. S. Schopf, 1988: A delayed action oscillator for ENSO. *Journal of the Atmospheric Sciences*, **45**, 3283–3287.

Takahashi, K., A. Montecinos, K. Goubanova, and B. Dewitte, 2011: ENSO regimes: Reinterpreting the canonical and Modoki El Niño. *Geophysical Research Letters*, **38 (10)**, L10 704, doi:10.1029/2011GL047364.

The GFDL Global Atmospheric Model Development Team, 2004: The new GFDL global atmosphere and land model AM2–LM2: Evaluation with prescribed SST simulations. *Journal of Climate*, **17**, 4641–4673.

Timmermann, A. and F.-F. Jin, 2002: Phytoplankton influences on tropical climate. *Geophysical Research Letters*, **29 (23)**, 19–1.

Tziperman, E., M. A. Cane, and S. E. Zebiak, 1995: Irregularity and locking to the seasonal cycle in an ENSO prediction model as explained by the quasi-periodicity route to chaos. *Journal of the Atmospheric Sciences*, **52 (3)**, 293–306.

Tziperman, E. and L. Yu, 2007: Quantifying the dependence of westerly wind bursts on the large-scale tropical Pacific SST. *Journal of Climate*, **20**, 2760–2768.

Uppala, S. M., et al., 2005: The ERA-40 reanalysis. *Quarterly Journal of the Royal Meteorological Society*, **131**, 2961–3012.

Vecchi, G., A. Wittenberg, and A. Rosati, 2006: Reassessing the role of stochastic forcing in the 1997–1998 El Niño. *Geophysical Research Letters*, **33 (1)**, L01 706, doi:10.1029/2005GL024738.

Vecchi, G. A. and D. E. Harrison, 2000: Tropical Pacific sea surface temperature anomalies, El Niño and equatorial westerly events. *Journal of Climate*, **13**, 1814–1830.

Vialard, J., C. Menkes, J. P. Boulanger, P. Delecluse, E. Guilyardi, M. J. McPhaden, and G. Madec, 2001: A model study of oceanic mechanisms affecting equatorial Pacific sea surface temperature during the 1997-98 El Nino. *Journal of Physical Oceanography*, **31**, 1649–1675.

Wang, W. and M. J. McPhaden, 2000: The surface-layer heat balance in the equatorial Pacific Ocean. Part II: Interannual variability. *Journal of Physical Oceanography*, **30 (11)**, 2989–3008.

Watanabe, M., M. Chikira, Y. Imada, and M. Kimoto, 2011: Convective control of ENSO simulated in MIROC. *Journal of Climate*, **24 (2)**, 543–562.

Webster, P. J. and R. Lukas, 1992: TOGA COARE: The coupled ocean-atmosphere response experiment. *Bulletin of the American Meteorological Society*, **73 (9)**, 1377–1416.

Wittenberg, A. T., 2009: Are historical records sufficient to contrain ENSO simulations. *Geophysical Research Letters*, **36 (12)**, L12 702, doi:10.1029/2009GL038710.

Xie, S.-P., C. Deser, G. A. Vecchi, J. Ma, H. Teng, and A. T. Wittenberg, 2010: Global warming pattern formation: Sea surface temperature and rainfall. *Journal of Climate*, **23 (4)**, 966–986.

Yeh, S.-W., J.-S. Kug, B. Dewitte, M.-H. Kwon, B. P. Kirtman, and F.-F. Jin, 2009: El Niño in a changing climate. *Nature*, **461 (7263)**, 511–514.

Yu, L., R. A. Weller, and T. W. Liu, 2003: Case analysis of a role of ENSO in regulating the generation of westerly wind bursts in the western equatorial Pacific. *Journal of Geophysical Research*, **108 (C4)**, 3128, doi:10.1029/2002JC001498.

Yu, X. and M. J. McPhaden, 1999: Dynamical Analysis of Seasonal and Interannual Variability in the Equatorial Pacific. *Journal of Physical Oceanography*, **29 (9)**, 2350–2369.

Zavala-Garay, J., A. M. Moore, and R. Kleeman, 2004: Influence of stochastic forcing on ENSO prediction. *Journal of Geophysical Research*, **109**, C1107, doi: 10.1029/2004JC002406.

Zavala-Garay, J., A. M. Moore, C. L. Perez, and R. Kleeman, 2003: The response of a coupled model of ENSO to observed estimates of stochastic forcing. *Journal of Climate*, **16**, 2827–2842.

Zavala-Garay, J., C. Zhang, A. M. Moore, and R. Kleeman, 2005: The linear response of ENSO to the Madden-Julian Oscillation. *Journal of Climate*, **18**, 2441–2459.

Zavala-Garay, J., C. Zhang, A. M. Moore, A. Wittenberg, M. J. Harrison, A. Rosati, J. Vialard, and R. Kleeman, 2008: Sensitivity of hybrid ENSO models to unresolved atmospheric variability. *Journal of Climate*, **21**, 3704–3721.